2018

MULTIMODAL NONCONTACT DIFFUSE OPTICAL REFLECTANCE IMAGING OF BLOOD FLOW AND FLUORESCENCE CONTRASTS

Daniel Irwin
University of Kentucky, daniel.irwin@uky.edu
Digital Object Identifier: https://doi.org/10.13023/ETD.2018.125

STUDENT AGREEMENT:

I represent that my thesis or dissertation and abstract are my original work. Proper attribution has been given to all outside sources. I understand that I am solely responsible for obtaining any needed copyright permissions. I have obtained needed written permission statement(s) from the owner(s) of each third-party copyrighted matter to be included in my work, allowing electronic distribution (if such use is not permitted by the fair use doctrine) which will be submitted to UKnowledge as Additional File.

I hereby grant to The University of Kentucky and its agents the irrevocable, non-exclusive, and royalty-free license to archive and make accessible my work in whole or in part in all forms of media, now or hereafter known. I agree that the document mentioned above may be made available immediately for worldwide access unless an embargo applies.

I retain all other ownership rights to the copyright of my work. I also retain the right to use in future works (such as articles or books) all or part of my work. I understand that I am free to register the copyright to my work.

REVIEW, APPROVAL AND ACCEPTANCE

The document mentioned above has been reviewed and accepted by the student's advisor, on behalf of the advisory committee, and by the Director of Graduate Studies (DGS), on behalf of the program; we verify that this is the final, approved version of the student's thesis including all changes required by the advisory committee. The undersigned agree to abide by the statements above.

Daniel Irwin, Student

Dr. Guoqiang Yu, Major Professor

Dr. Abhijit R. Patwardhan, Director of Graduate Studies

MULTIMODAL NONCONTACT DIFFUSE OPTICAL REFLECTANCE IMAGING OF BLOOD FLOW AND FLUORESCENCE CONTRASTS

DISSERTATION

A dissertation submitted in partial fulfillment of the
requirements for the degree of Doctor of Philosophy in the
College of Engineering
at the University of Kentucky

By
Daniel Irwin

Lexington, Kentucky

Director: Dr. Guoqiang Yu, Professor of Biomedical Engineering

Lexington, Kentucky

2018

ABSTRACT OF DISSERTATION

MULTIMODAL NONCONTACT DIFFUSE OPTICAL REFLECTANCE IMAGING OF BLOOD FLOW AND FLUORESCENCE CONTRASTS

In this study we design a succession of three increasingly adept diffuse optical devices towards the simultaneous 3D imaging of blood flow and fluorescence contrasts in relatively deep tissues. These metrics together can provide future insights into the relationship between blood flow distributions and fluorescent or fluorescently tagged agents. A noncontact diffuse correlation tomography (ncDCT) device was firstly developed to recover flow by mechanically scanning a lens-based apparatus across the sample. The novel flow reconstruction technique and measuring boundary curvature were advanced in tandem. The establishment of CCD camera detection with a high sampling density and flow recovery by speckle contrast followed with the next instrument, termed speckle contrast diffuse correlation tomography (scDCT). In scDCT, an optical switch sequenced coherent near-infrared light into contact-based source fibers around the sample surface. A fully noncontact reflectance mode device finalized improvements by combining noncontact scDCT (nc_scDCT) and diffuse fluorescence tomography (DFT) techniques. In the combined device, a galvo-mirror directed polarized light to the sample surface. Filters and a cross polarizer in stackable tubes promoted extracting flow indices, absorption coefficients, and fluorescence concentrations (indocyanine green, ICG). The scDCT instrumentation was validated through detection of a cubical solid tissue-like phantom heterogeneity beneath a liquid phantom (background) surface where recovery of its center and dimensions agreed with the known values. The combined nc_scDCT/DFT identified both a cubical solid phantom and a tube of stepwise varying ICG concentration (absorption and fluorescence contrast). The tube imaged by nc_scDCT/DFT exhibited expected trends in absorption and fluorescence. The tube shape, orientation, and localization were recovered in general agreement with actuality. The flow heterogeneity localization was successfully extracted and its average relative flow values in agreement with previous studies. Increasing ICG concentrations induced notable disturbances in the tube region (≥ 0.25 μM/1 μM for 785 nm/830 nm) suggesting the graduating absorption (320% increase at 785 nm) introduced errors. We observe that 830 nm is lower in the ICG absorption

spectrum and the correspondingly measured flow encountered less influence than 785 nm. From these results we anticipate the best practice in future studies to be utilization of a laser source with wavelength in a low region of the ICG absorption spectrum (e.g., 830 nm) or to only monitor flow prior to ICG injection or post-clearance. In addition, ncDCT was initially tested in a mouse tumor model to examine tumor size and averaged flow changes over a four-day interval. The next steps in forwarding the combined device development include the straightforward automation of data acquisition and filter rotation and applying it to *in vivo* tumor studies. These animal/clinical models may seek information such as simultaneous detection of tumor flow, fluorescence, and absorption contrasts or analyzing the relationship between variably sized fluorescently tagged nanoparticles and their tumor deposition relationship to flow distributions.

KEYWORDS: Speckle Contrast Diffuse Correlation Tomography (scDCT), Noncontact Diffuse Correlation Tomography (ncDCT), Blood Flow, Fluorescence, Multimodal Imaging

Daniel Irwin

April 19th, 2018
Date

MULTIMODAL NONCONTACT DIFFUSE OPTICAL REFLECTANCE IMAGING OF BLOOD FLOW AND FLUORESCENCE CONTRASTS

By

Daniel Irwin

Dr. Guoqiang Yu
Director of Dissertation

Dr. Abhijit R. Patwardhan
Director of Graduate Studies

April 19th, 2018

DEDICATION

This work is dedicated to my family.

ACKNOWLEDGMENTS

The assistance and support afforded me spans many individuals of varying backgrounds and expertise to which I am especially appreciative.

As having been my advisor throughout both my Master's and Doctorate program, Dr. Guoqiang Yu deserves many thanks. His exceptional work ethic and dedication have impressed positively upon my available opportunities, collaborations, and research potential. He has continuously served as an inexhaustible resource of profound observations, keen insights, and tracking down the effectively simple alternatives when difficulties in methodology arise.

Current and former lab members contributed significantly to my success. I would like to thank Dr. Chong Huang for allowing me to glean some of his understanding in optical device development and experimental design. His leading by example was a persistent inspiration of confidence. Dr. Yu Shang was a well of knowledge and clarity with an accompaniment of approachability and magnanimity. Dr. Lixin Dong fielded a large assortment of random questions on science and research topics both humbly and with intellect between intervals of clinical measurements. Working with Dr. Ran Cheng enabled me to gain a deeper understanding into the potential breadth of Biomedical Engineering with his ability to combine skills from multiple areas. Dr. Lian He's efforts helped me to bridge gaps of competency among the different steps involved in imaging. Dr. Yu Lin was a benefactor in all respects to camera details and reconstructions. Ahmed Bahrani in his research and discussions fostered an enhanced comprehension into hardware internals. Mingjun Zhao produced thought provoking questions forcing

me to improve my own interpretations and was always cordial when I needed to borrow instruments from her studies. Siavash Mazdeyasna was frequently attentive and quick to offer useful supplementary information regarding experimental concerns. I would also like to thank other lab members of whom I was only able to work with briefly, namely Weikai Kong, Katelyn Gurley, Brad Henry, and Drs. Youquan Zhao, Myeongsu Seong, Daniel Kameny, and Ting Li.

I would like to additionally extend thanks to the remaining members of my PhD committee and Cancer Nanotechnology Training Center Predoctoral Traineeship mentors. These include Drs. David Puleo, Abhijit Patwardhan, Jia Luo, Bradley Anderson, and Mahesh Kudrimoti. These individuals offered me valuable feedback, collaborative investigations, and sustained an impetus on my progress. I also thank several others who have assisted me over the years including Drs. Hainsworth Shin, Thomas Dziubla, Xiaoyan Zhang, Kyle Fugit, Mei Xu, and Haiping Wang, and Rebecca Hisel, Sue Mills, Joyce Evans, Jennifer Hart, and Tonya Vance.

I acknowledge funding from the National Institutes of Health (NIH) R01-CA149274 Grant, R21-AR062356 Grant, UL-1RR033173 Pilot Grant, R25-CA153954 Predoctoral Traineeship, and National Endowment for Plastic Surgery (NEPS) from the Plastic Surgery Foundation. The content herein is solely the responsibility of the author(s) and does not necessarily represent the official views of the NIH or NEPS.

TABLE OF CONTENTS

LIST OF TABLES

LIST OF FIGURES

CHAPTER 1 INTRODUCTION

1.1 Blood Flow and Fluorescence in Cancer Research

Blood flow and its response to physiological changes can serve as a status indicator into underlying tissue microenvironment conditions. Many diseased and abnormal progressions manifest through functional presentation as well as, or even prior to, observable structural alterations. Thus, monitoring the blood flow can provide supporting information to medical professionals in the detection, diagnosis, and treatment of patients. It may also serve in early studies on small animals which seek to gain, for example, insights into disease mechanisms and the effectiveness of treatments. One of the most prevalent objectives in flow studies is then to observe the contrast in flow between healthy and abnormal tissues which can help characterize diseases such as cancer.

Specifically, the microenvironment of cancerous tissues is distinguishable from healthy tissues by its highly irregular and chaotic vascular network. The feature of induced angiogenesis has been identified as one of the hallmarks of cancer [1]. How this overarching observation originates and presents in specific cases varies widely. A summarization of reported intertumoral blood flows in human malignancies and healthy tissues highlights upon the disparities; for example, squamous cell carcinoma breast cancer blood flow was found to range from ~0.07 – 0.40 ml/g/min compared to the mean healthy lactating and post-menopausal breast of 0.80 and 0.04 ml/g/min respectively [2]. The linking of increased angiogenesis and blood flow has been reported [3, 4]. Furthermore, tumor

vascularity as evaluated by mean arteriole number has been shown to exhibit a 3-fold increase in carcinomas [4]. Intratumoral variations frequently occur due to the unregulated growth and cellular proliferation accompanied by other microenvironmental alterations. Hypoxic and necrotic tissue regions can form in unpredictable fashion as nutrient transport is inhibited by perfunctory vessel networks and the collapse of vessels due to rising interstitial pressures [2].

Fluorescing agents also play a role of great medical interest, especially in cancer studies. One of the biggest impediments to cancer treatment is the ability to penetrate and effectively deliver drugs or other factors throughout a solid tumor. Adequate drug delivery and targeting of tumor tissues then largely governs treatment success [5-10]. Some studies rely on the enhanced permeability and retention (EPR) effect [11]. The injection of drugs is expected under EPR circumstances to preferentially accumulate in the leaky tumor vasculature. This behavior is extended to the injection of fluorescent agents for localizing in and demarcating tumor tissues. Though useful, the EPR assumption is not ideal and much current research into increasing control has taken the direction of nanotechnology, including the labeling of nanoparticles with fluorescence [12]. Nanoparticles provide a robust framework for leveraging receptor targeting, polymorphic adaptations, and drug loading and are expected to become an essential part of cancer therapy. It is anticipated that multipurpose nanoparticle designs can tailor treatments in innovative ways to the unique features of different cancers, location, and subject.

1.2 Medical Imaging and Diffuse Optics

Contemporary medical imaging options are numerous as is evinced by perusing any modern healthcare facilities' list of imaging services. These may be practically differentiated by the nature of their probe such as acoustic waves (Ultrasound, Doppler Ultrasound) and electromagnetic radiation as x-rays (Projection Radiography, Mammography, Computed Tomography, Fluoroscopy), visible light (Optical Coherence Tomography, Laser Speckle Contrast Imaging, Laser Doppler), radiofrequency (Magnetic Resonance Imaging, Functional Magnetic Resonance Imaging/Blood-Oxygen-Level Dependent Contrast Imaging, Magnetic Resonance Angiography), and injectable emitters of gamma rays (nuclear imaging; Positron Emission Tomography, Stimulated Positron Emission Computed Tomography). The latitudes in making an appropriate selection depend on many factors including the type of information recoverable, tissue type applicability (i.e., brain, muscle), safety, hardware and operating costs, and time and convenience (i.e., image acquisition duration, real-time vs. delayed results). Near-infrared (NIR; 650-900 nm) light has gained growing contemporary popularity among medical imaging modalities with its clinically preferential safety (e.g., nonionizing radiation), noninvasiveness, sensitivity to physiological processes in deep tissues (several centimeters), relative low cost in the realm of clinical imaging instrumentation, and potential for portable bedside measurements.

Advances over the last two centuries have set the foundation for modern NIR optics and tomography including the development of appropriate theories and observations (i.e., statistical physics, wave-particle duality, radiative transfer), and

available tools/technology (i.e., fast and efficient algorithms, modeling software, computing resources, lasers, sensitive light detectors). Less than two decades after the advent of the laser around 1960, an “NIR Window” (**Figure 1.1**) was distinguished (though recognition of optical transmission in tissue existed prior [13]) whereby biological tissues present low optical absorption and high scattering allowing measurement of oxygenated hemoglobin and deoxygenated hemoglobin concentrations (tissue oxygenation) [14]. The current diffuse optical instrumentation stemming from this collective keystone are diverse. Systems may be separated by use of continuous-wave (CW; intensity), frequency-domain (FD; amplitude and phase), or time-domain (TD; temporal point spread function) paradigms which inherently envelopes their measurables and dictates system design. Prioritizing transillumination or reflectance signals further dichotomizes their suitable applications. The systems may focus on spectroscopy or imaging, the latter typically the most desirable and consequently complex.

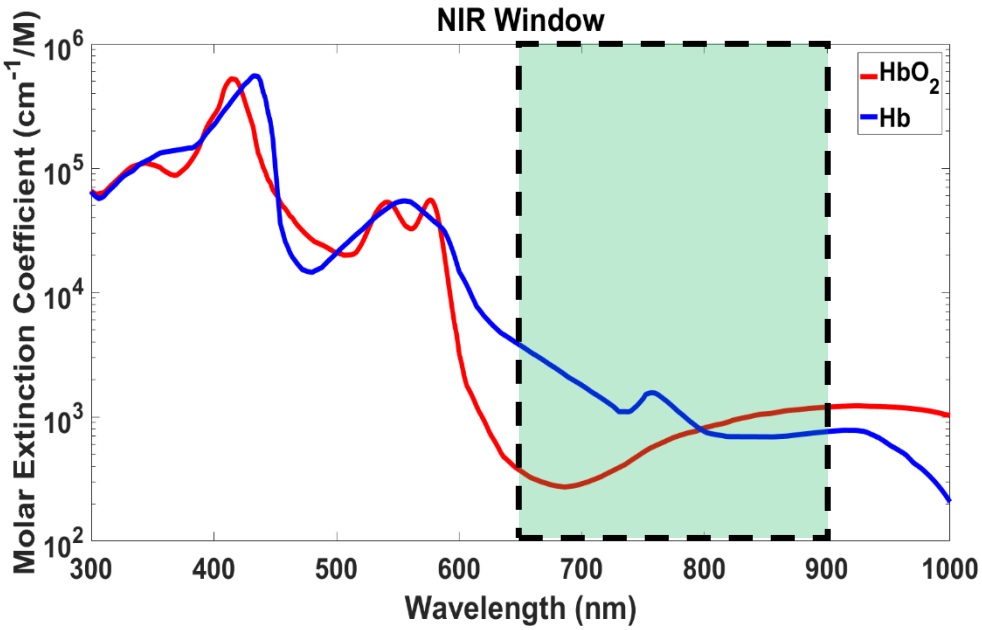

Figure 1.1: The near-infrared window. The molar extinction coefficient demonstrates low light absorption characteristics of the common intrinsic absorbing tissue chromophores: oxygenated hemoglobin, HbO_2, and deoxygenated hemoglobin, Hb.

The properties of light in the NIR spectrum and its interactions with biological tissues offer many options for extracting useful information depending on the particular feature of light and type of tissue such as angiogenesis, biochemical information, metabolism, and scatterer size distributions [14, 15]. In this study, we restrict ourselves to CW systems which are the simplest and most economical paradigm. We incorporate three diffuse optical imaging modalities capable of extracting unique sets of information, namely diffuse optical spectroscopy and tomography (DOS/DOT) for absorption, diffuse fluorescence spectroscopy and tomography (DFS/DFT; also known as diffuse optical fluorescence tomography

DOFT) for fluorophore concentration, and diffuse correlation spectroscopy and tomography (DCS/DCT) for blood flow changes.

These diffuse optical techniques have proven successful in cancer research investigations. For example, absorption contrasts, enhanced by indocyanine green (ICG) and measured by DOT, identified cancerous tissues (e.g., ductal carcinoma, fibroadenoma) and a non-specific heterogeneous distribution for healthy tissues (e.g., no disease) in the human breast [16]. These results were validated against Gadolinium (Gd)-enhanced MRI images. The fluorescent signal contrasts of ICG have also been measured by DFT in separating healthy and diseased human breast tissues (e.g., invasive carcinomas), validated against Gd-enhanced MRI [17]. Sufficient temporal resolution enables using absorption and/or concentration information to examine the ICG pharmacokinetics [18]. The simultaneous monitoring of absorption and fluorescence changes has already been methodically compared to determine the optimal acquisition arrangement (under FD considerations) [19]. A DCT-based device, validated by ultrasound (US), exhibited that it too has the potential to differentiate healthy and abnormal breast tissues (e.g., ductal papilloma and low-grade adenocarcinoma, atypical ductal hyperplasia and low-grade carcinoma) through presentations of blood flow heterogeneities [20]. The combination of tissue hemodynamic parameters as recovered by diffuse optical methods was furthermore deemed beneficial in predicting radiation therapy outcome in a recent head-neck tumor study [21].

1.3 Diffuse Optical Spectroscopy and Tomography (DOS/DOT)

The DOS/DOT technique often relies on the photon diffusion equation (PDE) which we make use of to extract tissue absorption information and derive a flow reconstruction method. The photon diffusion equation is defined with a continuous wave ($\omega = 0$) source for the photon fluence rate $\Phi(\boldsymbol{r})$ (W/cm^2) as [15]:

$$[\nabla \cdot D(\boldsymbol{r})\nabla - v\mu_a(\boldsymbol{r})]\Phi(\boldsymbol{r}) = -vS(\boldsymbol{r}) \tag{1.1}$$

with position vector $\boldsymbol{r}$ (cm), tissue absorption coefficient $\mu_a(\boldsymbol{r})$ (cm^{-1}), speed of light in the medium v (cm/s), photon diffusion coefficient $D \approx v/3\mu_s'(\boldsymbol{r})$ where $\mu_s'(\boldsymbol{r})$ (cm^{-1}) is the reduced scattering coefficient, and isotropic source term $S(\boldsymbol{r})$ (W/cm^3). Unless required for clarity the spatial dependence of the optical properties (μ_a, μ_s') will not be explicitly noted at every reference. The optical properties also exhibit a wavelength (λ) dependence which will be identified if context demands.

DOS/DOT techniques have been used in the monitoring and imaging of the reduced scattering coefficient, oxygenated and deoxygenated hemoglobin concentration, and oxygen saturation in addition to the absorption coefficient [22-27]. The absorption coefficient is related to chromophore concentrations as $\mu_a(\lambda) = \sum_{i=1}^{m} \epsilon_i(\lambda)[C_i]$ where ϵ_i and $[C_i]$ are the i^{th} chromophore's molar extinction and concentration, respectively. We do not evaluate chromophore contents in this study, but the primary biological absorber (wavelength dependent) in most tissues is hemoglobin with other minor contributors such as water varying in concentration with tissue type and composition. Using our CW system, we herein monitor

changes in the absorption coefficient $\mu_a(\boldsymbol{r})$ (cm^{-1}) only. The extension of the spectroscopic application to tomography follows the finite element method (FEM) implementation as described in **Chapter 4**.

1.4 Diffuse Fluorescence Spectroscopy and Tomography (DFS/DFT)

DFS/DFT establishes a set of coupled equations linking the diffusive propagation of the excitation light to the diffusive propagation of the emitted/fluoresced light. This is used to recover sample fluorescence changes and is commonly applied in cancer research [16, 17, 19, 28-37]. The fluorescence photon fluence $\Phi_{fl}(\boldsymbol{r})$ is described by (with CW) [17, 38]:

$$\left[\nabla \cdot D_{ex}(\boldsymbol{r})\nabla - v\mu_{a,ex}(\boldsymbol{r})\right]\Phi_{ex}(\boldsymbol{r}) = -vS(\boldsymbol{r}) \tag{1.2}$$

$$\left[\nabla \cdot D_{fl}(\boldsymbol{r})\nabla - v\mu_{a,fl}(\boldsymbol{r})\right]\Phi_{fl}(\boldsymbol{r}) = -(\eta\epsilon_{ex}[N])\Phi_{ex}(\boldsymbol{r}) \tag{1.3}$$

with excitation and emission parameters subscripted with *ex* and *fl* respectively, the fluorescence quantum yield η, fluorophore extinction coefficient ϵ_{ex}, and the fluorophore concentration $[N]$. The absorption coefficients here are contributed to by both endogenous chromophores and exogenous fluorophores. From **Equation 1.3** the RHS can be seen to be the solution to **Equation 1.2** modified by the fluorescence properties and concentration. The fluorescence yield, $\eta\epsilon_{ex}[N] = \eta\mu_{a,fl}$, is the parameter commonly resolved in practice and its relative change monitored. If η and ϵ_{ex} are known, then the absolute concentration can be separated. In this study, we monitor relative changes in the fluorescent yield as

produced by the addition of the exogenous ICG fluorescent agent. Tomography is implemented within the FEM framework in a manner similar to DOT and is also described in **Chapter 4**.

1.5 Diffuse Correlation Spectroscopy and Tomography (DCS/DCT)

DCS/DCT theory is provided by an analogous correlation diffusion equation (CDE) to the PDE which models the diffusive propagation of the unnormalized temporal electric field correlation function $G_1(\boldsymbol{r},\tau) = \langle E(\boldsymbol{r},t)E^*(\boldsymbol{r},t+\tau)\rangle$ in biological tissues. Fluctuations in this electric field enable detection of the underlying flow processes and DCS/DCT has been used in many applications including muscle, brain, and cancer as mentioned earlier [20, 21, 39-62]. The CDE is defined by [63]:

$$\left[\nabla \cdot D(\boldsymbol{r})\nabla - v\mu_a(\boldsymbol{r}) - \frac{1}{3}\alpha v\mu_s'(\boldsymbol{r})k_0^2\langle\Delta r^2(\boldsymbol{r},\tau)\rangle\right]\mathrm{G}_1(\boldsymbol{r},\tau) = -vS(\boldsymbol{r}) \qquad (1.4)$$

with autocorrelation decay time τ (s) and wavenumber k_0. The mean-square displacement (MSD) $\langle\Delta r^2(\boldsymbol{r},\tau)\rangle$ describes the motion of scattering particles (e.g., primarily moving red blood cells in tissues or Intralipid® emulsions in phantoms) in time τ. Another factor, α, accounts for the generally unknown ratio (between 0 and 1) of moving to total scatterers. In practice, we approximate a collimated source as a diffuse point source one scattering distance into the sample, $1/\mu_s'$ [64].

The solution to **Equation 1.4** for semi-infinite geometry provides the form of G_1 encountered on media such as the slabs used in experimental phantoms and as

an approximation on many real tissues. The corresponding semi-infinite solutions to **Equations 1.1 – 1.3** are of similar form and can be found elsewhere [22, 38]. The semi-infinite solution for G_1 is [65]:

$$\mathrm{G}_1(\rho,\tau) = \frac{vS_0}{4\pi D}\left[\frac{\exp(-r_1 M)}{r_1} - \frac{\exp(-r_2 M)}{r_2}\right] \tag{1.5}$$

where $M^2 = 3\mu_a\mu_s' + {\mu_s'}^2 k_0^2 \alpha\langle\Delta r^2(\tau)\rangle$, $r_1 = \sqrt{\rho^2 + (z - z_0)^2}$, $z_0 = 1/\mu_s'$, $r_2 = \sqrt{\rho^2 + (z + z_0 + 2z_b)^2}$, $z_b = 2(1 + R_{eff})\,/3\mu_s'(1 - R_{eff})$, $R_{eff} = -1.440n^{-2} + 0.710n^{-1} + 0.0636n + 0.668$ accounts for the refractive index mismatch between air and the medium, $n \approx 1.33$ for tissues and tissue-like phantoms, $\rho = |\boldsymbol{r} - \boldsymbol{r}_s|$ is the source-detector (SD) separation with source position $\boldsymbol{r}_s$ on the sample surface, and S_0 is the source term. The MSD in tissues is often modeled by Brownian motion where $\langle\Delta r^2(\tau)\rangle = 6\tau D_B$ with the effective diffusion coefficient of moving scatterers D_B. The αD_B term is collectively referred to as the blood flow index, BFI, which has been validated against multiple modalities including laser Doppler flowmetry [66, 67], Doppler ultrasound [68, 69], power spectral Doppler ultrasound [60], Xenon CT [70], arterial-spin-labeled MRI [71], and fluorescent microsphere flow measurement [72].

A single semi-infinite DCS measurement typically collects the normalized intensity autocorrelation function, $g_2(\rho)$, at a specific SD position ρ by hardware or software correlator processing of avalanche photodiode (APD) photon counts at multiple correlation times. This function can be fit to the normalized $g_1(\rho, 0)$ of **Equation 1.5** for quantifying αD_B. The Siegert relationship $g_2(\tau) = 1 + \beta|g_1(\tau)|^2$

can relate the intensity (measured) and electric field (model) autocorrelation functions where β is subject to the speckle and collection optics [73]. Fitting the curve for BFI and β simultaneously has been shown to improve results [74]. Optical fiber selection impact on DCS and other diffuse technologies has also been reported [75]. We use a novel FEM flow reconstruction method for imaging based on the PDE implementation, outlined in detail in **Chapter 2**.

1.6 Current Limitations and Thesis Outline

It is foreseen that a new single imaging instrument divulging both blood flow and fluorescence distributions in deep tissues is both necessary and desired to push forward into new potential research investigations. In a recent study, a relationship between tumor blood flow and nanoparticle deposition according to liposome size was found [76]. Thus, the 3D imaging of crucial detailed information about tumor tissue microvasculature and fluorescently-tagged nanoparticle spatial heterogeneity may significantly enhance realizable treatment efficacy of drug delivering nanoparticles. That study exemplifies the potential new facets of cancer research and highlights the difficulties. Imaging was performed with both dynamic contrast-enhanced computed tomography (DCE-CT) and fluorescence molecular tomography (FMT) requiring manual co-registration, landmark fiducials, and carefully interpreting the data acquired separately.

An instrument is thus proposed based on diffuse optical methods with multimodal flow and fluorescence capabilities. It will perform medical investigations within the NIR paradigm of diffuse optics, be relatively low cost and portable, have

robust sampling density and time, and obviate co-registration and related complications. Further desirables will include constraints that it be noncontact to avoid hemodynamic alterations [77-79] and reflectance-mode operation for translatability across subjects of varying sizes (i.e., small animals to humans). It would additionally be expandable to measure absorption and related derivatives.

The extension of diffuse optical spectroscopies to tomographic imaging has brought with it an ascension in multimodal imaging opportunities. Despite extensive progress, there has been an absence of a device which aggregated all the proposed features. Specifically, a fully noncontact multimodal diffuse optical instrument employed in reflectance-mode for the gathering of flow and fluorescence 3D distributions has yet been missing in the field. The development of such an instrument is the primary objective of this dissertation. The facilitation of a fully noncontact system requires moving the source and detection elements away from the tissue surface. Noncontact DOT/DFT systems have been previously developed using CCD cameras away from the interface [80-83]. No such systems have yet combined a reflectance design with CCD-based deep tissue flow imaging. This absent solution is due in part to the lack in developments of the latter.

Early DCT implementations have relied on the monitoring of light by high temporal resolution APD's to establish a correlation curve to fit the theoretical solution (**Equation 1.5**) [63, 84-86]. This type of detection element can be restrictive in its cost, scaling to high density sampling, and physical space overhead. As an alternative, CCD camera's offer a cost-effective solution to these limitations. CCD detection for flow imaging has already been employed abundantly

in techniques such as laser speckle contrast imaging (LSCI) [87, 88]. In comparison to our objectives, LSCI methods are largely used to probe superficial vascular distributions (up to 1 mm depth) with a wide-field illuminated light source [89, 90]. The extension of speckle contrast to the monitoring and imaging of deep tissues has been explored by several groups recently and replace the wide-field illumination with a point-like light source. The approach of diffuse speckle contrast analysis (DSCA) is to directly monitor inverse speckle contrast variations as a measure of the proportional change with the DCS BFI in the range of typical tissue properties [91-93]. Speckle contrast optical spectroscopy (SCOS) and tomography (SCOT) have been developed relating the speckle contrast parameter and DCS theory [94, 95]. The SCOT imaging uses perturbation and the Born approximation to establish the sensitivity relationship between changes in flow dynamics directly to speckle contrast and was tested in the transmission mode.

As mentioned in **Chapter 1.5** we have developed a novel flow reconstruction method. In our approach to CCD-based speckle contrast flow imaging, we retain our flow reconstruction advantages while deriving a link between it and speckle contrast flow measurements. This leverages our inherited reconstruction benefits from DOT developments due to the CDE/PDE equation and solution similarities while also accomplishing the utilization of a CCD camera for light detection of speckle contrasts. The speckle contrasts can be converted to boundary BFI which can then be input into the established FEM-based reconstructions and thereby amalgamate the robustness of CCD detection and previous/future flow imaging advancements.

Combining these advances with a noncontact light source and established DOT/DFT techniques, we expect that the resulting pioneered completely noncontact CCD-based system will synergize the benefits of all and provide a powerful new imaging technique for cancer research. In this study we incorporate the necessary theoretical advancements, hardware and software modifications, and preliminary testing to instantiate the highly translatable noninvasive imaging device that will serve as a robust segue between animal and human/clinical studies. This new technique allows for an accessible multiparameter data set without the complexities of image coregistration and multiple instrumentation data acquisition. The potential applications of this new device include the *in vivo* characterization of tumor detection and growth by flow distributions and those of ICG as well as opening the analysis on the relationship between fluorescently-tagged nanoparticles of varied size and localized flow differences.

The chapter outline of this thesis is as follows. The instrumentation is progressively developed in three stages: noncontact diffuse correlation tomography (ncDCT), speckle contrast diffuse correlation tomography (scDCT), and noncontact speckle contrast diffuse correlation tomography and diffuse fluorescence tomography (nc_scDCT/DFT). **Chapter 2** describes the ncDCT flow imaging instrumentation, complex boundary acquisition, our flow reconstruction method, and provides the results of a case study of ncDCT application on small animal tumors. **Chapter 3** presents the derived theoretical relationship between diffuse speckle contrast and the normalized temporal autocorrelation function and the modified instrumentation for CCD-based detection, termed scDCT, and its

phantom validation. **Chapter 4** follows with the multimodal reflectance-based nc_scDCT/DFT device prototype and its experimental validation. All personal contributions are more specifically relayed, along with overall study limitations and perspectives, in the closing **Chapter 5**.

CHAPTER 2 NONCONTACT DIFFUSE CORRELATION TOMOGRAPHY

2.1 Introduction

ncDCT serves as our flow imaging instrumentation progenitor and the foundational methodology upon which advancements are made in the following chapters. The novelty of ncDCT can be conceptualized as the straightforward transition from its stationary predecessor, noncontact diffuse correlation spectroscopy (ncDCS), to enable noncontact flow imaging. Accomplishing this goal thereby inherits the benefits of being noncontact and reflectance mode. ncDCS has been evaluated in simulations, tissue-like phantoms, forearm tissue cuff occlusions and head and neck cancer free tissue transfer flaps [96-98]. The ncDCT methods outlined in this chapter have been tested in simulations, phantoms, and real tissues including human breast tumor [20, 85, 99-101].

In this chapter we begin by examining the ncDCT hardware specifications and operation. An understanding of this implementation highlights the importance of our modifications in later chapters. Measuring and incorporating complex boundaries and finding source and detector surface coordinates is addressed for completeness. While a necessity in many real tissue encounters, this task is comparatively negligible in simple phantom models. Next are details of the FEM flow reconstruction method. This method is utilized throughout the thesis for flow reconstructions. As it is based on readily available open source software (NIRFAST, Dartmouth College, NH), seamless integration of geometries and

inversion algorithm techniques is promoted. The chapter will conclude with the application of ncDCT to an *in-vivo* mouse tumor study.

2.2 Instrumentation

A lens-based focusing apparatus suspended from a boom arm orchestrates the collection of boundary flow measurements (**Figure 2.1**) [20, 85, 97, 98]. The apparatus bookends a linear array of 15 single-mode detector fibers (SM800-5.6-125, Fibercore, CA) with 2 multimode source fibers (WF200/220/245, CeramOptec, MA) allowing for a 10 – 30 mm SD range and separate source and detector paths. The source paths consisted of two lenses (each) to collimate then focus the source light onto the sample surface. The detector path guided collimated light onto detector fiber tips after having passed through a 750 nm long-pass filter (FEL0750, ThorLabs, NJ) and aperture upon collection by an achromatic focusing lens. Detector fibers were connected to a bank of avalanche photodiodes (PerkinElmer, Canada). The APD intensity autocorrelation functions were simultaneously and dynamically processed by a multiple channel autocorrelator (Correlator.com, NJ). Each source fiber connected to an 830 nm long coherence laser (coherence length > 5 m; CrystaLaser, NV). A linear (T-LSM200A, Zaber, Canada; 5236A16, McMaster-Carr, IL) or rotational (CR1-Z7, Thorlabs, NJ) stager impressed mechanical translations to scan an ROI with an adjustable step size.

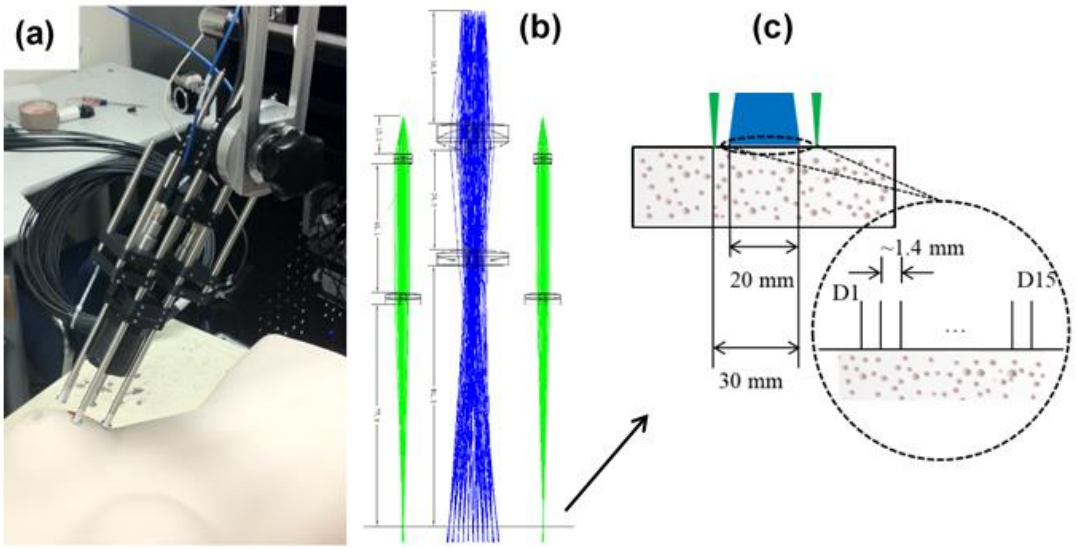

Figure 2.1: ncDCT instrumentation. The (a) lens-based focusing apparatus is positioned above a sample and scans over an ROI through mechanical translation to acquire a set of boundary flow data. (b) Light is projected by two individual source paths and collected by a linear array of detector fibers. (c) A single scan step provides SD separations from 10 – 30 mm for each of the two separate sources.

2.3 Complex Boundary Acquisition and Source/Detector Placement

The FEM reconstruction requires the incorporation of a finite element mesh representative of the sample and the surface coordinates of source and detector positions. In the simplest cases we may form a mesh from simple geometries such as a slab with built-in NIRFAST functionality and use the straightforward SD projections on a flat surface. In the case of real tissues, we aren't gifted with such ideal circumstances and use more involved methods. Contemporaneously with

ncDCT device development both the surface geometry and SD positioning concerns were addressed [20, 99].

To acquire the real sample geometry, a photogrammetric scanner (**Figure 2.2**; NextEngine, CA) proves a suitable solution. This 3D camera is oriented at an approximate working distance of 17 inches with a corresponding 10 inch × 13 inch field of view (FOV). Once stationed, the 3D surface mesh is acquired using the camera control software (ScanStudio HD, NextEngine, CA) and will include a reference plane and reference markings which have been manually placed by marker pen on the subject during ncDCT measurement. The markings generally correspond to the beginning, middle, and end step source positions for identifying the ncDCT lens apparatus translations (i.e., the SD arrangement and step length are static). A solid model is created by extruding a 2D contour (SolidWorks, Dassault Systemes, MA), where the shape chosen is based on sample similarity (i.e., circular for breast, rectangular for mouse), starting at the desired depth below and extending into the surface mesh. The finished solid volume must be of adequate size to allow diffusive photon propagation without creating a mesh of substantial processing burdens in reconstructions. From this solid, a 3D mesh was generated using ANSYS® (ANSYS, PA) with an appropriate average node distance (i.e., 1 or 2 mm based on previous experiments) and element shape (e.g., 4-node tetrahedron). In this step, localized mesh refinement (or other advanced options) can be carried out.

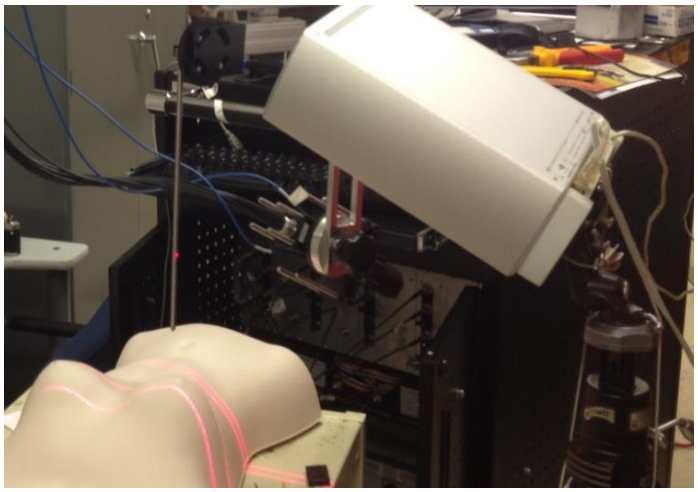

Figure 2.2: Photogrammetric scanning camera. The 3D camera positioned over a mannequin exemplifying surface geometry recovery scanning.

In noncontact-based applications the source and detection surface locations are not always as evident in comparison to contact designs. Mapping the projected source and detector positions is possible using the volume created by the 3D camera/extrusion and the source location reference markings. A program written to advantage the SolidWorks application programming interface (API) determines the positions in the following fashion. A plane is created perpendicular to the bottom plane (e.g., used for extrusion) whereby a line is created connecting the two source positions at an individual step. The program scans chief optical rays from the line to the sample surface with intersections denoting the proper SD coordinates. Errors of this method for alignment (< 10% error) were found to be negligible by simulated recovery of heterogeneity location (0.77 mm deviations < 1 mm node distance) and flow contrast (1% deviation) [99].

2.4 Flow Reconstruction

The basis of the flow reconstruction procedure resides in the PDE (**Equation 1.1**) and CDE (**Equation 1.4**) being analogous, which was the intent of the CDE [102]. The following **Table 2.1** comparison of the equations (P1 approximations; PDE shown for CW source) and partial-flux boundary conditions (also called Robin boundary conditions; incoming photon/correlation flux only due to Fresnel reflections at the interface) illustrates their formal similarity [22, 102, 103]:

Table 2.1: PDE, CDE, and boundary condition comparison

P1 Approximation Diffusion Equations	
Photon Diffusion	$[\nabla \cdot D(\boldsymbol{r})\nabla - v\mu_a(\boldsymbol{r})]\Phi(\boldsymbol{r}) = -vS(\boldsymbol{r})$
Correlation Diffusion	$[\nabla \cdot D(\boldsymbol{r})\nabla - v\mu_a^{total}(\boldsymbol{r},\tau)]\mathrm{G}_1(\boldsymbol{r},\tau) = -vS(\boldsymbol{r})$
Robin Boundary Conditions	
Photon Diffusion	$\Phi(\boldsymbol{m}) + z_b(\boldsymbol{m})\frac{\partial\Phi(\boldsymbol{m})}{\partial\hat{n}} = 0$
Correlation Diffusion	$\mathrm{G}_1(\boldsymbol{m},\tau) + z_b(\boldsymbol{m})\frac{\partial\mathrm{G}_1(\boldsymbol{m},\tau)}{\partial\hat{n}} = 0$

where we have replaced the second and third terms in the CDE with a total absorption which includes dynamic processes as $\mu_a^{total}(\boldsymbol{r},\tau) = \mu_a(\boldsymbol{r}) + \frac{1}{3}\alpha\mu_s'(\boldsymbol{r})k_0^2\langle\Delta r^2(\boldsymbol{r},\tau)\rangle$ and that when assuming moving scatterers undergoing Brownian motion becomes $\mu_a^{total}(\boldsymbol{r},\tau) = \mu_a(\boldsymbol{r}) + 2\mu_s'(\boldsymbol{r})k_0^2\alpha D_B(\boldsymbol{r})\tau$, $\hat{n}$ is normal to the surface, and the boundary conditions specify a boundary position $\boldsymbol{m}$. Although

the notation exhibits spatial variation in both optical properties and BFI, the flow reconstruction method to follow attributes all changes to $\alpha D_B(\boldsymbol{r})$.

As the analytic solutions for these equations are difficult to achieve except for simple cases, the problem is described by an FEM formulation which lends itself well to irregular boundaries and heterogeneous flow. The remaining details in this section are modified versions for flow (CDE) purposes from previous work done by others involving the FEM formulation, reconstruction implementations, and Jacobian calculation by adjoint method as originally outlined for photon fluence (PDE) and implemented in the NIRFAST (version 9.0) open source software package [104-107]. In FEM, we make the compromise of knowing the exact solution everywhere to that of an approximate numerical solution described in terms of a discrete set of elements and corresponding nodes. The FEM formulation derives a useful alternative problem formulation which provides the equivalent (approximate) solution to the CDE while allowing us to adjust the parameter surrogates. By continuously reducing the element size or increasing the nodal density, we expect ideally to effectively approach the exact solution for arbitrary media.

The physical domain Ω is first partitioned into L nonoverlapping volume (for our 3D objective) elements E_i joined at 4 vertex nodes N_i (for 4-node tetrahedrons) with $E_i: i = 1 \dots L$, $N_i: i = 1 \dots 4$, and the entire region is then constructed from $\Omega = \cup_{i=1}^{L} E_i$. Also required is an estimate of the continuous physical distribution of the function of interest (e.g., G_1). A piecewise linear polynomial shape function is thus defined with $\psi_i(N_j) = \delta_{ij} = \begin{cases} 1 & i = j \\ 0 & i \neq j \end{cases}, i, j = 1, \dots, P$ where $\{\psi_i\}_1^p$ denotes a basis

function set with the total number of mesh nodes P and has limited support (i.e., contributions only from elements sharing node N_i). The approximate solution G_1^h is then defined in terms of the basis as $G_1^h(\mathbf{r},\tau) = \sum_{i=1}^{P} G_{1,i}(\tau)\psi_i(\boldsymbol{r})$. There are no inherent mechanical relationships of significance between the nodes and G_1 and thus no displacement occurs during analysis. This does not imply external factors haven't inadvertently altered the true geometry such as subject movement or tissue compression during real measurements.

The ability to establish the actual FEM solution is derived in detail for the analogous PDE elsewhere [64, 104, 105, 107-109]. Briefly, integrations are performed over each element and the total nodal contributions summed (based on limited support). The governing equations are given below where ψ_i is related to G_1 being expressed in terms of the basis and ψ_j is a trial function, resulting in a (sparse) $P \times P$ "mass" matrix and $P \times 1$ source and solution vectors:

$$[\boldsymbol{K}(D) + \boldsymbol{C}(\mu_a^{total}) + \zeta\boldsymbol{F}]\mathbf{G_1}(\tau) = \boldsymbol{S_0} \tag{2.1}$$

$$K_{ij} = \int_{\Omega} D(\boldsymbol{r})\nabla\psi_i(\boldsymbol{r}) \cdot \nabla\psi_j(\boldsymbol{r})\, d\Omega \tag{2.2}$$

$$C_{ij} = \int_{\Omega} \mu_a^{total}(\boldsymbol{r},\tau)\psi_i(\boldsymbol{r})\psi_j(\boldsymbol{r})\, d\Omega \tag{2.3}$$

$$F_{ij} = \int_{\partial\Omega} \psi_i(\boldsymbol{r})\psi_j(\boldsymbol{r}) d(\partial\Omega) \tag{2.4}$$

$$S_i = \int_\Omega \psi_i(\boldsymbol{r}) S_0(\boldsymbol{r}) d\Omega \tag{2.5}$$

where $\zeta = 1/2A$ is arrived at by applying the Robin boundary condition to a boundary measurement defined by $\Gamma(\mathbf{m}) = \hat{\boldsymbol{n}} \cdot \boldsymbol{J}_{\boldsymbol{G_1}}(\boldsymbol{m})$ with normal surface vector $\hat{\boldsymbol{n}}$ and correlation flux $\boldsymbol{J}_{\boldsymbol{G_1}}$ at position $\boldsymbol{m}$ [102, 104, 107], and $\boldsymbol{G_1}(\tau)$ is the solution vector for nodal $G_1(\tau)$. The integrations are evaluated by methods such as quadrature. The forward solution can be extracted manually or with the versatile MATLAB® (MathWorks, MA) slash operator for the typical $\boldsymbol{Ax} = \boldsymbol{b}$ equation. Note that this entire arrangement is used to retrieve results in reference to a single source application/position.

An inverse problem is required for taking our measured G_1^M boundary data and finding the flow (technically the total absorption, μ_a^{total}, is reconstructed) distribution which produced it. The approach in the modified NIRFAST follows a Tikhonov minimization with [105]:

$$\chi^2 = \min_{\mu_a^{total}} \left\{ \sum_{i=1}^{B} \left[G_{1,i}^M(\tau) - G_{1,i}^C(\tau) \right]^2 + \lambda_T \sum_{j=1}^{P} \left[\mu_{a,j}^{total}(\tau) - \mu_{a,0}^{total}(\tau) \right]^2 \right\} \tag{2.6}$$

with B boundary measurements (all valid SD pairs), G_1^C is the forward solution, and a regularization parameter λ_T decreases the updated total absorption contribution each iteration. The resulting update is ultimately given, with the addition of a Jacobian sensitivity matrix J, by a Levenberg-Marquardt, $\delta\mu_a^{total} = \left(J^T J + \overline{\lambda_T} I\right)^{-1} J^T \delta G_1$ with $\overline{\lambda_T} \equiv 2\lambda_T$, or Moore-Penrose, $\delta\mu_a^{total} = J^T (JJ^T + \lambda_T I)^{-1} \delta \mathrm{G}_1$,

procedure depending on the (secondary mesh) node and boundary measurement quantities. Further details of this implementation are given analogously for optical properties in the NIRFAST papers [105, 110]. Iterations are ended after ≤ 2% projection error between the measured and forward model boundary data. The reconstructed μ_a^{total} is then finally used to extract the spatial distribution of $\alpha D_B(\boldsymbol{r})$. We retain the logarithmic transformation on G_1 with the assumption that there is a large dynamic range of the data [104]. The Jacobian is formed with an adjoint method as summarized next.

With the analogous (CW) diffusion equations and boundary conditions (**Table 2.1**), the boundary measurement sensitivity is restated here in terms of G_1 and total absorptions changes, within the FEM framework and utilizing the reciprocity relation, as [104, 106, 111]

$$\frac{\partial[\Gamma(\tau)]_j}{\partial \mu_{a,k}^{total}} = -\boldsymbol{\Psi}_{\mathbf{i}}^{\boldsymbol{T}}(\tau)\boldsymbol{V}_k\boldsymbol{G}_{\mathbf{1},\boldsymbol{j}}(\tau) = -\boldsymbol{G}_{\mathbf{1},\boldsymbol{j}}^{\boldsymbol{T}}(\tau)\boldsymbol{V}_k\boldsymbol{\Psi}_{\mathbf{i}}(\tau) \tag{2.7}$$

where $\boldsymbol{G}_{\mathbf{1},\boldsymbol{j}}$ corresponds to the CDE forward solution with $\boldsymbol{r_j}$, $V_{k,ij}(\mu_a^{total}) = \int_\Omega \psi_k(\boldsymbol{r_j})\psi_{\mathrm{i}}(\boldsymbol{r_j})\psi_{\mathrm{j}}(\boldsymbol{r_j})\mathrm{d}\Omega$ is a basis system matrix arising from the expression of the total absorption in basis form $\mu_a^{total}(\boldsymbol{r_j},\tau) = \sum_{k=1}^{P}\mu_{a,k}^{total}(\tau)\psi_k(\boldsymbol{r_j})$, and $\boldsymbol{\Psi}_{\mathbf{i}}$ is the solution to the CW adjoint problem $[\mathbf{K}+\mathbf{C}+\zeta\mathbf{F}]\boldsymbol{\Psi}_{\mathrm{i}} = \boldsymbol{S}_i^+$. In this latter problem S^+ is a δ-function source of type "Robin" (see **Table 2.1** boundary conditions) at the measurement position $\boldsymbol{m_i}$. The source has been tacitly assumed constant with

respect to changes in μ_a^{total}. The sensitivity from **Equation 2.7** can finally be applied to form the Jacobian matrix considering all valid SD pairs.

Throughout the description of this flow reconstruction technique we have largely left the role of correlation time τ unaddressed. In practice, we select a single τ leaving the reconstruction procedures nearly identical to the original PDE implementations. The choice for this parameter, the implications of μ_a and μ_s' contributions to the total absorption, and forward and inverse solution validations for ncDCT relative flow imaging has been examined in detail elsewhere [85, 112]. It may also be noted that μ_a^{total} is a function of τ as is an implicit $\exp\left(i\frac{2\pi c}{\lambda}\tau\right)$ on the CDE source term and should be taken into account in future analyses where the correlation time is not held constant in reconstructions [103].

2.5 Observations and Limitations

There are several limitations with the ncDCT implementation. Although the lens apparatus may be scanned along the surface increasing lateral/rotational density, the linear SD array itself is static. This inhibits transitioning among subjects and ROI's of varying sizes and restricts the ability to increase longitudinal SD density. The SD coverage is improved by mechanical scanning, but this movement is time consuming (up to 20 minutes). Artifacts due to subject and stager movements and potential physiological variations from the protracted duration may be introduced. Further difficulties occur in scaling the design to a greater number of SD pairs and patterns. Optical fibers and APDs incur inhibitive physical overhead with increasing number and the associated costs could have diminishing

returns. Such setups can also become exceedingly complex in accomplishing high spatial sampling density applications such as tomography. In the scDCT design we seek to remedy many of these shortcomings. Before moving on to this new design, a case study with ncDCT on a mouse tumor model is presented.

2.6 Flow Imaging of Mouse Tumors with ncDCT

In this investigation, we examine the flow contrasts between healthy and tumor tissue in a small animal model with ncDCT. Potential disadvantages of many current imaging techniques include costs and sensitivity only to morphological advancements. The microenvironment following rapid tumor growth is marked by enhanced angiogenesis and metabolic demand [1]. Functional physiological changes thus may serve as important biomarkers. The abnormal blood flow of such diseased tissue may provide detectable contrasts with surrounding normal healthy tissues. Small animal tumor models are employed in device development due to their availability, ease of control, tumor access, reduced complexity, and lower cost than human tumors. Imaging applied to small animals can provide a rapid segue between *in-vitro* assay-based and *in*-vivo clinical research and potentially produce results with fewer animals than traditional methods [28, 29]. Small animals can provide a faster and more cost-effective mechanism for evaluating criteria of potential concepts prior to a clinical trial. Combining the ncDCT technique with a mouse mammary tumor model allows visualization of tumor region blood flow contrasts with surrounding healthy tissues.

2.6.1 Tumor Model

Human breast cancers commonly overexpress the ErbB-2 gene and breast cancer patients with high ErbB-2 have poor prognosis [113-115]. It has been found that ErbB-2 overexpression promotes hypersensitivity to ethanol [116]. Furthermore, ethanol has been found to encourage tumor growth and angiogenesis [117]. Due to its ethanol response, aggressive MDA-MB231 breast cancer cells may be investigated [117]. In the current case study, we employ ncDCT in measuring the blood flow characteristics of an athymic nude (NU/NU) mouse (Harlan Laboratories, IN) dorsally inoculated with aggressive MDA-MB231 breast cancer cells (2×10^6 cells per each of two sites). The tumors were allowed to grow until palpable and one had reached at least 5 mm in diameter to promote high flow contrasts. Measurements were then acquired by ncDCT on two separate days denoted as Day 1 and Day 4. Mice were euthanized following the last measurement. All procedures were carried out according to the guidelines for the care and use of laboratory animals implemented by the National Institutes of Health and the Guidelines of the Animal Welfare Act approved by the Institutional Animal Care and Use Committee of the University of Kentucky.

2.6.2 Data Collection

Each measurement consisted of the following protocol. The mouse was first anesthetized through intraperitoneal injection. The animal was secured into position with its ventral side on a platform. The platform (excluding the mouse) was

covered to help minimize ambient light contributions. The ncDCT device as outlined in **Chapter 2.2** is arranged longitudinally with the one laser source projected near the neck and the other the tail as shown in **Figure 2.3**. Data is collected at 16 steps as the lens apparatus is mechanically scanned in 1.0 mm increments transverse to the head-tail orientation. At each step data was acquired at 0.5 Hz sampling with 15 s collection for each source, alternately. This data was fit using **Equation 1.5** and the Siegert relation for a complete set of boundary BFI. The actual source positions were marked on the animal after the first and last step for SD coordinate calculations.

Figure 2.3: ncDCT mouse tumor data acquisition. Illustration of the mouse orientation with respect to ROI, noncontact probe alignment, and scan direction.

Following ncDCT, photogrammetric scanning of the mouse curvature was taken, and a mesh was then created. The mesh was combined with the boundary data and calculated SD positions for flow reconstruction. The corresponding mesh of bounding dimensions (mm) [Day 1: 45.6 (H) × 21.4 (W) × 24 (D); Day 4: 46.7 (H) × 18.4 (W) × 22.4 (D)] with nodes [Day 1: 25,610; Day 4: 20,885] of average 1.00 mm node distance is shown in **Figure 2.4** for both days with visualized SD locations. These complex boundary and mesh steps followed the methods described in **Chapter 2.3**. Of the total SD combinations, only pairs which coincide with each step of the linear apparatus positioning are valid resulting in 480 boundary measurements (2 sources × 15 detectors × 16 steps). A secondary pixel basis mesh of [25 25 25], single delay time of $\tau = 3.2 \times 10^{-6} s$ [85], and optical properties of $\mu_a = 0.03\ mm^{-1}$, $\mu_s' = 1\ mm^{-1}$ were used in reconstructions.

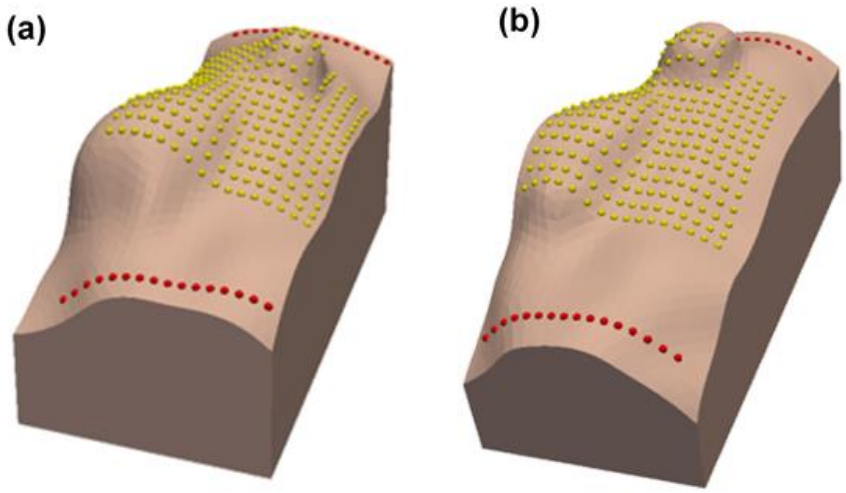

Figure 2.4: Coverage of source and detector locations on the mouse. The source (red spheres) and detector (yellow spheres) locations are shown for the (a) first day and (b) fourth day.

2.6.3 Results

A region of known healthy tissue was used for normalization to produce tumor-healthy relative blood flow [$rBF = \left(\alpha D_B / \alpha D_{B,0}\right) \times 100\%$; $\alpha D_{B,0}$ from healthy region] contrasts. From the tomographic reconstructions, a threshold of two standard deviations above the mean was used to separate the abnormal/tumor tissue flow from that of healthy tissues. Visual inspection supplemented the quantitative segmentation by manually categorizing regions as that of the large tumor, small tumor, or artifacts based on the known tumor palpations. In agreement with expectations, segmented regions were primarily limited to regions of tumor growth for both days as evidenced in **Figure 2.5**. There are two uniquely identifiable tumors on both occasions.

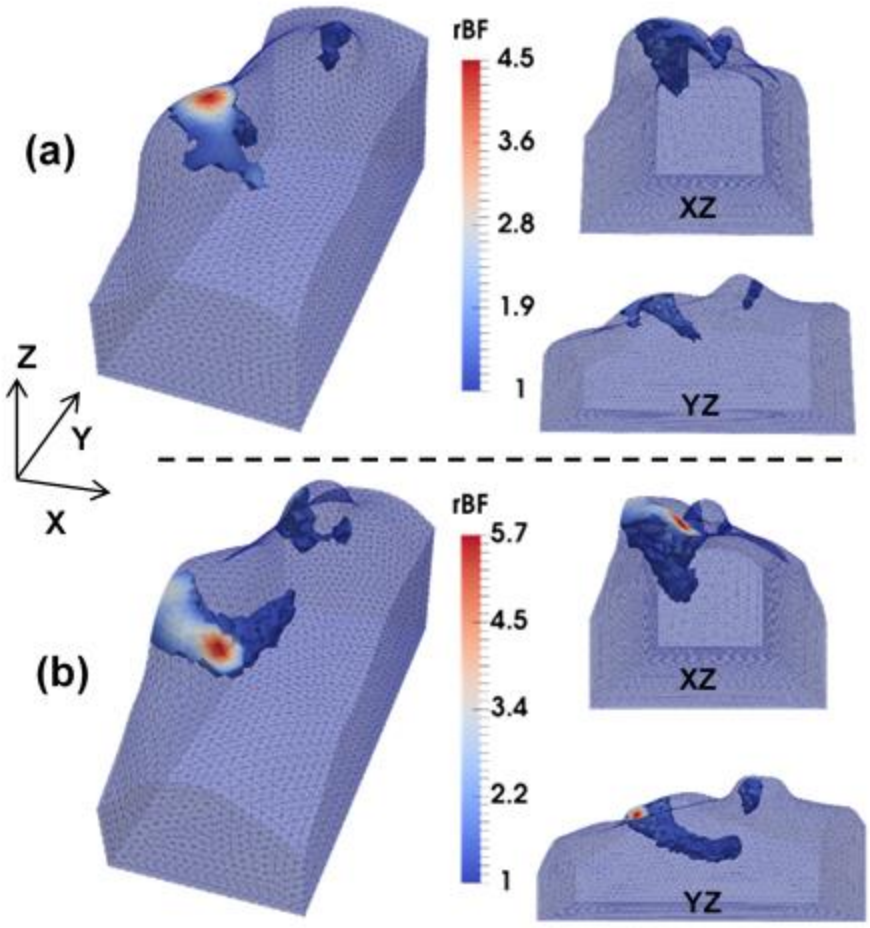

Figure 2.5: ncDCT mouse tumor reconstruction. The segmented 3-D tumor relative blood flow (rBF) contrasts for (a) day 1 and (b) day 4 are shown. Perspectives normal to the XZ and YZ plane are also shown (right).

The tumor volumes (V) and average relative tumor-healthy blood flows ($\overline{rBF}$) were quantified using the segmented and separated tumor data and listed in **Table 2.2**. The tumor volumes both increased over the four days duration with an observed ~1.75- and ~3-fold change in the large and small tumors, respectively. The tumor blood flow averages exhibited a discrepancy between the large and small tumors. The smaller increased 25% while the larger decreased 10%.

Table 2.2: Recovered mouse tumor characteristics

	Large Tumor		Small Tumor	
	V (mm^3)	$\overline{rBF}$	V (mm^3)	$\overline{rBF}$
Day 1	155.82	1.78 ± 0.78	11.82	1.20 ± 0.09
Day 4	276.40	1.60 ± 0.70	34.84	1.50 ± 0.42

2.6.4 Observations and Limitations

The trend in tumor volumes from **Table 2.2** for both tumors coincides with uncontrolled tumor growth. Further elevations in tumor volumes is anticipated to be minimal due to practical circumstances. Specifically, the tumors can begin to present with open wounds and the mouse subject will experience discomfort soon after the sizes observed. The varied average tumor blood flow is reasonable as the inside of solid tumors can develop poor circulation and even necrotic regions due to lack of nutrients and inadequate vessel structures. The resolution of ncDCT may not easily discern such regions until they grow to mm sizes but is still influenced by the partial volume effects on the boundary measurements. The average tumor flow contrast with healthy human breast tissues as measured by DCS and ncDCT *in vivo* have been reported between 2- to 10-fold [20, 58, 59]. The average flow contrast measured herein is just under this range. Some discrepancies due to partial volume effects, breast tumors in a mouse model, and lack of optical property information will contribute to inaccuracies in flow estimations [112, 118]. Overall, the application of the ncDCT technique to imaging small animal (mouse) mammary tumor blood flow contrasts was supported by this

case study. The regions of tumor tissues were identified and found localized proximal to their true locations. Average blood flow distributions were characterized with positive success in agreement with literature.

There are areas where this study was limited and future optimizations which are both possible and necessary. The detection area being distributed across the entire animal is undesirable due to some asymmetry of internals (e.g., liver), large heterogeneity in tissue types and optical properties, large separation of SD combinations (i.e., SD sensitivity is typically half the separation distance), and laser source projections near the edges such as the neck and tail area. These deficiencies are predominantly due to the development of the ncDCT lens apparatus for human scale ROI's. The mouse body is several centimeters in length and pushes the lens focusing apparatus to the margins of its applicability. Future studies should narrow the ROI to a smaller region of tissue and SD separations which limit penetration and optimize sensitivity. In proceeding chapters, instrument design allows for this robust translational potential.

Measurement of the tissue optical properties can be accomplished through addition of DOS/DOT techniques to attempt further improvements in blood flow estimates. The absorption and reduced scattering coefficients used coincided with literature, but there is a large variation across tissue types [119-122].

The scan time, also addressed in proceeding chapters, is another undesirable system trait. The animal though secured and anesthetized has intermittent exaggerated respirations and twitches which can introduce artifacts over the scan

period of ~8 minutes. Reducing the data collection duration will help reduce the impact of these occurrences.

The modest boundary curvature makes suspect that there is consistent modeling with the semi-infinite solution (**Equation 1.5**). Monte Carlo (MC) modeling may improve the recovered data and understanding of the curvature and angle of incidence influences. A previous study noted curvature influence on absolute αD_B with a negligible affect on rBF [98]. Such analysis uses the form of g_1 explicitly including the path length distribution as obtainable from MC simulations. In future mouse studies an assumption of negligibility should be assumed invalid and require case-specific analysis. This is due to the spatial heterogeneity of curvature which will also change over time with a palpable tumor. The progression of size in the smaller tumor as seen in **Figure 2.5** is thus expected to supply less reliable results. Additionally, the separation for a particular SD pair as defined for the semi-infinite solution uses a flat boundary, but has ambiguous meaning (e.g., shortest direct distance or geodesic distance) and inaccurate applicability with regard to a curved boundary. Alternatively, limiting the ROI to a smaller area can reduce these effects with a sufficiently modified lens apparatus as mentioned above. A technique developed specifically for extracting DCS flow indices on complex curvatures has recently been developed and may be incorporated in future studies for flow boundary data reconciliation [123, 124].

Several other improvements may also be incorporated into future related studies. Further flow progression information can be made available by extending the longitudinal monitoring to earlier time points including early tumor growth. To

support the findings shown, validation should be performed against other modalities and/or techniques such as CD34/microvessel density after tumor excision. Lastly, a heating element is needed to assist in maintaining the animal body temperature and preventing flow changes throughout the measurement duration.

An uncertainty arose after the measurements were concluded concerning the source fiber attachments to the lens focusing apparatus. The source orientation (i.e., source 1 top/source 2 bottom or source 1 bottom/source 2 top) was determined by comparing usage of the ncDCT device in experiments near the relevant dates and the results for the 2 separate mouse measurement days. Several other mice were measured, but due to insufficient data for longitudinal/self-comparison and compounding complications in assumptions from the uncertainty above they were excluded from analysis.

CHAPTER 3 SPECKLE CONTRAST DIFFUSE CORRELATION TOMOGRAPHY

3.1 Introduction

In this chapter we proceed from APD's to CCD detection and develop the background for moving between speckle contrast flow measurements and our flow reconstruction technique while describing the system built for exemplification. As this method transitions raw flow measurements from intensity correlation to speckle contrast we term it speckle contrast DCT (scDCT). This unique system facilitates CCD-based 3D flow contrast imaging of complex turbid media. We first look at the scDCT instrumentation and how it is oriented for taking data in an experimental setup. Following this is the derivation of the speckle contrast flow detection in semi-infinite media which enables utilizing the CCD camera as opposed to APD's. We continue with the image pre-processing details including noise corrections and a smear correction algorithm. Finally, we apply this scDCT technique on reflectance-based measurements of tissue-like phantoms. The derivation [100] and system and experimentation [125] described herein have been published. A low cost compact spectroscopic alternative has also been proposed [126].

3.2 Instrumentation and Experimental Setup

In scDCT we replace the APD detection elements of ncDCT by a single highly sensitive electron-multiplying CCD (EMCCD; Cascade 1K, Photometrics, AZ). This

method of detection allows for many (e.g., up to ~1 million [1004 x 1002 pixels]; camera dependent) effective detector measurements due to the populated pixel grid. It also removes the scanning overhead and time penalty of the ncDCT design. The camera specifications are shown in **Table 3.1**. The maximum full frame rate achievable is ~9 frames per second (fps; we average ~8 fps in practice) without binning (up to ~33 fps with binning at the expense of resolution; no binning is used in the current investigation). The quantum efficiency of the camera is shown in **Figure 3.1**. The 785 nm long-coherence laser (coherence length > 5 m; CrystaLaser, NV) used coincides with a quantum efficiency slightly under 45% from the referenced figure. The camera backing is mounted to a heavy base seated upon a mobile cart which can be quickly moved between laboratory settings and clinical rooms. The reflectance mode orientation more adequately represents the situation encountered in larger subjects such as humans where transmission is not practical in most cases (due to the limited penetration depth of light), enhancing translatability to different ROI's and subjects (e.g., small animals).

Table 3.1: Cascade 1K EMCCD specifications

Specification	Details
Format	1004 pixels x 1002 pixels; 8 µm x 8 µm pixels
Linear full well single pixel	30,000e-
Digitizer	16 bits @ 10 MHz
Frame readout	110 ms/frame; 1 ms (image-to-storage shift time)

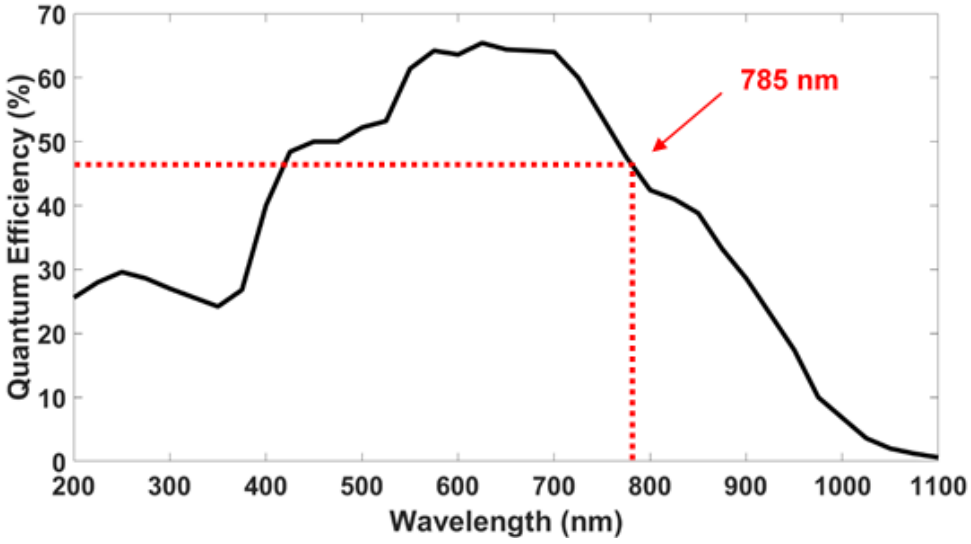

Figure 3.1: Quantum efficiency of the Cascade 1K EMCCD. The quantum efficiency corresponding to the 785 nm laser source is denoted by a dashed red line.

A zoom lens (Zoom 7000, Navitar, NY) is attached to the CCD camera opening as shown in **Figure 3.2a**. The lens is aligned concentrically to the FOV over a liquid phantom surface (**Figure 3.2b**). The zoom lens was set with a 35 mm focal length and F-number of 8 to make the focal plane agree with a tissue-like liquid phantom surface and to satisfy the speckle size Nyquist sampling criteria [127], respectively.

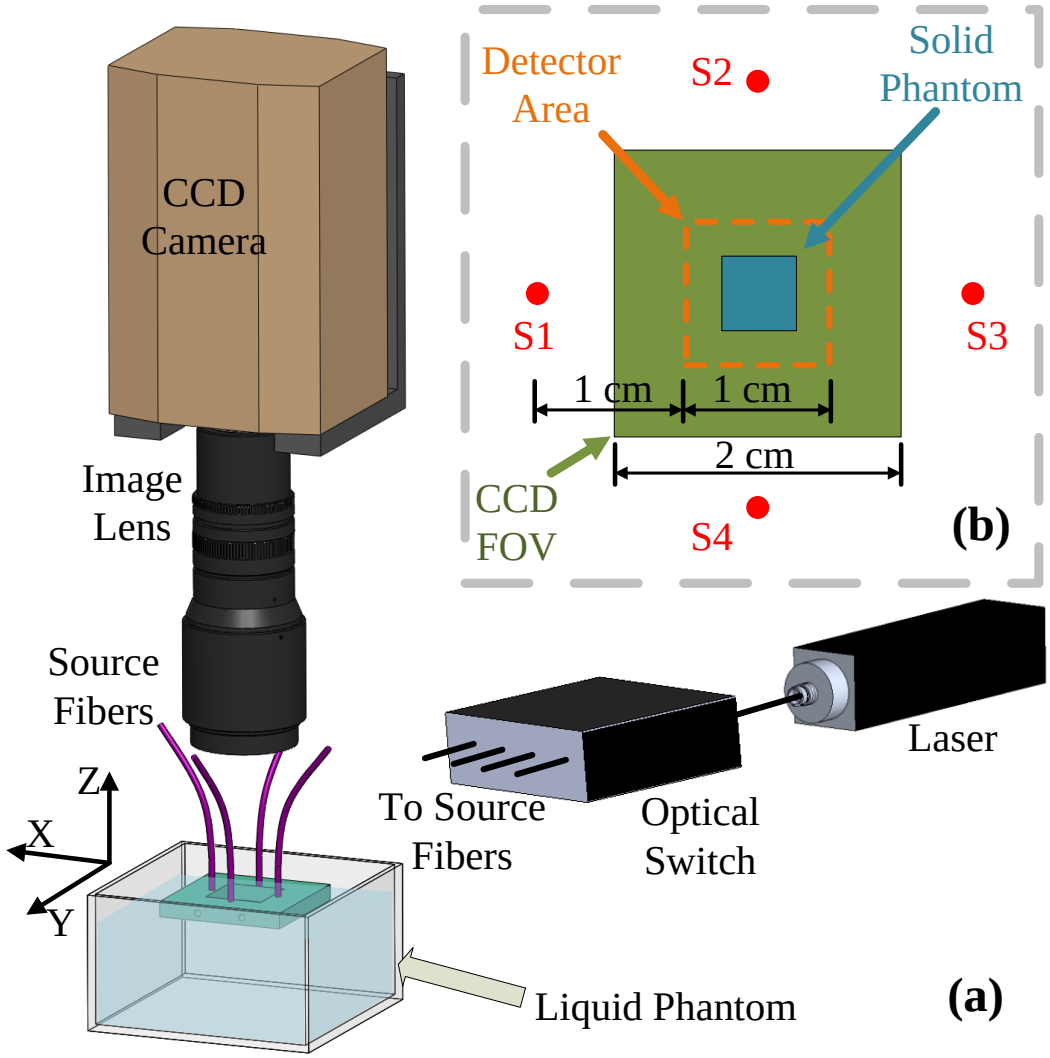

Figure 3.2: CCD camera and experimental setup. (a) The EMCCD is focused by zoom lens onto a liquid phantom surface. A square metal holder positioned the ferrule tips of four optical fibers on the liquid surface. The holder provided a 2.4 cm × 2.4 cm open area. The optical switch distributed laser light into the four source fibers sequentially. (b) Configuration of the four sources, CCD, FOV, solid phantom placement, and detector area.

A blocking fiber optic switch (VX500, DiCon, CA) was custom designed with two-channel inputs and four-channel outputs. Here we use it to deliver photons from a single laser input to four multimode optical fibers (FT200UMT, Thorlabs, NJ; 200 µm core fiber with 0.39 NA and FC/PC connector) individually (see **Figures 3.2a** and **3.3**). The 2 × 4 switching mechanism is reversible and can allow low-loss light throughput in the opposite direction in future applications. The switch is optimized for wavelengths in the range of 600 – 860 nm. The switch output fibers (S1 to S4 in Figure **3.2b**) were led to a metal holder with a 2.4 cm × 2.4 cm open center with their ferrule tips held in place symmetrically around the FOV perimeter. The effective positions were located 1.5 cm from the FOV edge centers. A LabVIEW® (National Instruments, TX) program was written to control the optical switch operation through an A/D board.

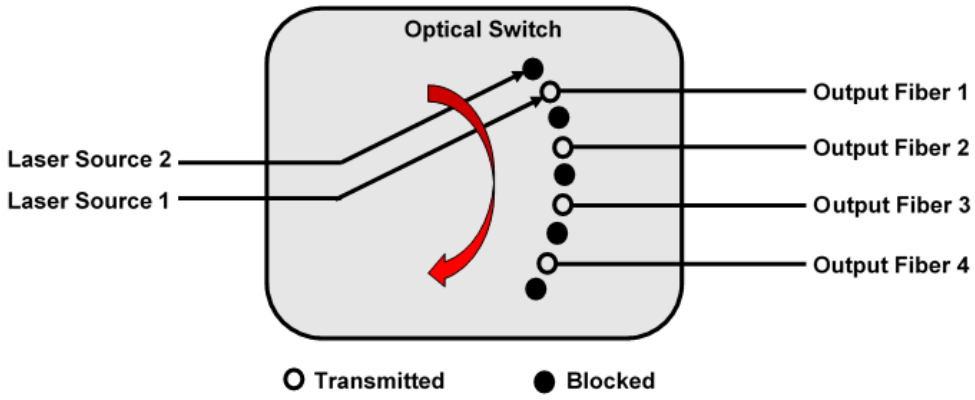

Figure 3.3: The blocking and switching mechanism of the optical switch. The 785 nm laser light was connected to input 1 and sequenced from output 1 through 4. The blocking feature restricts input 2 light from passing through any output channel when only input 1 light passage is desired (or conversely). No light source is connected to input 2 in the current investigation.

3.3 Speckle Contrast

To facilitate determination of blood flow indices by CCD detection we borrow a concept from LSCI termed speckle contrast. In typical LSCI a wide-field light source is applied across a region for monitoring superficial flow variations by quantifying the speckle contrast in a local region as [87]:

$$K_s(\boldsymbol{r}) = \frac{\sigma_s}{\langle I \rangle} \tag{3.1}$$

where σ_s is the spatial (or temporal) standard deviation and $\langle I \rangle$ is the mean intensity of a set of pixels (e.g., a window). We seek to extend this into speckle patterns created by photons having traversed diffusely up to a few centimeters depth within biological tissues. We thus turn to the following relationship (assumes the Siegert relation) between the speckle contrast parameter and g_1:

$$K_s^2(\boldsymbol{r}) = \frac{2\beta}{T}\int_0^T \left(1 - \frac{\tau}{T}\right) g_1^2(\boldsymbol{r}, \tau)\, d\tau \tag{3.2}$$

where T is the exposure time and β relates the detector and speckle sizes [128].

Using the normalized semi-infinite analytic solution $g_1(\boldsymbol{r}, \tau) = G_1(\boldsymbol{r}, \tau)/G_1(\boldsymbol{r}, 0)$ from **Equation 1.5** and rewriting we obtain

$$g_1(\boldsymbol{r}, \tau) = C[r_2 \exp(-r_1 M) - r_1 \exp(-r_2 M)] \tag{3.3}$$

where $C = \left[r_2 \exp\left(-r_1\sqrt{3\mu_a\mu_s'}\right) - r_1 \exp\left(-r_2\sqrt{3\mu_a\mu_s'}\right)\right]^{-1}$. Inserting **Equation 3.3** into **Equation 3.2**,

$$K_s^2(\boldsymbol{r}) = \frac{2\beta C^2}{T}\begin{bmatrix} \int_0^T \begin{Bmatrix} r_1^2 \exp(-2r_2M) \\ -2r_1r_2 \exp(-[r_1+r_2]M) \\ +r_2^2 \exp(-2r_1M) \end{Bmatrix} d\tau \\ -\frac{1}{T}\int_0^T \tau \begin{Bmatrix} r_1^2 \exp(-2r_2M) \\ -2r_1r_2 \exp(-[r_1+r_2]M) \\ +r_2^2 \exp(-2r_1M) \end{Bmatrix} d\tau \end{bmatrix} \tag{3.4}$$

which can be rewritten in terms of M as

$$\tau = \frac{M^2 - 3\mu_a\mu_s'}{6{\mu_s'}^2 k_0^2 \alpha D_B} \tag{3.5}$$

and

$$d\tau = \frac{M}{3{\mu_s'}^2 k_0^2 \alpha D_B} dM. \tag{3.6}$$

We can consider the integrals of the following two general forms with their corresponding solutions

$$A = \frac{1}{3{\mu_s'}^2 k_0^2 \alpha D_B} \sum_{i=1}^{3} x_i \int_a^b M \exp(y_i M)\, dM$$

$$= \frac{1}{3{\mu_s'}^2 k_0^2 \alpha D_B} \sum_{i=1}^{3} \left(\frac{x_i}{y_i^2}\right) [(y_i b - 1)\exp(y_i b) - (y_i a - 1)\exp(y_i a)] \tag{3.7}$$

and

$$B = \frac{1}{18{\mu_s'}^4 k_0^4 (\alpha D_B)^2} \sum_{i=1}^{3} x_i \int_a^b (M^2 - 3\mu_a\mu_s')M \exp(y_i M)\, dM$$

$$= \frac{1}{18{\mu_s'}^4 k_0^4 (\alpha D_B)^2} \sum_{i=1}^{3} \left(\frac{x_i}{y_i^4}\right) \left[\begin{pmatrix} {y_i}^3 b^3 - 3{y_i}^2 b^2 - {y_i}^3 b a^2 \\ +6y_i b + {y_i}^2 a^2 - 6 \end{pmatrix} \exp(y_i b) \right. \\ \left. +2({y_i}^2 a^2 - 3y_i a + 3) \exp(y_i a) \right] \qquad (3.8)$$

with $x_i = \begin{cases} r_1^2 & i = 1 \\ -2r_1 r_2 & i = 2 \\ r_2^2 & i = 3 \end{cases}$, $y_i = \begin{cases} -2r_2 & i = 1 \\ -(r_1 + r_2) & i = 2, \\ -2r_1 & i = 3 \end{cases}$ $a = \sqrt{3\mu_a\mu_s'}$ and $b = \sqrt{6{\mu_s'}^2 k_0^2 \alpha D_B T + 3\mu_a\mu_s'}$. The final solution is then

$$K_s^2(\boldsymbol{r}) = \frac{2\beta C^2}{T}\left[A - \frac{1}{T}B\right] \qquad (3.9)$$

The theoretical diffuse speckle contrast can be seen to be a function of several parameters, explicitly $K_s^2(\boldsymbol{r}) = f(\alpha D_B, T, \mu_a, \mu_s', \lambda, \beta, k_0, \boldsymbol{r})$. We assume that all parameters remain constant throughout the camera integration time. All parameters are known, measurable, or estimated from literature except for αD_B (i.e., the blood flow index, BFI). The relationship between the diffuse speckle contrast, SD separation, and exposure time T is nonlinear as shown in **Figure 3.4**.

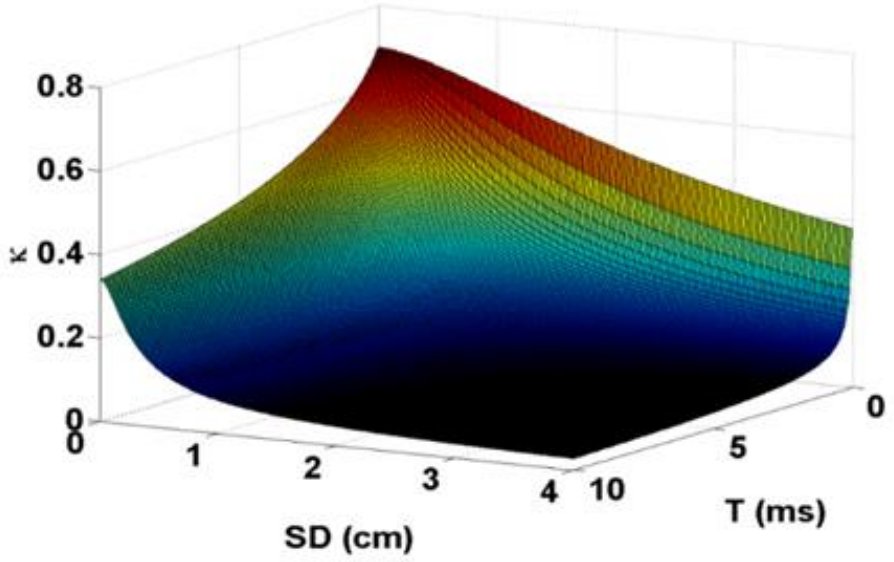

Figure 3.4: Variation in diffuse speckle contrast. Variations in speckle contrast are shown over a typical range of SD separations and exposure times T.

Extraction of the BFI for each SD pair is carried out as follows. The experimentally measured diffuse speckle contrast is calculated from CCD camera measurements by **Equation 3.1** with noise corrections, which we term K_{se} for illustrative purposes. The theoretical diffuse speckle contrast is calculated by **Equation 3.9**, similarly termed K_{st}^2. As BFI is unknown, we finally minimize the squared difference between the two speckle contrasts, $\min_{\alpha D_B}(K_{se}^2 - K_{st}^2)^2$, with respect to BFI.

The BFI obtained from this speckle contrast method by CCD detection is considered equivalent to that obtained from APDs and **Equation 1.5**. As such, reconstructing flow distributions is performed as described in **Chapter 2** with the difference only existing in the acquisition of the boundary BFI data.

3.4 Image Pre-Processing and Reconstruction

Prior to applying speckle contrast-based flow recovery, the raw images were preprocessed to account for several negative factors including smear and noise contributions. The speckle contrast obtained from a frame transfer EMCCD camera may deviate from the theoretical value due to intensity disorder originating from the frame transfer process [129]. More specifically, visual stripes (smears) are induced extending from bright features in the image into the direction opposite that of the charge transfer process. Along this direction, the smear can be corrected using an algorithm described by **Equation 3.10**. The actual pixel intensity signal of the xth column and yth row, $i(x,y)$, can be restored by the measured value $i'(x,y)$ with

$$i(x,y) = i'(x,y) - \frac{\eta_{ft} t_{ft}}{n_p T} \sum_{n=1}^{y-1} i(x,n) \tag{3.10}$$

where t_{ft} is frame transfer time, n_p is number of pixel rows when the frame has moved to the readout buffer, and η_{ft} is the efficiency with which photoelectrons are generated during the charge-transfer process relative to the efficiency with which photoelectrons are generated during the image capture period. Our EMCCD frame transfer time is ~1 ms. We set 7×7 windows at the same distance to the source location for a symmetric intensity distribution, leading to η_{ft} value of 0.67.

Speckle contrast contributions due to hardware noise (i.e., shot noise and dark noise) are accounted for correcting the speckle contrast computation (**Equation**

3.1) of windowed regions [94, 130]. Details of these corrections can be found elsewhere [94]. Briefly, dark images are used to mitigate speckle contrast influences from dark noise, $I_c = I - I_D$, where I is the original intensity of a single pixel and I_D is the intensity of dark current. The shot noise of I_C follows Poisson statistics, $\sigma_s(I_C) = \sqrt{\mu(I_C)}$, which are incorporated into the correction calculation. The shot and dark corrected speckle contrast is then given by

$$K = \sqrt{\frac{\sigma^2(I) - \sigma^2(I_D) - \sigma_S^2(I_C)}{\mu^2(I_C)}}. \quad (3.11)$$

The tomographic reconstruction process is the same as described in **Chapter 2** with the boundary BFI now provided as described in **Chapter 3.3** and above. A single delay time of $\tau = 3.2 \times 10^{-6}\, s$ was used [85]. The SD separation is determined for each effective detector as the center of the region covered by its associated pixels.

3.5 Experimental Protocol

Two types of tissue-like phantoms were incorporated for experimentation. The background consisted of a liquid phantom mixture comprised of distilled water, India ink (Black India 44201, Higgins, MA), and Intralipid (Fresenius Kabi, Sweden). This phantom maintained an effectively homogeneous set of optical properties comparable to real tissues as $\mu_a = 0.05\, cm^{-1}$ and $\mu_s' = 7.0\, cm^{-1}$ and flow from Intralipid particle Brownian motion as $D_B \cong 1 \times 10^{-8}\, cm^2/s$ (assumed

[118]). In our homogeneous liquid phantom experimentation all scatterers are dynamic ($\alpha = 1$) and we thus write D_B. For satisfying the need for flow contrast, a 7 mm side length cube-shaped solid phantom was created of carbon black (Alfa Aesar, IL), titanium dioxide (Alfa Aesar, IL), and silicone (Circuit Specialists Inc, AZ) [112]. Its associated properties supplied D_B about three orders of magnitude lower than the liquid phantom background while matching optical properties ($\mu_a = 0.05\ cm^{-1}$, $\mu_s' = 7.0\ cm^{-1}$). The cube was submerged at 2 mm depth beneath the surface in the FOV center.

The scDCT speckle contrast measurement protocol was identical for both the presence and absence of the solid cube in the liquid phantom background and was as follows. A source position was first selected with the optical switch. The CCD camera then acquired 30 frames at a frame rate of 8 fps while set at 2 ms exposure time. Collection of raw images was repeated in this manner for the remaining three source positions. A set of 9 × 9 detectors were defined and centered in the FOV over 1.0 cm × 1.0 cm (**Figure 3.2b**) surrounding the cubical target (when applicable). With the static source and defined detector positions, SD separations ranged from 1.0 to 2.0 cm with 1.25 mm detector separation distance. Each detector (0.42 mm × 0.42 mm) was comprised of 3 × 3 windows which in turn contained 7 × 7 pixels (8 μm pixel size). For each preprocessed image, the speckle contrast was calculated per window and subsequently averaged across all windows corresponding to their associated detector. Localized speckle contrast averages were then calculated along obtained frames for all sources.

Prior to heterogeneity inclusion, the homogeneous phantom was measured with scDCT and DCS for calibration purposes. Practically, the optical constant β for CCD is not available for measurement. Therefore, a DCS instrumentation was utilized with an APD-connected single-mode detection fiber (β = 0.5) to measure BFI as calculated by **Equation 1.5** and thus serving as the standard. This BFI was used with **Equation 3.9** providing the expected speckle contrast with unknown β (for CCD). As the sample was homogeneous with respect to the optical properties and BFI this enabled the determination of appropriate calibration factors at all SD separations.

3.6 Smear Correction Improvements and Speckle Contrast Flow Validation

The influences of smear correction are considered first. **Figure 3.5a** illustrates the intensity distribution with source S2 on the homogeneous phantom. The bias of intensity is evident in the direction of frame transfer (towards S2). **Figure 3.5b** shows the distribution after desmearing, demonstrating a normal presentation for point source intensity. To quantify the desmearing influence we consider an array of detectors defined along the center row in line with the source location as shown relative to S2 in **Figure 3.5a**. The number of effective detectors is increased to 21 along this line (see the ROI and dots in **Figure 3.5a**) for enhanced illustration of the smear influence. The detectors are otherwise defined as outlined previously. The SD ranges from 1.0 to 2.0 cm. Each remaining source is processed to examine smear correction influence similarly, but with different center row orientation based on source location. The measured K for such detectors and each source with and

without desmearing is shown in **Figure 3.6a**, along with the calculated K. It can be seen that the desmeared K correlates with the calculation. The region of usable speckle contrast without desmearing is obviously limited with S2 most noticeably impacted. This is due to our system configuration in which frame transfer occurs in the direction from S4 to S2.

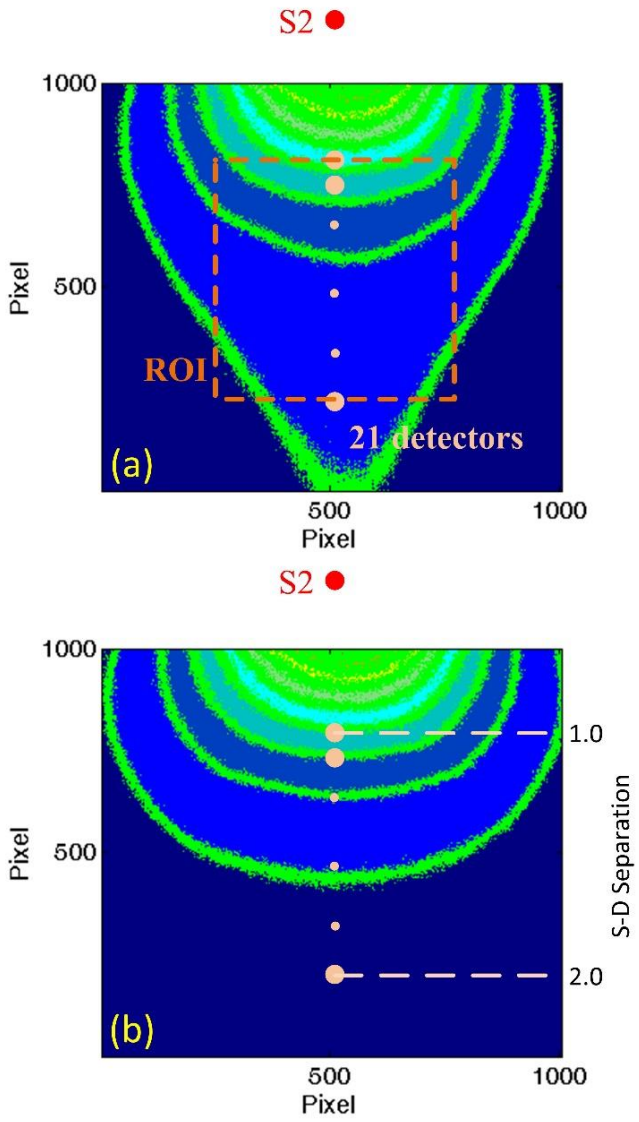

Figure 3.5: Effect of smear correction on image intensity. (a) Original intensity pattern for source S2 on the homogeneous phantom. (b) Desmeared intensity distribution of (a) with a corresponding SD separation axis. These images depict contours of the intensity profiles with dots representing 21 effective detectors for demonstrating the K distribution with the SD separations. Note that the dots are not to scale and the smaller dots serve as an ellipsis for the intermediate detectors.

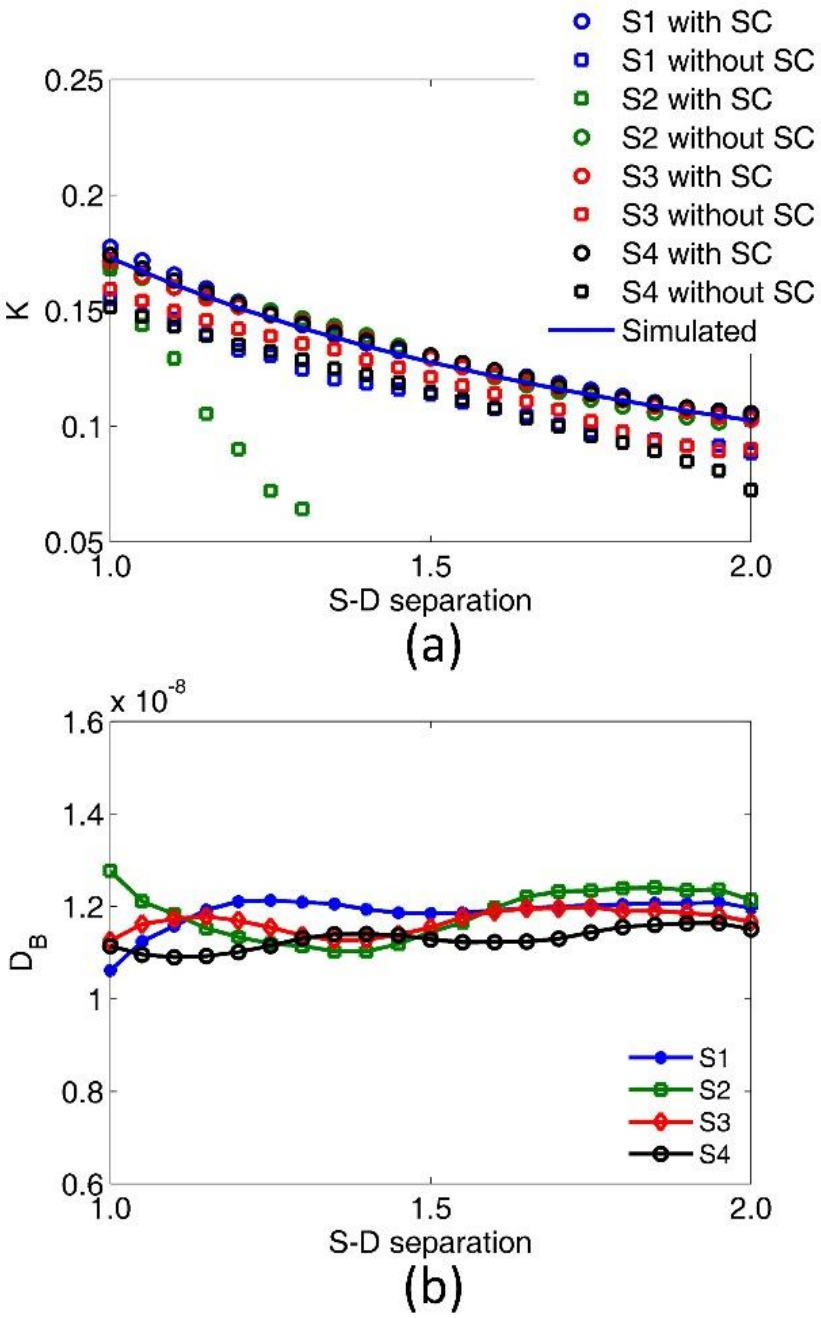

Figure 3.6: Speckle contrast K and D_B influences from smear. (a) K for all sources from detectors defined along the center row with and without smear correction (SC) and numerically simulated K at the SD separations. (b) D_B for center row detectors.

After smear correction we can compare the flow indices measured by the new EMCCD speckle contrast method and standard DCS. Continuing from the previous analysis, the D_B value across the center row of detectors is shown in **Figure 3.6b**. The D_B values achieved from DCS at 2.0 cm SD separation and those independently averaged for S1 to S4 at the 21 detectors are shown in **Table 3.2**. The CCD measured D_B are in good agreement (within 12%) with the standard DCS measurement. The comparison of K distributions measured from S1 on the homogeneous and heterogeneous phantoms is shown in **Figure 3.7**.

Table 3.2: Average D_B from EMCCD and DCS

Source	Average D_B $(\times 10^{-8}\ cm^2/s)$
EMCCD – S1	1.19 ± 0.05
EMCCD – S2	1.18 ± 0.08
EMCCD – S3	1.17 ± 0.06
EMCCD – S4	1.13 ± 0.06
DCS @ 2.0 cm SD	1.28

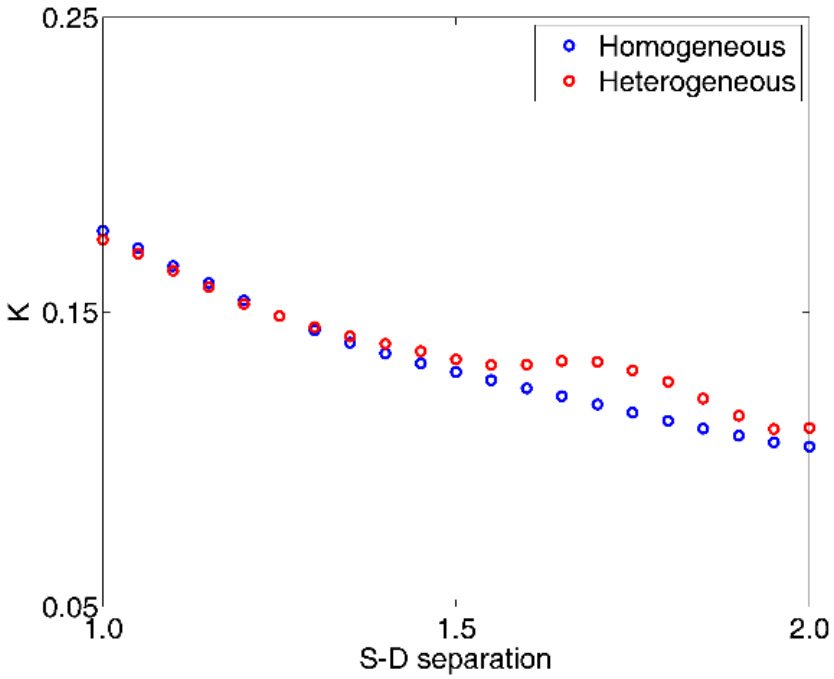

Figure 3.7: Measured speckle contrast distributions on homogeneous and heterogeneous phantoms.

3.7 Flow Heterogeneity Detection and Characterization

To examine the performance of scDCT in detecting and characterizing flow contrast, we next measure the liquid phantom with the submerged solid cube heterogeneity (**Figure 3.2b**). Boundary BFI's were acquired from measured speckle contrast, using **Equations 3.1** and **3.9**, and combined with those obtained from the homogeneous phantom for relative changes. The boundary flow information and valid SD pairs were integrated with the following mesh for image reconstructions. A finite element mesh [dimension (mm): 60 (H) × 60 (W) × 30 (D)] centered at (0, 0, 15) with an average 3 mm node distance, 4-node tetrahedrons, and optical properties matching the phantoms provided a slab-shaped

representative geometry. The mesh was refined in the region known to contain the heterogeneity to improve detection resolution while not overwhelmingly increasing the number of nodes. Refinement was within a 15 mm radius (e.g., inclusive of 5 elements) centered from (0, 0, 30) to a 1.5 mm node distance (total nodes: 10,307) using ANSYS. The relative blood flow, rBF, is used to denote the ratio of phantom with heterogeneity to homogeneous phantom αD_B's. The reconstructed image from homogeneous phantom and heterogeneous phantom are shown in **Figures 3.8a – 3.8b**. A reconstructed heterogeneity was clearly recognizable from the overlaid cross-sections compared between the two images. **Figure 3.8c** shows cross-sectional views of the heterogeneity extracted by half max contrast threshold criteria. The averaged heterogeneity rBF was 0.38 with center (-0.0, -0.1, 25.0) close to the actual center (0, 0, 24.5). Reconstructed heterogeneity side length was 7.2 mm with dimensions that were accurate compared to the true solid phantom.

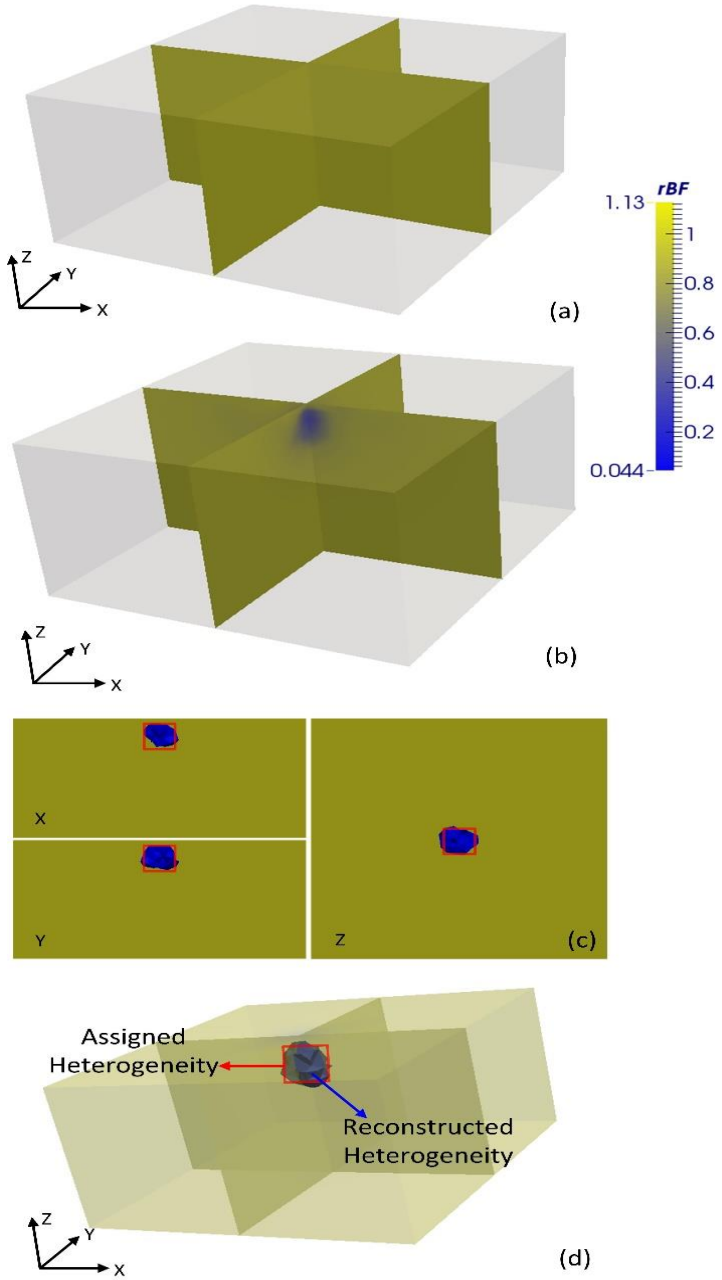

Figure 3.8: Reconstructed 3D flow contrasts. Two-dimensional cross-sectional view (x and y through side centers; z at 24.5) of slab phantom (a) without heterogeneity and (b) with heterogeneity. (c) The region with heterogeneity as extracted by half max contrast threshold criteria. The true region with heterogeneity is depicted by centered squares. (d) The extracted (half max contrast threshold) region with heterogeneity obtained by computer simulation.

For comparison with the ideal scenario, we simulated the phantom experiment by computer using identical parameters. The region with heterogeneity extracted by half max contrast threshold is shown in **Figure 3.8d**. The reconstructed heterogeneity averaged rBF was 0.37 with center (-0.1, 0.0, 24.0), similar to phantom results (averaged rBF within 3% of phantom test results). Corresponding 3D flow distributions were also similar to the phantom experiment (**Figure 3.8b**) and hence not shown. In order to examine the effect of centering the heterogeneity symmetrically in the FOV, we also performed two simulations with it placed in off-center locations, but in an otherwise matching setup. The reconstructed center and side length were both in agreement with expectations.

3.8 Observations and Limitations

In this study, an exposure time of 2 ms was selected to achieve a good contrast to noise ratio [131]. Inherent in this selection was an adverse smear effect. This was resolved by post data collection analysis, but other solutions exist such as shutters or laser gating. The reconstruction and boundary data parameters of delay time τ and window size used herein have been discussed elsewhere [88, 132]. We acknowledge that static scatterer contributions can degrade the current model. Ideally, recovered rBF would be zero. However, we only sought to validate 3D flow contrast detection using our new scDCT method rather than optimize flow recovery accuracy, and we produced sufficient contrast to identify and characterize the anomalous presence. The agreement between scDCT and DCS on a homogeneous phantom and between simulation and phantom in heterogeneity

detection supports success. Furthermore, multiple two-dimensional SD pairs provided by the CCD omits the probe scanning in ncDCT, and thus significantly improves the spatial and temporal resolution. In addition, due to decreasing signal with increased SD separation using a point source we were limited to at most 2.2 cm after noise correction. Nevertheless, this SD separation is still capable of probing tissues ~1 cm depth.

We also note that although the FEM framework allows incorporating complex heterogeneities and boundaries we chose to exemplify our technique in a straightforward setup. Further difficulties may be encountered when extending scDCT to real complex media. For example, surface curvature may result in modified light distributions and SD separations potentially reducing the accuracy and reliability of reconstructed flow contrasts as was described in **Chapter 2.6**. These issues can be addressed in the future through computer simulations, possible free-space corrections [80], and telecentric zoom lens incorporation [133, 134]. To improve results we additionally refined the mesh in the center region around the known cubical heterogeneity location.

Compared to our previous ncDCT design, this system demonstrated potential for fast and dense boundary data acquisition and deep tissue hemodynamics tomography translating directly to human studies (e.g., burn/ulcerous tissue flow detection). However, as the scDCT was designed primarily to further the CCD-based detection and novel speckle contrast flow detection some features are limited. The contact-based source fibers are undesirable in practice due to compression-induced hemodynamic and optical property changes [77, 78],

potential situations of wound sensitivity and exposure, being restricted to outside the camera FOV, and the difficulties in greatly increasing their quantity. This system is also not capable of imaging fluorescence distributions. A fully noncontact scDCT (nc_scDCT) has been developed and combined with DFT capabilities in the next chapter concerning the final instrumentation which performs both flow and fluorescence imaging.

CHAPTER 4 NONCONTACT SPECKLE CONTRAST DIFFUSE CORRELATION AND DIFFUSE FLUORESCENCE TOMOGRAPHY

4.1 Introduction

In this chapter advancements have been made to purpose a prototype diffuse optical instrument in which all the beneficial operational characteristics including noninvasiveness, reflectance mode, noncontact, translational, and sensitivity to both flow and fluorescence changes are borne conjointly. The extension builds upon the designs and techniques of ncDCT and scDCT and its noncontact version (nc_scDCT) as described first. The role of ICG as our fluorescent agent of choice and the related implications is supplied. The chapter is rounded out by the custom designed experimental setup and protocol for executing a combined flow and fluorescence contrast validation. A separate publication illustrated the independent nc_scDCT instrumentation and its testing *in vivo* [100].

4.2 Multimodal Noncontact Speckle Contrast Diffuse Correlation and Diffuse Fluorescence Tomography Prototype

A scanning galvo-mirror (GVS002, Thorlabs, NJ) was added for directing laser source light around the FOV in noncontact fashion (**Figure 4.1**). As this and the following supporting elements remove the static optical fiber source positioning present with scDCT, the method is termed noncontact scDCT (nc_scDCT) [100]. To situate the galvo-mirror at a versatile vantage point, a metal support abreast of

the CCD camera and out of the FOV was machined and installed. Detection of potential source light reflections from the sample surface which have not travelled through the tissue are minimized by installation of cross polarizers. The first polarizer (LPNIRE050-B, Thorlabs, NJ) is interposed between a lens doublet at the source fiber connector and the galvo-mirror. The second polarizer (LPNIRE200-B, Thorlabs, NJ) is placed in a stackable tube (SM2L05, Thorlabs, NJ) in the path of detected light at the zoom lens entrance.

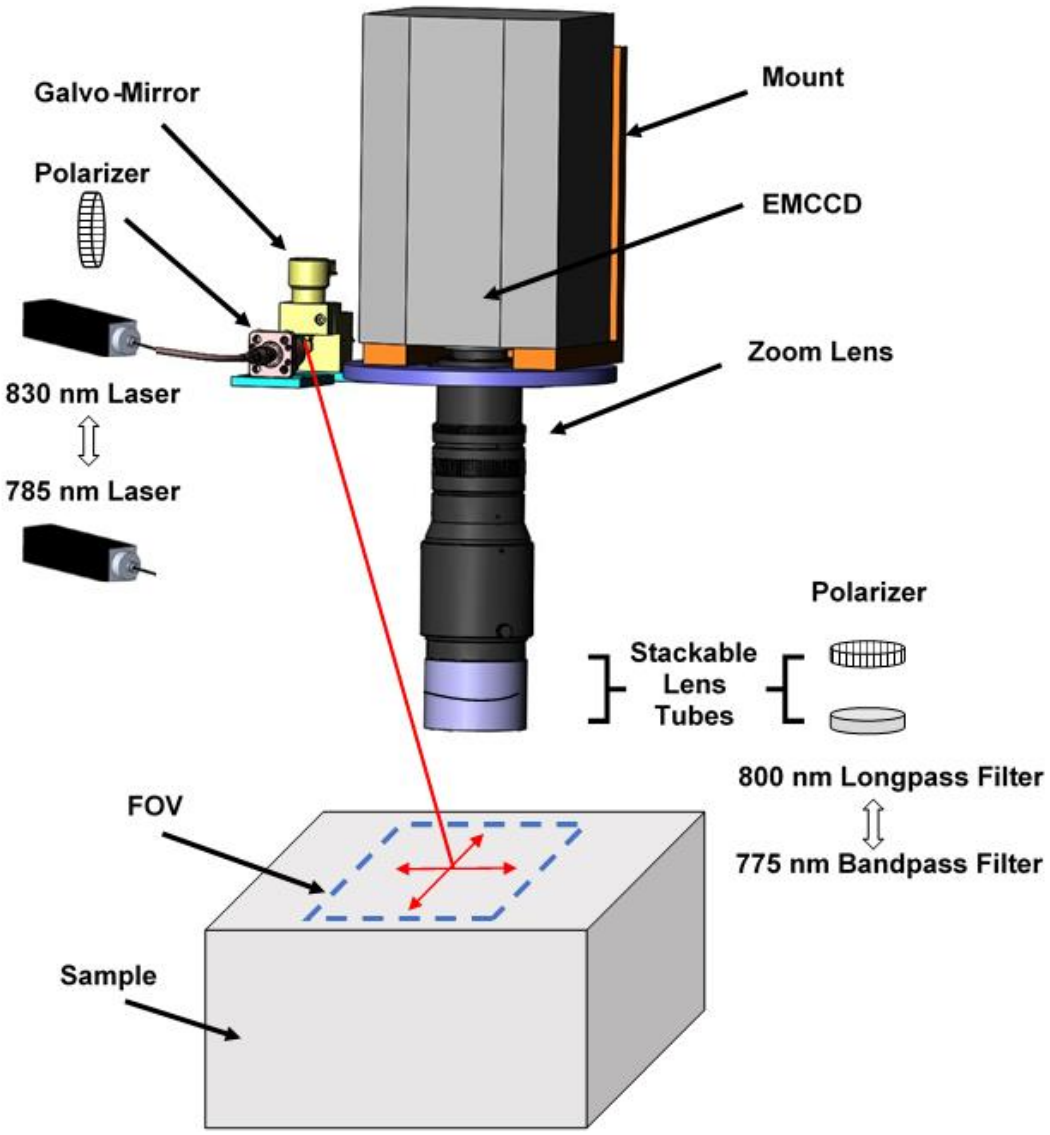

Figure 4.1: Combined nc_scDCT and DFT instrumentation. A laser source fiber directs light into a lens and polarizer before being redirected to the sample surface by the galvo-mirror. Light having travelled through the tissue and reflected from the surface passes through two stackable tubes before interacting with the zoom lens and CCD. The initial tube contains either a 775nm bandpass filter (775BP) or 800nm longpass filter (800LP). The proceeding tube contains a polarizer in cross orientation with the source polarizer to remove reflected light.

In order to isolate the different signals of interest one of two stackable tubes is placed in front of the polarizer at the zoom lens at any given time. For acquiring $BFI(785nm)$ or $\mu_a(785nm)$ a 775 nm bandpass filter (775BP; 86-968, EdmundOptics, NJ) is placed in one stackable tube. For acquiring $BFI(830nm)$, $\mu_a(830nm)$, or $\eta\mu_{a,fl}$ an 800 nm longpass filter (800LP; 84-762, EdmundOptics, NJ) is placed in another stackable tube. These stackable tubes are manually exchanged as necessary during experimentation along with the appropriate laser source. The polarizers remain in place throughout operation.

4.3 Indocyanine Green and Source Light

Indocyanine green (ICG) is a frequently used and documented fluorescent dye in the NIR spectrum [16, 17, 19, 30, 33, 35, 135]. It is also FDA approved and relatively inexpensive. The excitation and emission spectrum of ICG in whole blood are shown in **Figure 4.2**. In our liquid phantoms we incorporate water, Intralipid (primarily water), and ink (primarily water) which comprising a primarily aqueous solution can diminish the fluorescent properties after ~6 hours. The experimental protocol in this study therefore confines the total experiment duration (once ICG is prepared in aqueous solutions) to within this interval. Furthermore, our preliminary testing in similar phantom arrangements to those used herein suggested that the 785 nm laser (as used with scDCT; **Chapter 3**) produced adverse flow results at high ICG concentrations. An 830 nm laser (as used with ncDCT; **Chapter 2**) was

therefore also incorporated for comparison due to its increased distance from the ICG absorption peak (**Figure 4.2**).

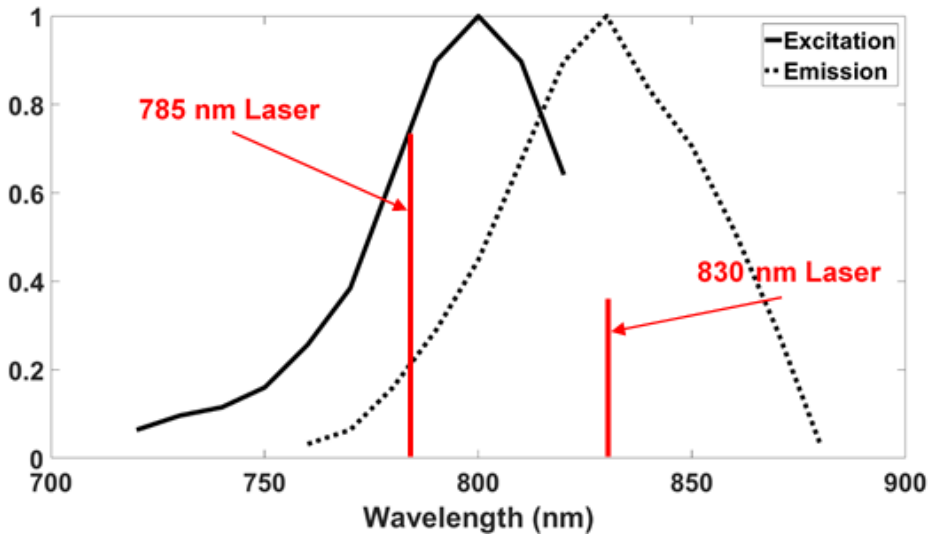

Figure 4.2: ICG and laser sources. The normalized excitation and emission curves of ICG are shown with the wavelengths of the two laser sources (785 and 830 nm) used. It is expected that the 830 nm laser BFI recovery will exhibit a diminished influence from the presence of ICG due to its location lower in the absorption/excitation spectrum.

4.4 Experimental Setup

The noncontact source/detection apparatus is located directly above a container filled with liquid phantom background, $\mu_a(785nm) = 0.05\, cm^{-1}$, $\mu_s'(785nm) = 7.0\, cm^{-1}$, $D_B \approx 1 \times 10^{-8}\, cm^2/s$, and centrally stationed custom hinged structure for holding and swapping contrast elements (**Figure 4.3**). The

flow contrast was provided by a 6 mm side length solid cubical phantom, $\mu_a(785nm) = 0.05\ cm^{-1}$, $\mu_s'(785nm) = 7.0\ cm^{-1}$, αD_B approximately three orders of magnitude lower than background as measured previously [125], submerged at 2 mm depth on one side of the 60 mm × 60 mm FOV. Fluorescence, and inherently absorption, contrasts were created by tubes (5.9 mm outer diameter, 5.3 mm inner diameter; PRT00074, ClearTec Packaging, MO) filled with liquid phantom background and a varying concentration of ICG. They were submerged (one per each step) at 2 mm depth with concentrations in steps from 0.0625 – 4 μM in doubling fashion for a total of 8 steps (plus one step of 0 μM) on the opposite side of the FOV. This concentration range agrees with typical diffuse optical applications in the literature and includes the maximum ICG fluorescence signal (~1 μM) before it proceeds to decrease with further concentration increases. With reference to the coordinate system centered in the FOV (0, 0, 0) as the x-y plane on the surface at depth z = 0 mm, the solid cube center was (-9.74, 0, 5.0) and tube center (12.3, …, 5.0; extending effectively indefinitely outside the FOV in the y direction).

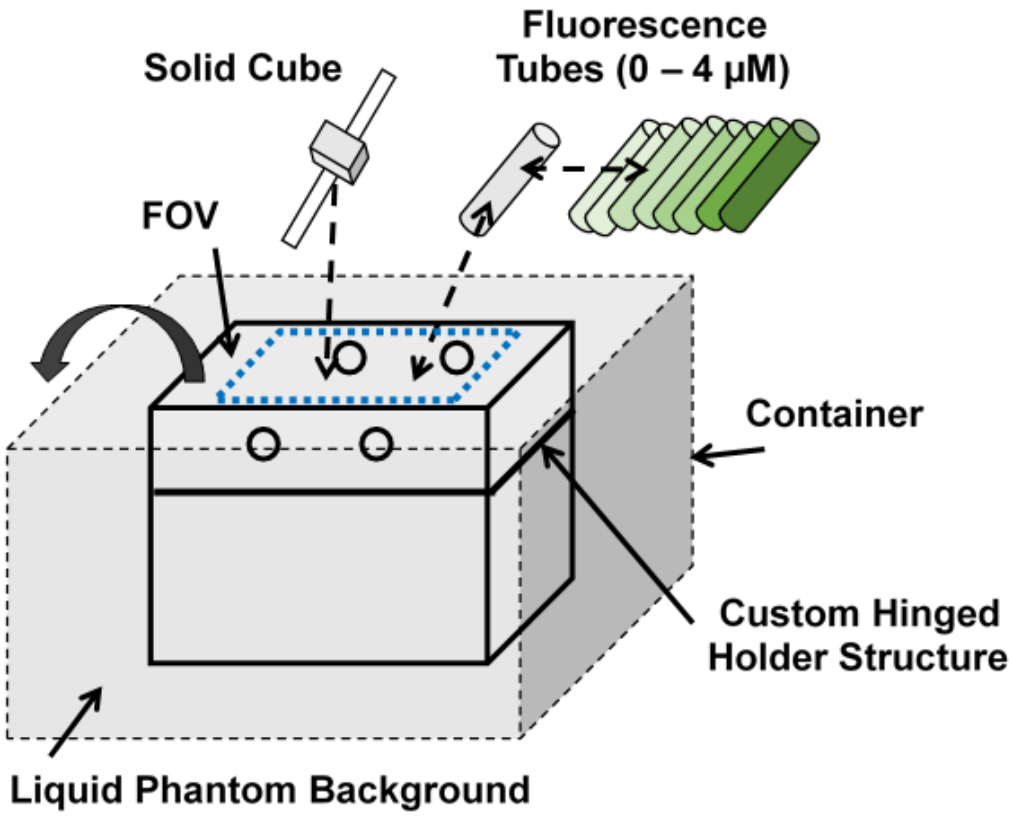

Figure 4.3: Experimental setup for multimodal system testing. A liquid phantom background pervades a container centered around the camera FOV (blue dashed line). A custom holder also centered enables fast switching of flow (cubical solid phantom) and fluorescence/absorption (liquid-containing tubes) contrasts in the left and right regions, respectively.

4.5 Data Acquisition Procedure

Prior to data collection several preliminary tasks were performed. The container was placed in the camera FOV with the hinged structure centered. The liquid phantom background was then created with Intralipid, India ink, and distilled water as done in our earlier studies (see **Chapter 3**). This was used to fill the

container to a level 2 mm above the designated areas for cube and tube insertion. A single tube of 115 mm length was filled with the liquid phantom background solution and placed as designated in the hinged structure along with the solid phantom cube. The displacement of the surface level due to the added heterogeneities was negligible. Some liquid was removed temporarily to acquire a reference image of the heterogeneity layout as shown in **Figure 4.4**.

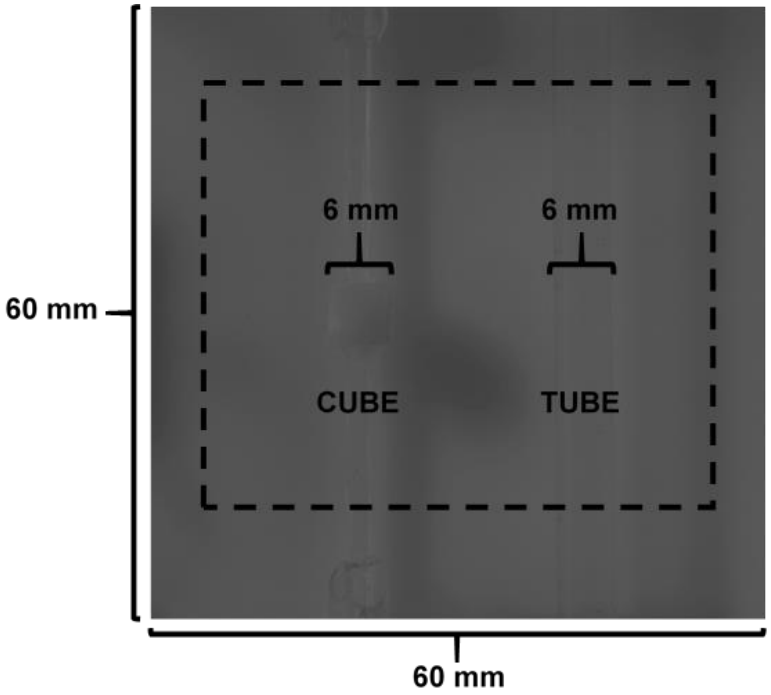

Figure 4.4: Heterogeneity layout. A reference image of the positioning of flow (cube) and fluorescence (tube) contrasts prior to data collection. Data outside the dashed frame is within the FOV, but excluded from analysis. The surface level of the liquid phantom background was reduced only for this image.

After restoring the surface level and removing heterogeneities, the 785 nm laser source was applied. The galvo-mirror scan offsets to achieve a 9 × 9 grid of source positions were determined covering the 60 mm × 60 mm FOV. A set of images were acquired for post-analysis calculation of the source positions. This was repeated for the 830 nm laser along with verifying the scan settings and coverage area (**Figure 4.5**).

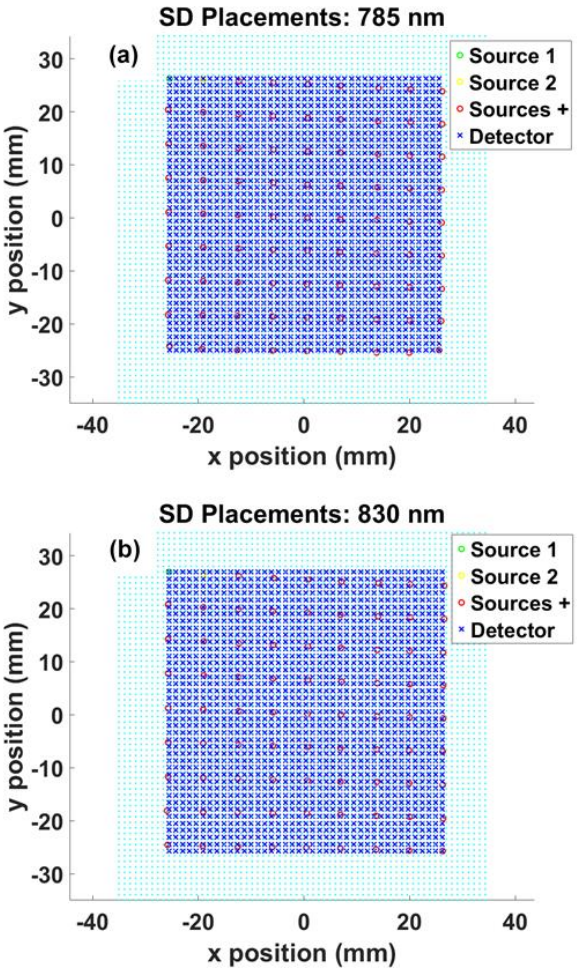

Figure 4.5: Source-Detector layout for 785 and 830 nm. The 9 × 9 source (circles) and 41 × 41 detection (crosses) grids for (a) 785 nm and (b) 830 nm lasers.

Eight 115 mm length tubes were then filled with ICG in the following fashion. A base dye solution of 15.48 µM was created with 1.2 mg of ICG (MW: 775 g/mol) and 100 ml of the surplus liquid phantom background. The remaining surplus liquid phantom background, in a separate container, was brought up to the first step of 0.0625 µM ICG concentration using the base dye solution. An aliquot was then taken to fill a single tube. The base dye solution was added again to the primary solution for 0.125 µM and an aliquot placed in the second tube. This was repeated to fill the remaining six tubes, up to 4 µM.

The final preliminary objective was in establishing the exposure times for fluorescence and absorption measurements. The maximum concentration tube was placed in the structure along with the solid phantom cube. Exposure times were varied until the highest intensities were ~90% max (of 16-bit digitization; ~59,000 counts). This increased the available signal while remaining below the level of pixel saturation. To accomplish this a program was written in MATLAB to mask and plot the intensity data in an SD range-delimited annulus for visualization. The flow exposure time was restricted in that it has an inherent relation with the flow dynamics – the value was selected based on our nc_scDCT study [100].

Each step consisted of five unique system setups as shown in **Table 4.1**. This row arrangement is maintained in actual data collection sequencing (**Figure 4.6**) to minimize transition time (e.g., switching filter and/or laser). An initial step not otherwise depicted consisted of the flow baseline step which included the 0 µM tube only (i.e., no cube present). Subsequent data collection then consisted of

acquiring data for each variation in tube concentration while the cube remained unhindered.

Table 4.1: System collection parameters at a single step

Target	Exposure Time (ms)	# Frames	Frame Rate (fps)	Filter	Laser Source (nm)
$\eta\mu_{a,fl}$	750	4	1.4	800LP	785
$\mu_a(785\ nm)$	15	10	8	775BP	785
$BFI(785\ nm)$	5	10	8	775BP	785
$BFI(830\ nm)$	5	10	8	800LP	830
$\mu_a(830\ nm)$	25	10	8	800LP	830

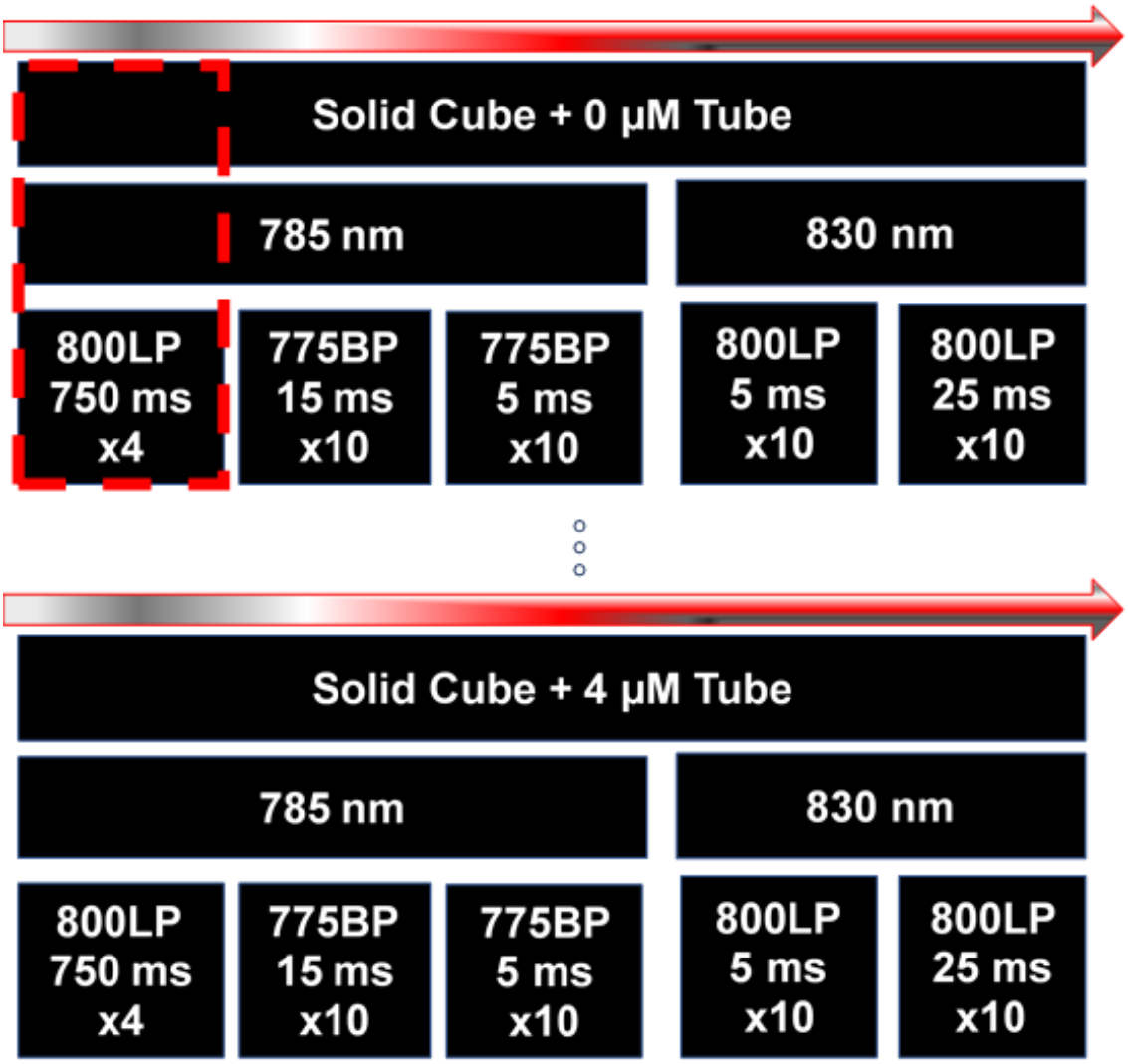

Figure 4.6: Data acquisition sequencing. The data collection is depicted at the top with a single complete step consisting of the simultaneous presence of the solid cube and a tube with 0 µM ICG. This is repeated for each step of increasing fluorescence up to the final step (solid cube plus 4 µM tube). The attached filters are identified as well as the corresponding source wavelengths, exposure times, and number of frames collected.

The data acquisition for an individual signal was automated through the complete set of 81 source positions using a customized LabVIEW program once the appropriate laser source and filters were attached. The automation was (for each position): set galvo-mirror offset values, signal galvo-mirror to move, wait 100 ms, trigger camera, wait for exposure completion, wait for frame readout completion. The camera control program (open source μManager, Open Imaging) was set to acquire the appropriate number of images.

To process the data, a 41 × 41 grid of logical detectors was identified to span the source grid area of the corresponding source (see **Figure 4.5**). Detectors were separated by 1.25 mm. Each source position was found by averaging the row and column indices for intensities greater than half max from the reference images collected at the beginning of the protocol. This is on the assumption that the intensity is roughly symmetric and falls away from the center in a radial (and exponential) manner. Ultimately, we end up with 136,161 possible SD arrangements. The actual data used in reconstructions was restricted by SD separation to limit noise while probing up to the requisite depth sensitivity of the contrast elements. With a sensitivity of ~1/2 SD separation, heterogeneity depth up to 8 mm, and increasing noise/decreasing signal at large SD, the SD range was limited to 16 mm. The lower end criteria excluded data close to the source (< 7 mm) where the data tends to deviate from expectations as experienced in previous investigations. This SD range was kept consistent for all boundary data processing and reconstructions (e.g., flow, fluorescence, and absorption).

The post-analysis processing of data is shown in **Figure 4.7**. The processing overlaps in several ways such as dark correction, low-pass (Gaussian) filtering, and averaging data across frames. The flow and absorption data were smear corrected due to the order of the exposure time being near that of the frame transfer time (see **Chapter 3**). For all sets of information, the basic data was considered as that calculated in a 7 × 7 window. This was averaged over a 21 × 21 block in the neighborhood of each effective detector. The resulting values were then averaged across the collected frames. A detector position was established as the center of its corresponding block. For flow, the reconstruction process requires an estimated αD_B at each SD pair which is determined by the semi-infinite based speckle contrast minimization (see **Chapter 3**). Calibration for flow was performed by applying calibration factors to boundary data as obtained from the baseline step where flow is homogeneous throughout ($\alpha D_B \cong 1 \times 10^{-8}$ cm^2/s). The fluence boundary data for absorption was calibrated to the forward solution in NIRFAST of the homogeneous baseline step with known absorption coefficients. The fluorescent fluence boundary data was subtracted from the baseline step (i.e., no fluorescence) to remove the excitation signal.

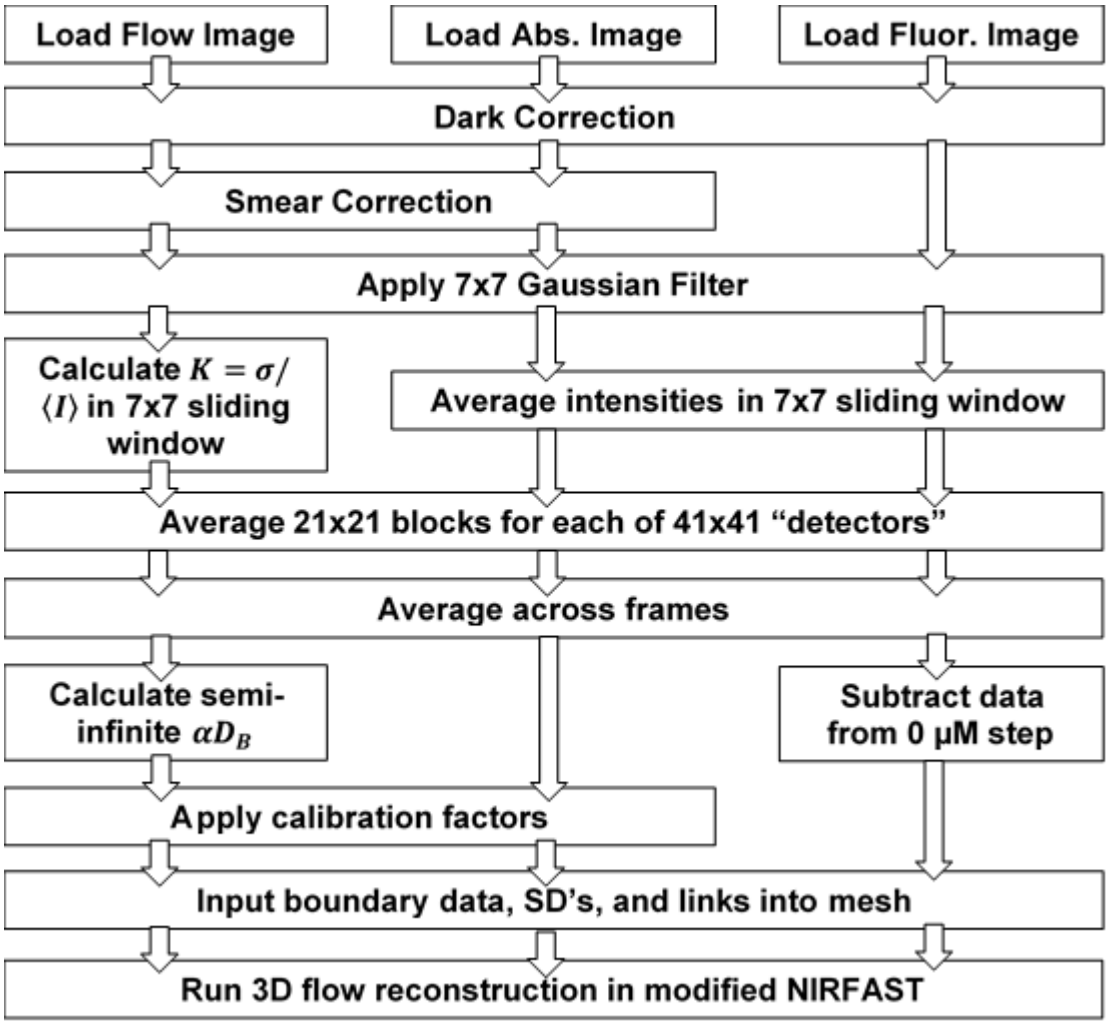

Figure 4.7: Flow diagram of data processing. The diagram charts the path of data along various levels of processing for flow, fluorescence, and absorption.

Absorption reconstructions are analogous to those of flow as outlined in **Chapter 2.4**. The substitution of G_1 by Φ and setting $\tau = 0$ provides the formally equivalent set of steps. These features are already provided within the FEM framework in NIRFAST [105, 110]. FEM fluorescence reconstructions also resemble those of absorption/PDE as can be seen by the similarity of the CW PDE (**Equation 1.1**) and coupled fluorescent diffusion equations (**Equations 1.2** and

1.3). The formal definitions include comparable Robin boundary conditions, FEM discretization, and matrix equations where the source vector for the emission wavelength is expressed in terms of the (CW) excitation fluence $S_{fl,i} = \int_{\Omega} \psi_i \Phi_{ex} d\Omega$, and the updating procedure includes both the excitation absorption $\delta\mu_{a,ex}$ and the fluorescence yield $\delta\eta\mu_{a,fl}$ as described in detail elsewhere [136] and is also already included in NIRFAST.

The flow and absorption reconstructions used a mesh of [dimensions (mm): 70 (H) × 70 (W) × 30 (D)] with 31,091 nodes at 1.05 mm node distance. The fluorescence had a mesh of reduced node numbers due to memory requirements. The corresponding mesh had [dimensions (mm): 70 (H) × 70 (W) × 30 (D)] with 7,094 nodes at 2 mm node distance. In addition to SD range limits, edge regions were masked from SD pairs as shown in the outline in **Figure 4.4**. There were a total of 81 source and 1,681 detector positions used in all reconstructions with 17,912/16,823 valid SD pairs for 785/830 nm sources. The average number of iterations and reconstruction times (minutes) for flow, fluorescence, and absorption are shown in **Table 4.2**. All reconstructions used a [20 20 20] pixel basis for the secondary mesh with 8000 nodes (used in calculating the Jacobian and update per iteration). Flow distributions are reported as nodal $rBF = \alpha D_B / \alpha D_{B,0}$ where $\alpha D_{B,0}$ are the nodal values from the 0 μM tube, absent solid cube step. Fluorescence results are reported as nodal $r\eta\mu_{a,fl} = \eta\mu_{a,fl} / \left(\eta\mu_{a,fl}\right)_0$ where $\left(\eta\mu_{a,fl}\right)_0$ is the baseline step of 0.0625 μM tube with cube present. Absorption results are reported as actual recovered nodal values.

Table 4.2: Reconstruction iterations and times

Reconstruction	# Iterations		Reconstruction Time (minutes)	
	785 nm	**830 nm**	**785 nm**	**830 nm**
Flow	13.7 ± 0.8	13.1 ± 0.3	59.4 ± 2.8	52.9 ± 4.0
Fluorescence	50.6 ± 6.9	-	704 ± 96	-
Absorption	10.0 ± 3.8	11.2 ± 3.7	45.7 ± 17.0	46.1 ± 14.5

4.6 Results

The fluorescence distributions recovered at each step of varying ICG concentration are shown in **Figure 4.8**. The tube shown was separated from background by a threshold of three standard deviations above the mean. The detection and localization capabilities are evident with the tube clearly separated from the background and in the region expected. The characterization of the tube shape is distorted in appearance but has similarity to a tube with the proper orientation. This inadequacy is due in part to the lower density mesh used in fluorescence reconstructions. The characterization of relative fluorescence changes involved normalization of the extracted heterogeneity average fluorescence per step to the middle of the tested range (1 µM) as shown in **Figure 4.9**. These values are compared to the expected values with good agreement. The larger deviations at higher concentrations is likely caused by the self-quenching and diminished signal of ICG at concentrations greater than 1-2 µM resulting in underestimations in comparison with the strict trend used. Additionally,

inaccuracies in the preparation of ICG may result in the absolute concentrations being lower/higher than expected. Extracting small amounts of solid ICG for placement in the aqueous base solution created an uncertainty in the mass with true value in the range of 1.2 ± 0.2 mg. Due to the instability of ICG in water, creating a large base solution for storage and reuse was not feasible.

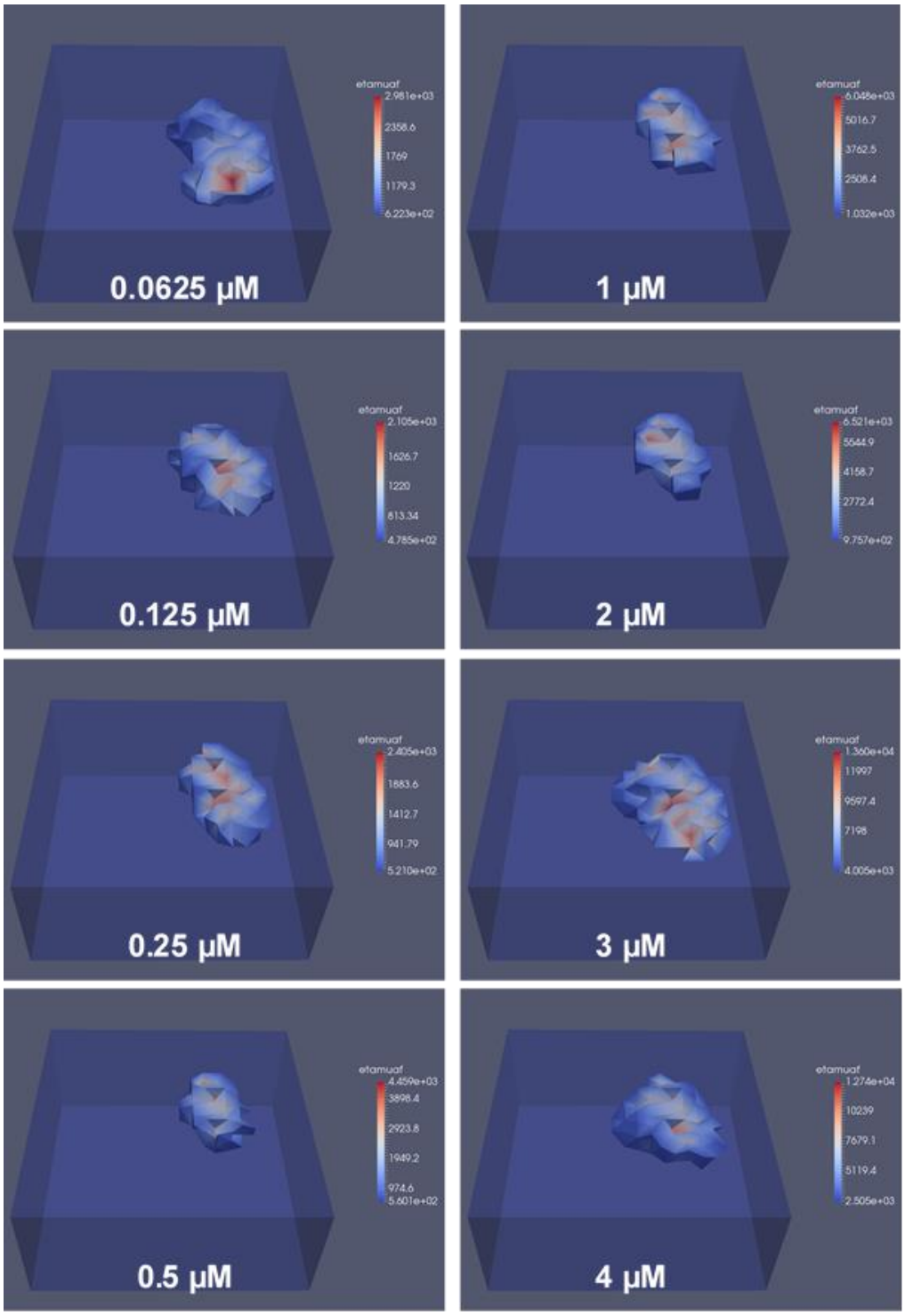

Figure 4.8: Recovered fluorescence images. The heterogeneity as recovered by fluorescence distributions for each step of ICG variation.

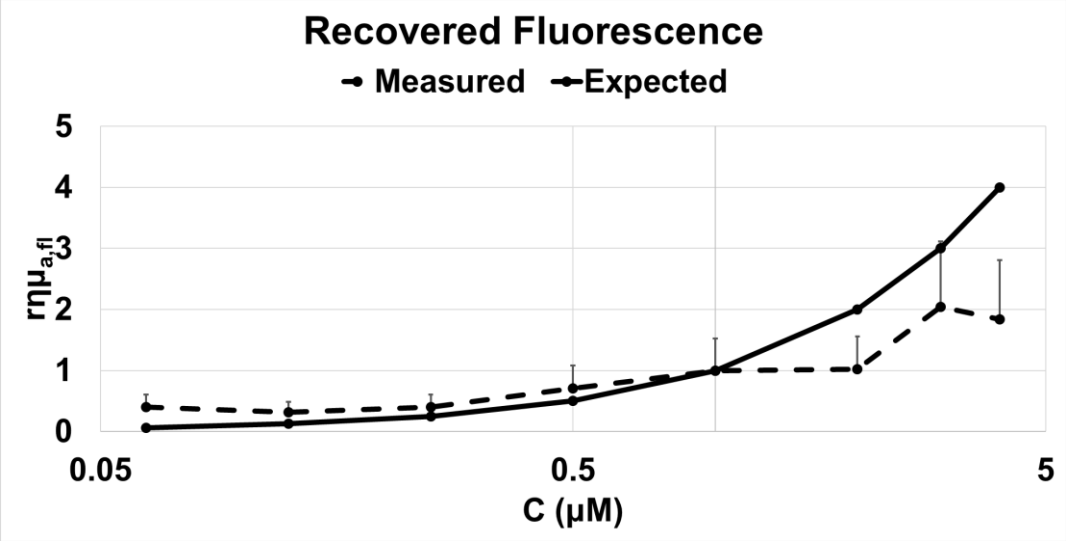

Figure 4.9: Recovered fluorescence changes. The heterogeneity average fluorescence as recovered by fluorescence distributions for each step of ICG variation in comparison with the expected changes (solid line).

The heterogeneity as extracted by absorption coefficient distributions are shown for 785 nm and 830 nm in **Figures 4.10** and **4.11**, respectively. The background and heterogeneity were separated by a threshold of three standard deviations above the mean. The heterogeneity detection and localization with the absorption coefficients were quite evident for 785 nm. Corresponding tube shapes and orientations were also in agreement with the known situation. These characterizations increasingly trended towards the tube properties with increasing concentration. At the lowest concentrations (e.g., < 0.25 μM) the tube was difficult to separate from the background with some noticeable erroneous inclusions. The 830 nm results have artifacts that are obfuscating the recovery of the true tube data. However, at higher concentrations (e.g., > 1 μM) the increasing absorption dominates and the conclusions coincide with that for 785 nm absorption

coefficients. Using the threshold-extracted heterogeneity at each step, nodal absorption coefficients were averaged and their change with ICG concentration is shown in **Figure 4.12**. There is a 320% increase in 785 nm absorption over the steps. The 830 nm absorption trend is inconclusive due to artifacts in the lower ranges.

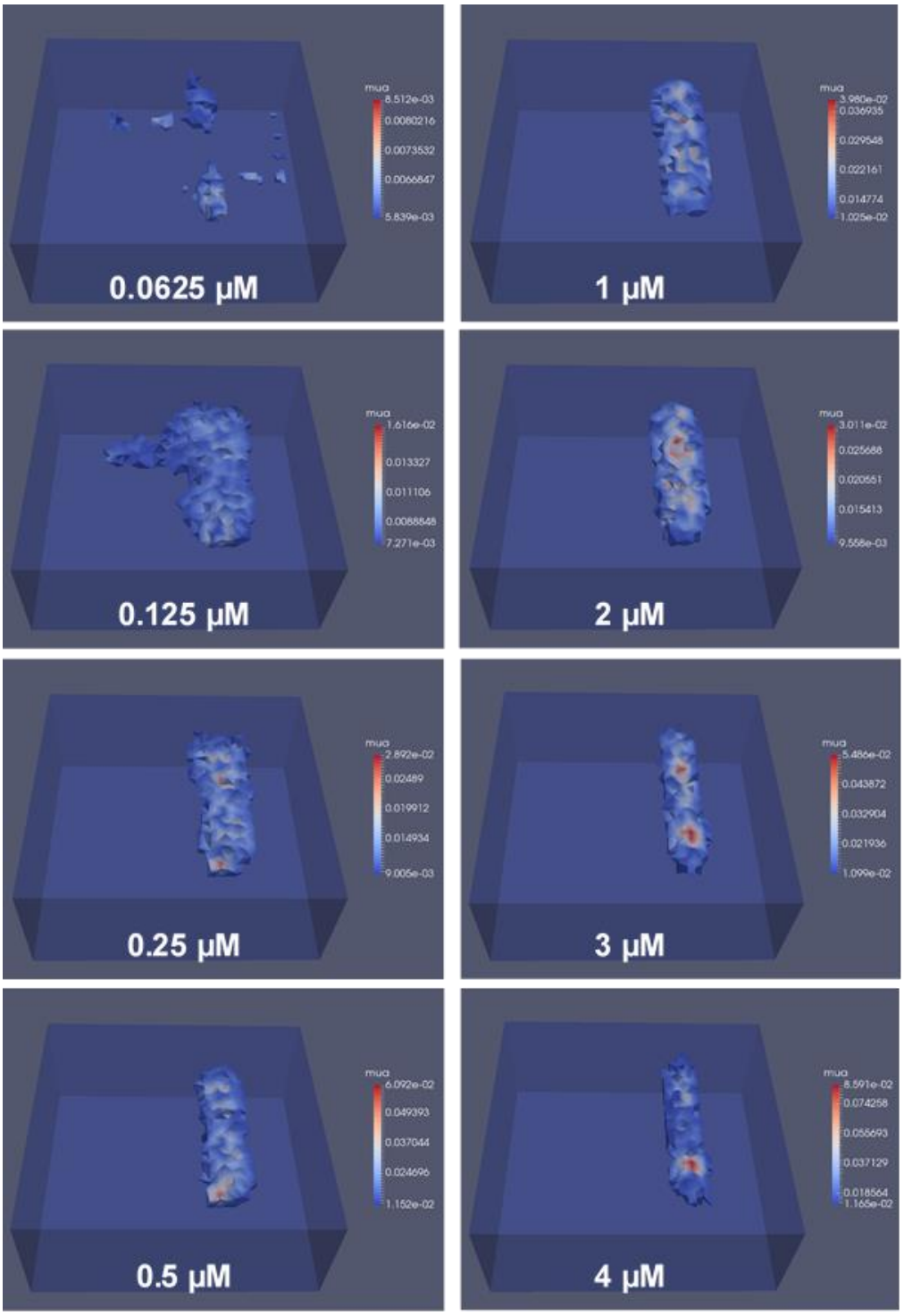

Figure 4.10: Recovered 785 nm absorption. The 785 nm absorption coefficient distributions are shown for each step of ICG variation for the extracted heterogeneity.

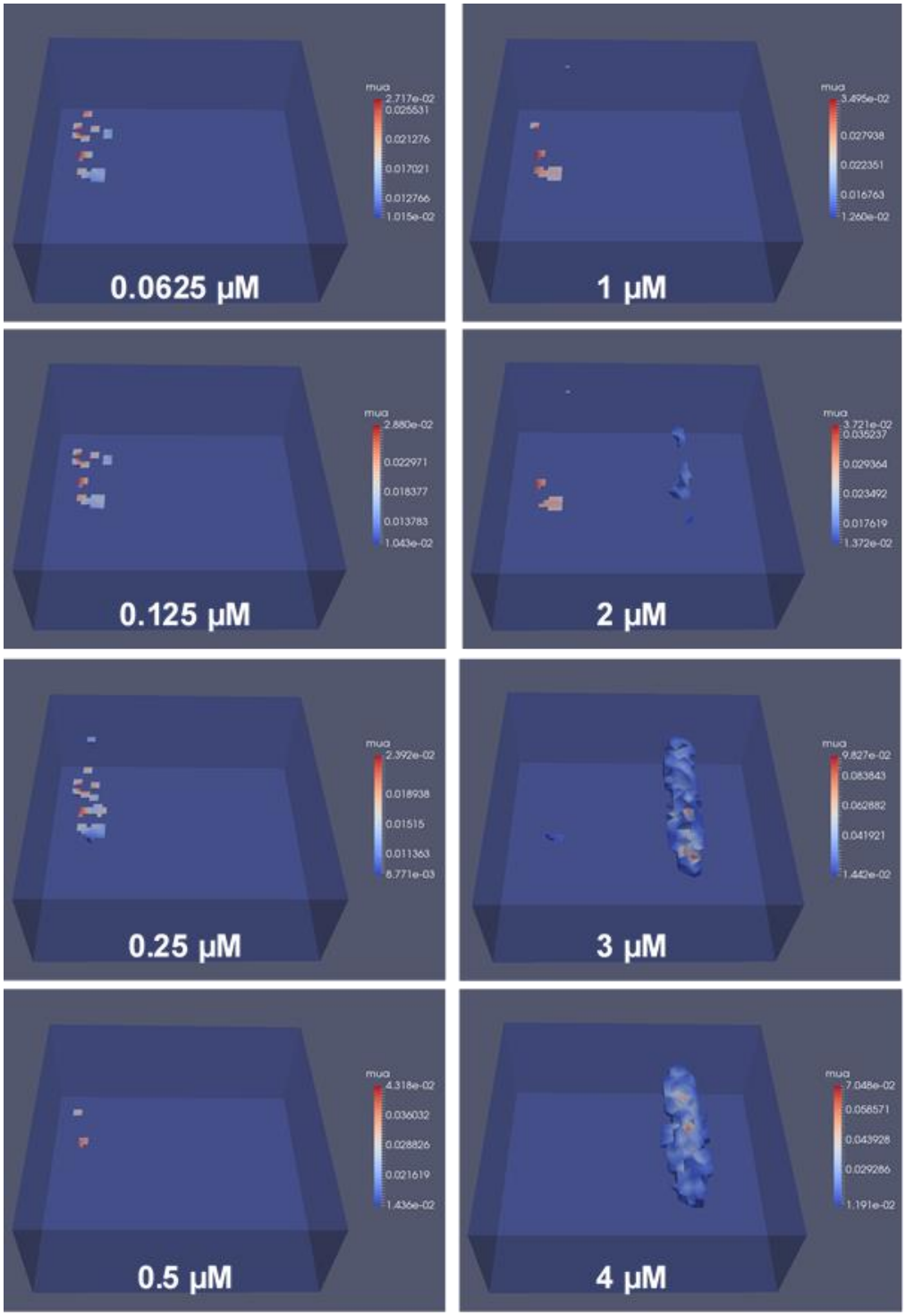

Figure 4.11: Recovered 830 nm absorption. The 830 nm absorption coefficient distributions are shown for each step of ICG variation for the extracted heterogeneity.

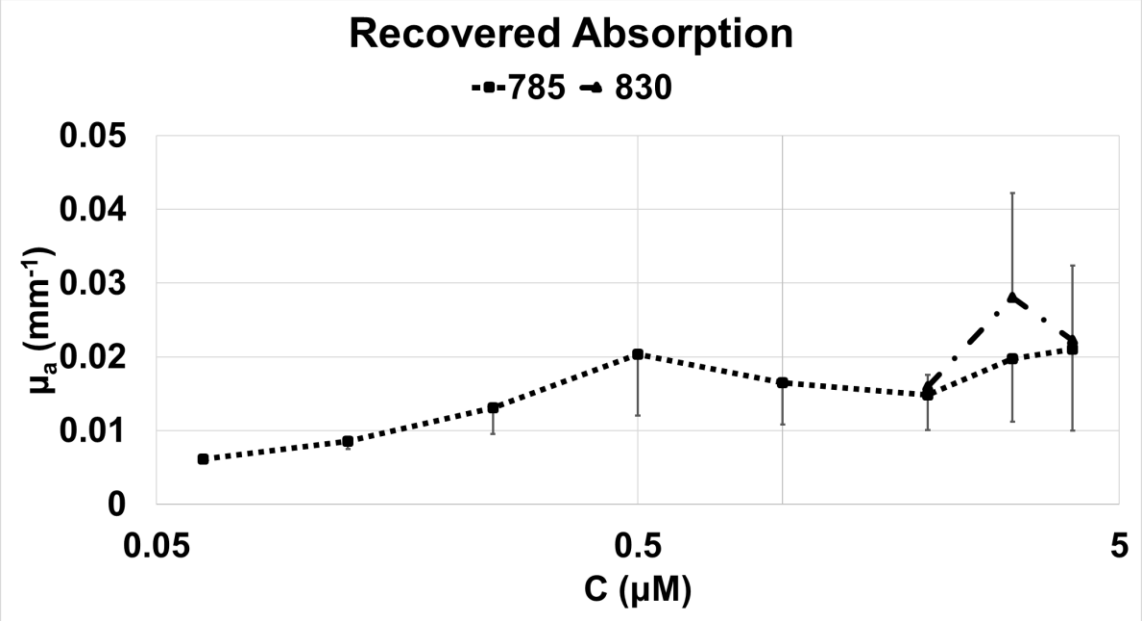

Figure 4.12: Recovered absorption coefficient changes. The nodal average of absorption coefficients as recovered from the threshold-extracted heterogeneity at each step.

Further characterization includes the tube depth and lateral position as shown in **Figure 4.13** for the fluorescence and absorption coefficient extracted heterogeneities at each step. The depth is calculated as the z-coordinate of the center of mass (nodal weighted fluorescence or absorption coefficient). The lateral position similarly is by the x-coordinate of the center of mass. As the tube extends outside the FOV, the y-coordinate is not specified but instead the agreement was visualized in **Figures 4.8**, **4.10**, and **4.11**. The tube depth was most successfully recovered by the fluorescence signal with an average percentage error of 41% whereas 785 nm absorption was 74% error (830 nm data insufficient). The increasing signal with fluorescence did not correct the depth estimate. This is due in part to the sampling density and that ICG (MW 775 g/mol) may have

preferentially accumulated at the bottom of the tube (primarily water: MW ~18 g/mol). The lateral positioning did, however, show a gradual improvement with concentration.

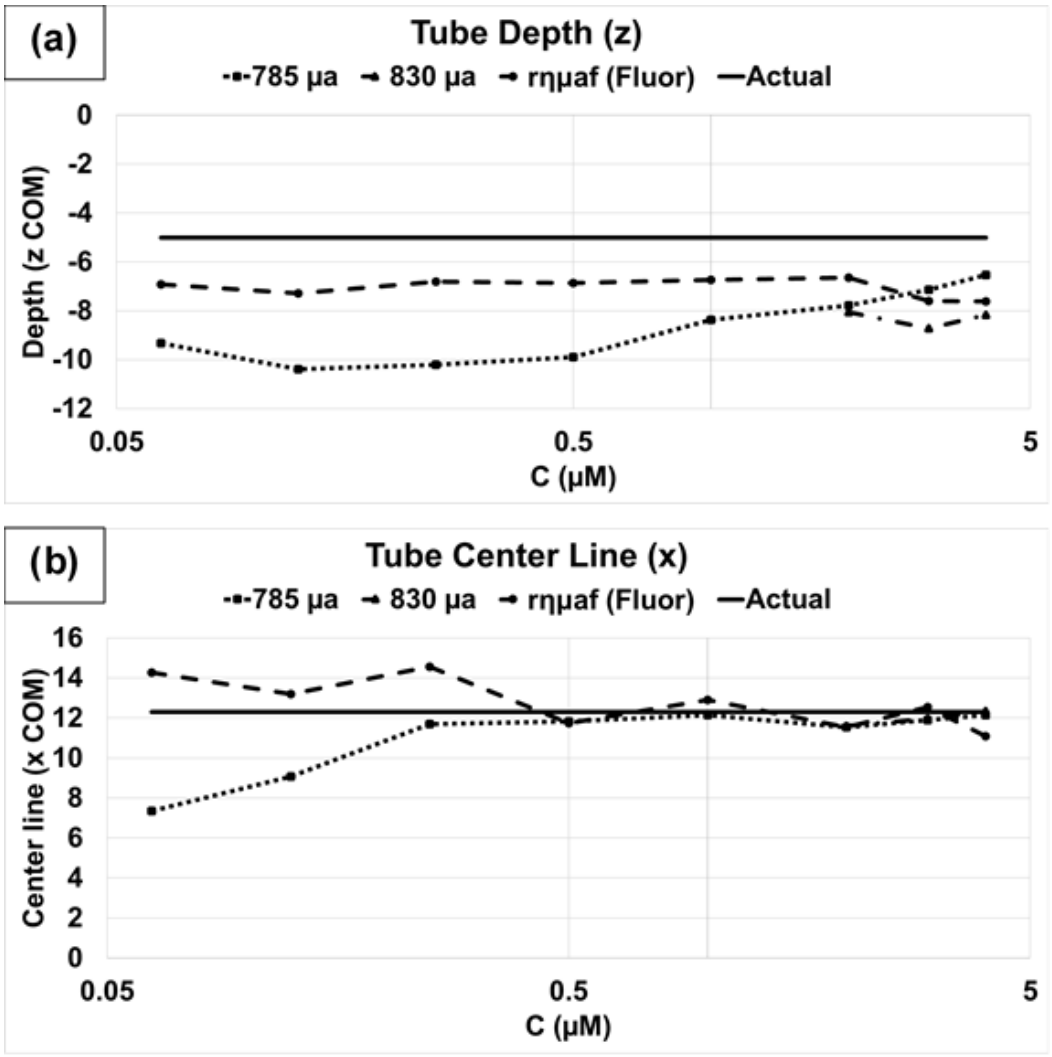

Figure 4.13: Characterized tube properties. The (a) tube depth (center of mass z-coordinate) and (b) lateral position (center of mass x-coordinate) are shown based on the recovered fluorescence and absorption coefficients. The actual value is provided by a solid line for comparison.

In the case of flow, we expect the reconstructed heterogeneity to resemble a cube and present with low flow values with respect to the background. The flow heterogeneity as extracted by half-minimum threshold is shown for 785 nm and 830 nm in **Figures 4.14** and **4.15**, respectively. The cube is detected and localized in the appropriate region by both wavelengths at low concentrations of ICG. A noticeable disturbance in the tube region arises at ~0.25 μM for 785 nm and ~1 μM for 830 nm. The size of the disturbance increases with the graduation of ICG concentration. The derived cube center of mass, averaged rBF, and average side lengths are shown in **Figures 4.16** and **4.17**. This data excludes the region of disturbance and only pertains to the cube properties. The x and y coordinates were near to the true values with offsets of: 1.7 ± 0.46, 1.7 ± 0.38 mm and 0.67 ± 0.24, 0.52 ± 0.22 mm, respectively for 785/830 nm. This coincides with the square appearance of the upper portion of the recovered cube shape. Depth recovery for 785/830 nm was off by 4.0 ± 0.09, 3.8 ± 0.06 mm over all cases as reflected in the z center of mass coordinate and recovered shape. The threshold chosen was based on previous studies as well as the best recovery of the cube as judged across all steps. Modifying the threshold and increasing the sampling density in the cube region can improve characterization. The heterogeneity rBF was consistent throughout all steps with 785 nm (0.41 ± 0.05) higher on average in comparison with 830 nm (0.31 ± 0.07). Both values dropped after the first step suggesting some vestiges of motion lingered from the early setup stages. As all relative flow values depend on the first step, it is expected that the difference between the recovered flow in the first step from both wavelengths persisted

through the remaining steps once the phantom had stabilized. The relative flow values agreed with previous measurements. The last metric characterized was the average side length. While 830 nm exhibited a nearly constant recovered side length (5.0 ± 0.55 mm), 785 nm (3.9 ± 1.2 mm) had strong influences due to the ICG presence (> ~0.25 μM). The inaccuracy in depth and corresponding “depth side length” contribution is likely the cause of both wavelengths’ underestimation of the average side length in all cases.

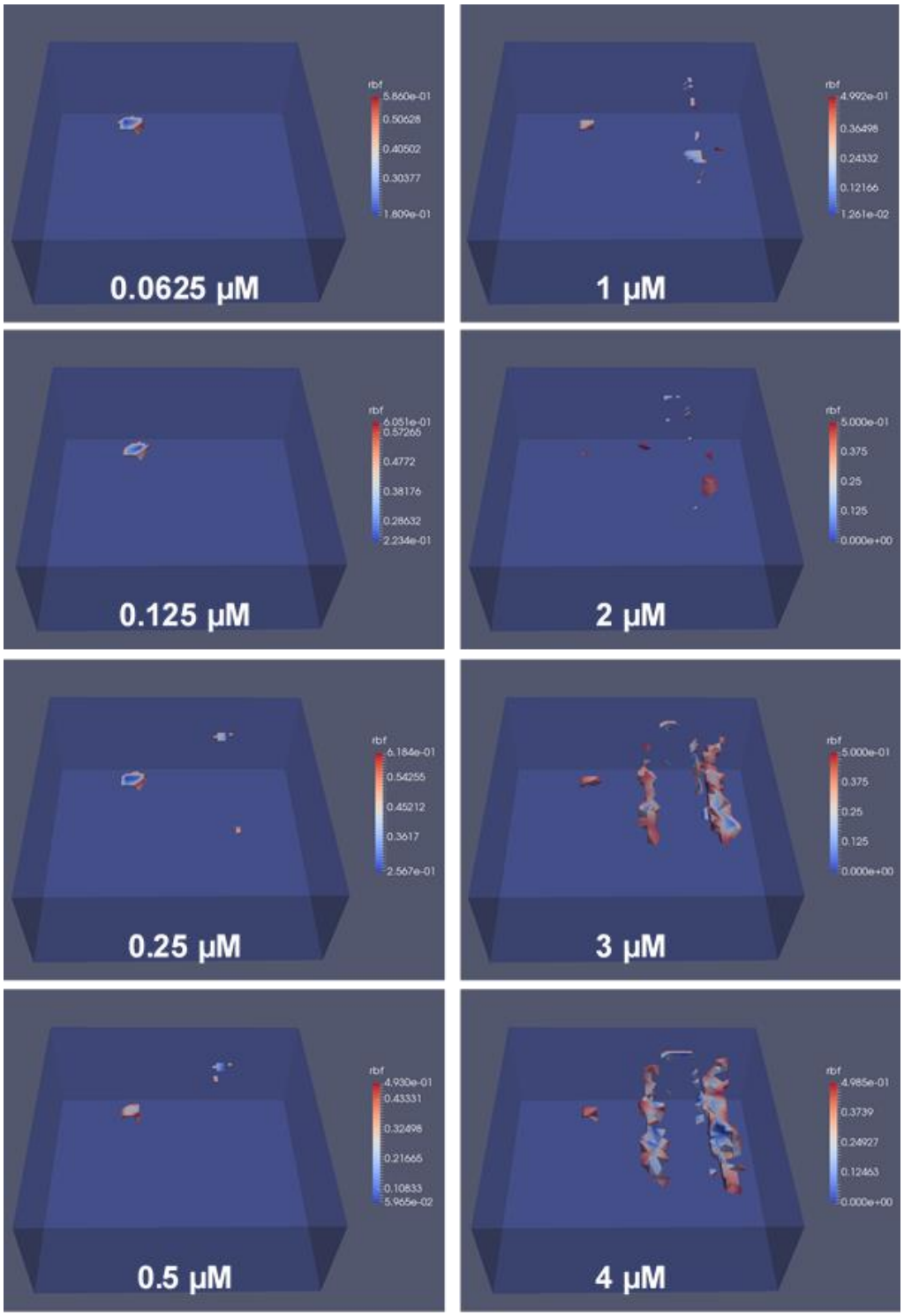

Figure 4.14: Recovered 785 nm flow. The heterogeneity as recovered by flow distributions with a half-min threshold for extraction over all steps.

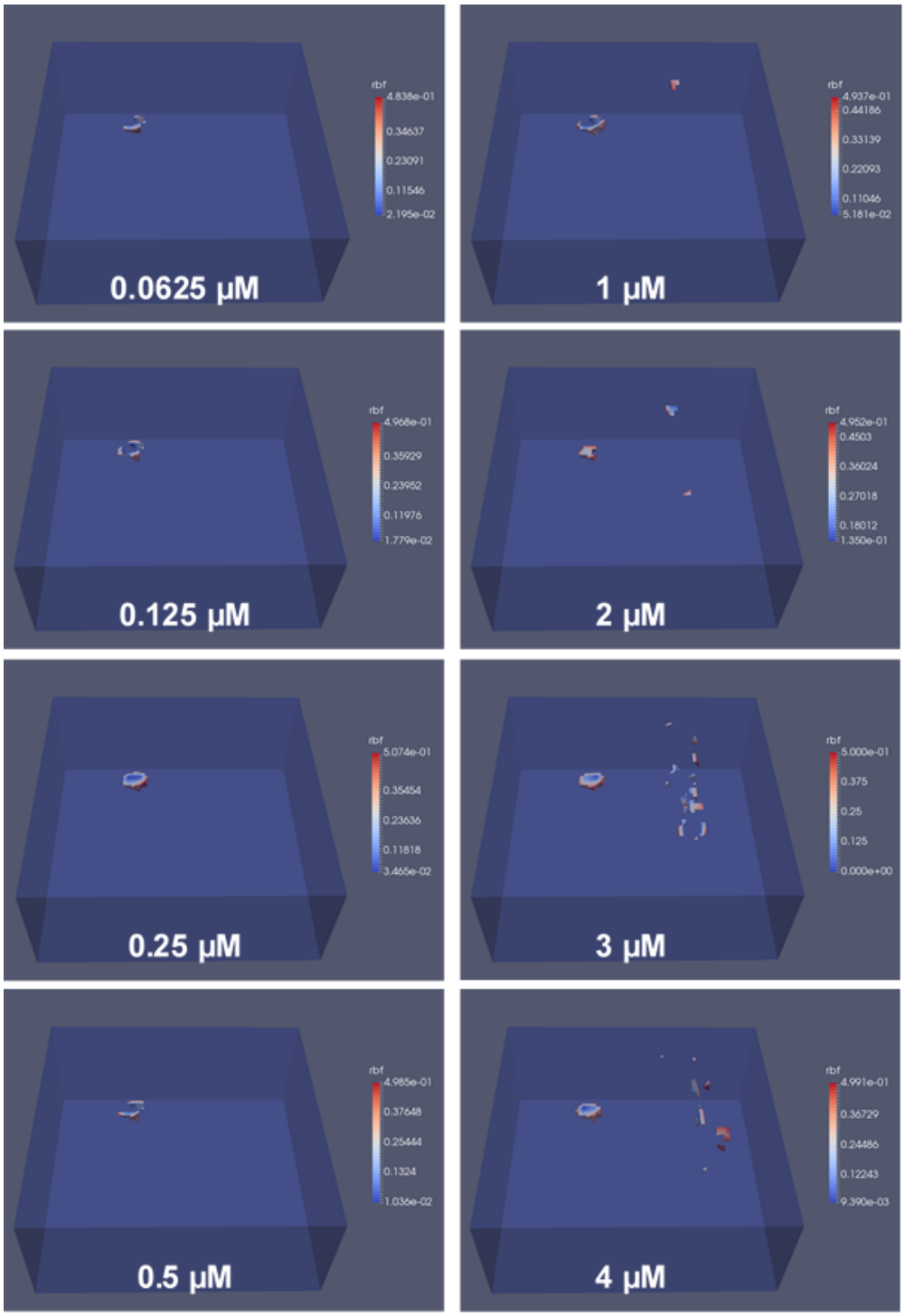

Figure 4.15: Recovered 830 nm flow. The heterogeneity as recovered by flow distributions with a half-min threshold for extraction over all steps.

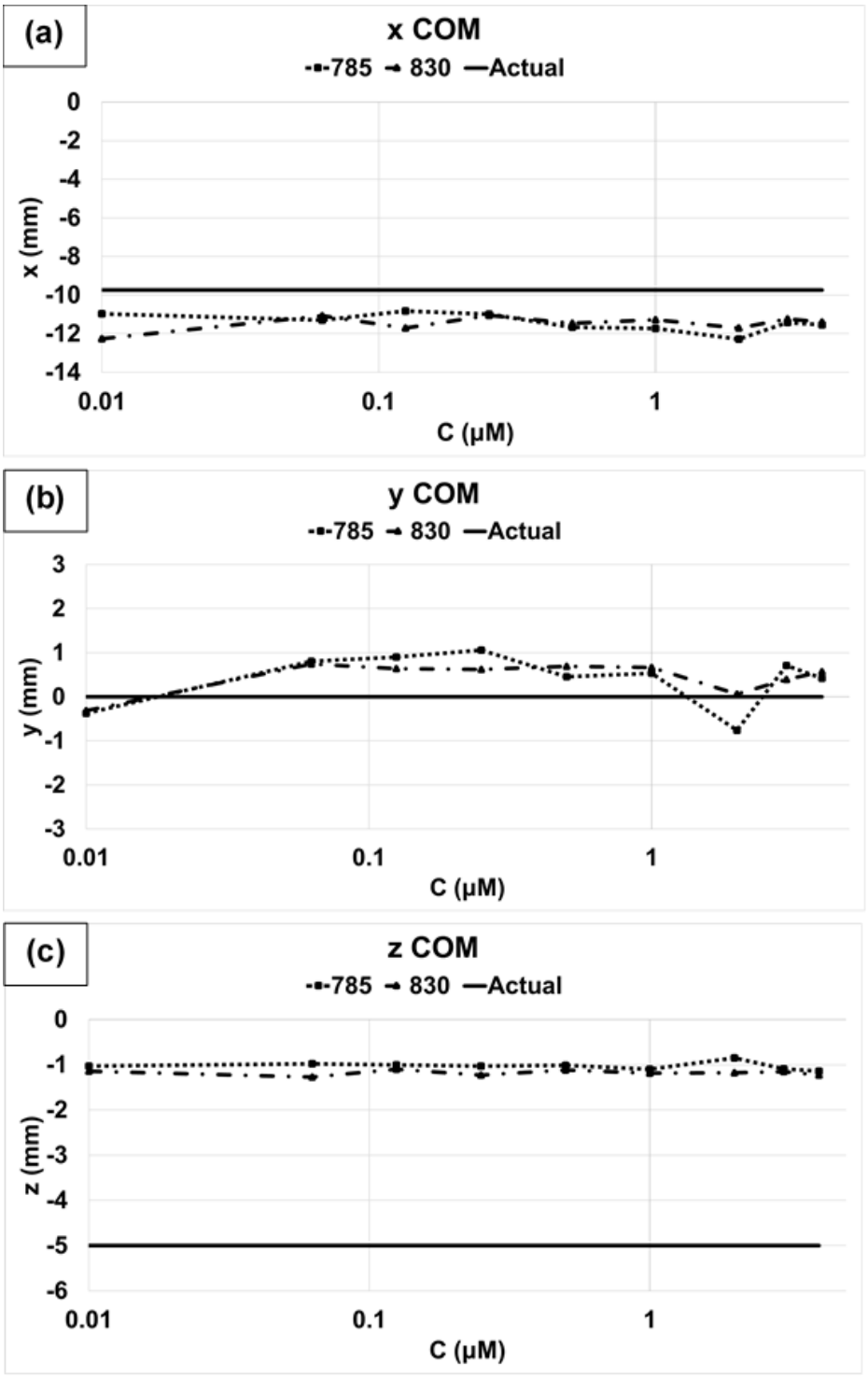

Figure 4.16: Cube location. The results of the recovered cube center of mass coordinates from the extracted flow heterogeneity at each step. The 0 μM step is represented as 0.01 μM for visualization on the log scale.

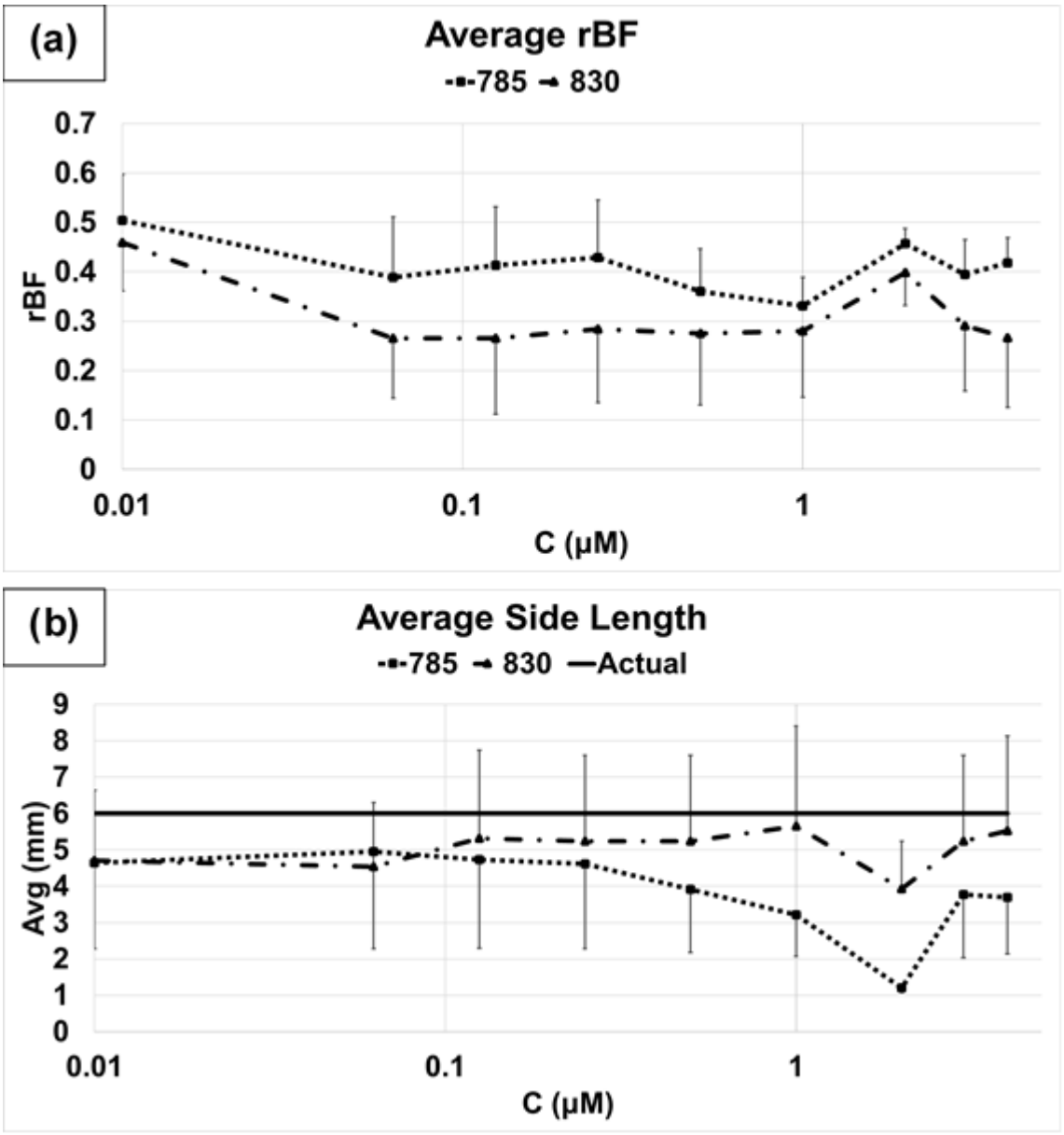

Figure 4.17: Cube characteristics. The (a) average rBF and (b) average side length from the heterogeneity extracted at each step from flow distributions. The 0 μM step is represented as 0.01 μM for visualization on the log scale.

4.7 Observations and Limitations

The results of this study provide insight into the feasibility of applying this prototype multimodal diffuse flow and fluorescence imaging system into recovering a combined tomographical set of parameters. The instrumentation possesses all the features desired in the outset, namely noncontact, noninvasive, translational potential, flexible design, reflectance mode, and important flow and fluorescence endpoint information. The incorporation of the novel nc_scDCT design provided enhanced sampling density and SD patterns over previous implementations. The addition of diffuse optical tomography techniques during experimentation has given prescience to problematic circumstances that may occur under application of this new device. Explication into the outcomes, reconciliations, and limitations will elucidate these findings.

There are two major time obstructions in this study, to be evaluated on a case by case basis in future studies, which are the stepwise and total experimentation times. For an individual step there is a tradeoff regarding bottleneck factors including the maximum camera frame rate, long fluorescence exposure time, source position number/density, and frame number (see **Figure 4.5** and **Table 4.1**). The camera frame rate can be improved by camera selection and binning. To retain a full set of pixel information we did not use binning. The fluorescence exposure time is an order greater than that used for absorption and two orders for flow. As the fluorescence signal is generally only a small fraction of the original signal one may seek to maximize filter quality, fluorescence concentrations,

excitation intensity, camera sensitivity, and use a fluorescent agent with greater quantum yield. The signal increase with fluorescence concentration may peak as is the case with ICG around 1-2 μM. An increase in source positions can probe a greater amount of detail from the sample. As the purpose of this study was to combine detection and characterization, we selected a distributed source pattern that included both homogeneous and heterogeneous regions. The data from each source must be taken independently due to the point-like source and detection models incorporated. Too many source positions may result in subject movement artifacts, physiological changes, and computational overhead. These time-consuming options are then protracted by the number of frames collected. The two sources as employed in this study add a multiplicative layer to this envelope. The total experimentation time is then, under the assumption that each step is identical in collection, scaled by the number of overall steps. For example, increasing the number of concentrations tested would greatly increase the total duration. The upper limit was the stability of ICG in aqueous solutions at approximately 6 hours. In clinical studies, the stability of ICG in plasma and whole blood is not a significant factor but the clearance rate and desired temporal resolution will intimate the governing constraints.

The most observable deviation from expectations was the disturbance of flow recovery with increasing ICG concentrations (see **Figures 4.14** and **4.15**). The source of this influence is not allocated to the fluorescence signal which is both filtered and inherently significantly weaker than the excitation light. The accompanied absorption coefficient changes are conversely known to cause

errors in diffuse correlation flow analysis [112, 118]. Specifically, an underestimation of the absorption coefficient results in an underestimation in the flow. As the absorption coefficient in the ICG tube is continually increasing (see **Figure 4.12**) it is expected that our use of the background value for fluorescence reconstructions is leading to an underestimate in flow. Therefore, the ICG region is promoting a drop in flow boundary data that is not due to any actual flow presence. As the referenced results analyze DCS rather than scDCS, typical parameters were used to show they are similarly affected (**Figure 4.18**). In most blood flow studies involving diffuse optics the relative blood flow over time is unchanged regardless of the absorption coefficient value. However, these are with the expectation that there are no changes during the experiment/interval. In the case of changing ICG the absorption coefficient is not static and therefore can introduce uncertainties in the results. The extent of influence depends both on the level of absorption coefficient change as well as the measurement in question. One must note the potential implications both on spatial and temporal heterogeneities. In this study, we only looked at flow relative to an otherwise homogeneous absorption background and with the flow and ICG in separate regions.

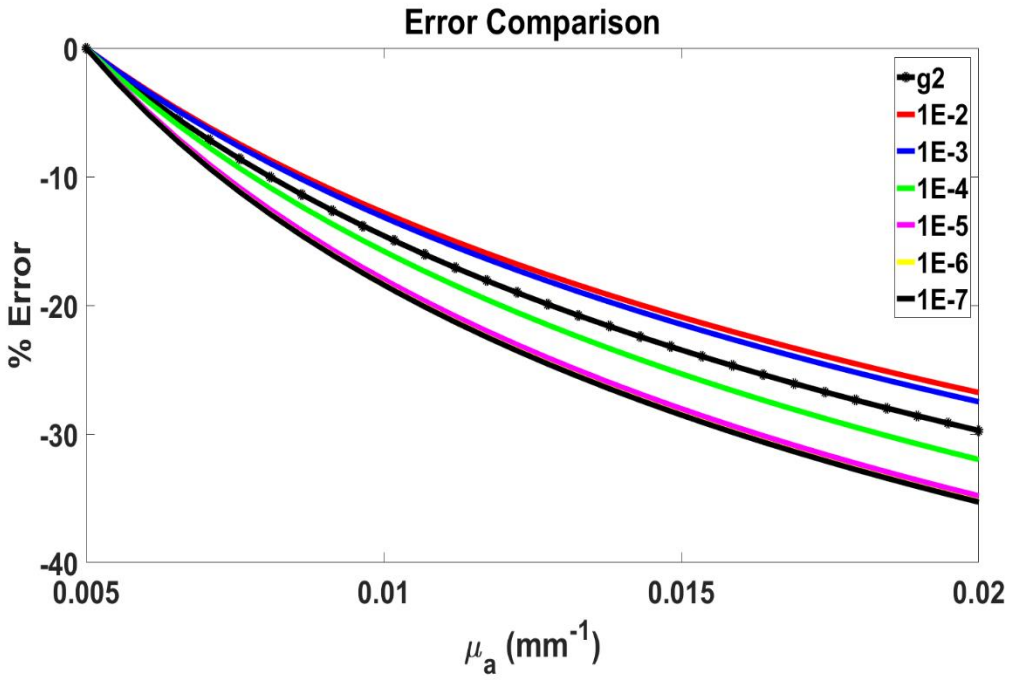

Figure 4.18: Comparison of DCS and scDCS errors with absorption coefficient. The percentage errors between the actual and recovered blood flow index by DCS (g2) and scDCS (K^2; multiple exposure times) in typical circumstances over increasingly underestimated absorption coefficients. In this study, a 5 ms exposure time for flow corresponds to the region between the red and blue solid lines.

To minimize the absorption change influence on flow results, we consider several counteractions by means of system modification, context leveraging, or measurement protocol adjustment. Two system additions were integrated in the current study: adding a second laser source (830 nm) at a different wavelength from that used to induce a strong fluorescent signal (785 nm), and monitoring μ_a changes with DOT. When selecting a separate source for flow we enlist a wavelength outside of the maximum region of ICG absorption. From **Figures 4.14**

– 4.17, the 830 nm with a lower position in the ICG excitation spectrum (**Figure 4.2**) did offer an improvement in flow results. A source on the lower end, around 660 nm, is another option. The accompanying optical properties will, however, inhibit in other ways including increased scattering at lower wavelengths and increases in chromophore absorption at both ends of the NIR spectrum (**Figure 1.1**). In either case, there will be two laser sources required which can greatly increase data acquisition time as described earlier. We also added DOT to append our parameter set with the absorption changes. From this we found a large absorption change (**Figure 4.12**). In practice, by reviewing this concurrent information post-measurement volumes of large absorption change may be marked unreliable and removed from further analysis. We would first need to select a threshold for what constitutes a large absorption change (e.g., use estimates for DCS [118] or perform equivalent scDCS analysis) as well as remove all flow boundary data that is sensitive to the region(s) effected. In real tissues this solution could become intractable due to heterogeneous distributions, DOT measurement uncertainties, and the ability to perform reconstruction adequately with remaining data. In such circumstances the flow data would be completely disregarded. The ability to add CW DOT is straightforward with the combined system as the laser source and filter are already implemented. There is, of course, the additional overhead of collecting the DOT data which can inhibit the temporal resolution. System modifications may not be necessary if, by experience, we already know the ICG absorption to fluctuate only within a small range (as the absorption contrast itself is a popular use of ICG). In practice, the fluorescence is usually

examined in relative fashion and can be subject to pH and tissue microenvironment variations and therefore is in general, by itself, an insufficient indicator of feasibility. Other fluorescent agents than ICG require individual examination. Finally, one might simply acquiesce to the possibility of unresolvable absorption interference and restrict flow measurements to pre-fluorescence injection and post-clearance (or the phantom equivalent). We note here for completeness that the reduced scattering coefficient has an even greater influence on flow recovery than the absorption coefficient, but that there is no expected introduction of significant scattering changes due to ICG [135]. An additional consideration is the red-shifting of ICG absorption in plasma as opposed to the aqueous solution tested (**Figure 4.2**).

The computing resources for processing the fluorescence data surpassed that available for our reconstruction computer (2.80 GHz i7-7700HQ, 32.0 GB memory) requiring a mesh of decreased density. This is primarily due to the implementation building a pre- and current-iteration Jacobian which collectively has greater memory requirements than the standard CW DOT or flow reconstructions. For the standard reconstructions a conjugate gradient alternative is available to reduce memory expense with a longer reconstruction time but was not implemented for fluorescence at the time of this study. It is technically simple to convert a mesh created for flow to that for absorption and fluorescence given they are all in MATLAB and can be done in future studies to have a directly comparable set of mesh information. Use of supercomputing resources, Jacobian subsets, task paralellization, GPU-based solvers, and fewer SD combinations can help relax

overhead on mesh agreement and reduce computation times [137, 138]. The valid SD combinations depend on both the source positions as outlined earlier as well as the defined detectors. When selecting a detector grid we avoid touching (side-by-side) spacings which contribute marginal information in terms of the tradeoff for spatial sampling. Increasing the detector number extends the reconstruction time and necessary resources.

We conclude that with this prototype we illustrated the ability to extract flow and fluorescence, but that the situation in practice is complex and requires care in properly setting up, acquiring, and consuming the information. In the next chapter we look towards the future and areas of improvement.

CHAPTER 5 STUDY SUMMARY, LIMITATIONS, AND FUTURE PERSPECTIVES

5.1 Study Summary

In this dissertation, I presented a progression of continuously advancing diffuse optical devices towards the noncontact reflectance imaging of 3D flow and fluorescence distributions in deep tissues/phantoms. The initial ncDCT system with its mechanical scanning apparatus, complex boundary acquisition methods, and new FEM flow reconstruction technique provided a useful first generation of completely noncontact flow imaging capability. This instrument was applied to a small animal aggressive breast tumor model highlighting the potential for longitudinal reflectance flow imaging for visualization and relative quantification of cancerous microvascular developments. The successor scDCT system demonstrated a movement to CCD-based light detection for improved spatial and temporal detector sampling, a uniquely requisite smear correction, and speckle contrast flow measurement. Testing illustrated a sensitivity to the presence of high flow contrast and subsequent characterization. The final multimodal nc_scDCT and DFT prototype made its province with the best features of both the previous systems along with related noncontact scDCT developments. With this fully noncontact source and detector arrangement and filter set, high contrast flow and fluorescent heterogeneities were identified and characterized in tissue-like phantoms.

The novel nc_scDCT/DFT system embodies all the desirables proposed in the outset. The potential for new cancer studies are extensive, especially by coupling

the realm of nanoparticles. For example, nanoparticles may be repletely tagged and monitored as drug carrying vehicles or, alternatively, designed to improve tumor targeting for the proper localization of the fluorescence signal itself. As the vasculature is the most common route of conveyance for transporting agents throughout the tissues (as opposed to site injection for example), analyzing corresponding blood flow variations can offer new insights into the underlying factors contributing to nanoparticle success or failure. With the new instrument we can now build upon the already established advantages of the diffuse optical methods in cancer imaging.

My major contributions to the studies herein are as follows:

ncDCT. I had primarily a supporting role in the development of ncDCS/ncDCT instrumentation, source and detector alignment on complex boundaries, and ncDCT application to breast tumors. My major contributions in respect to ncDCT concern its application to small animal tumors. I performed all animal ncDCT measurements, image reconstructions, and analysis (**Chapter 2.6**). I was able to find average tumor flow changes and volumes after a four-day gap for a mouse with two palpable tumors. The localization and separation of tumor tissues relative to healthy tissues was also described along with numerous observations for enhancing future studies of a similar nature.

scDCT. Forwarding the transition from APD to CCD detection I derived the relationship between speckle contrast and the semi-infinite form of the electric field temporal autocorrelation function as modeled by the correlation diffusion equation (**Equations 3.1 – 3.9**; **Chapter 3.3**). I also worked with a vendor to obtain a

customized optical switch to fulfill our requirements within the constraints and wrote the LabVIEW program to operate it in sequencing light around the FOV for phantom experimentation. Through meeting Cancer Nanotechnology Training Center (CNTC) fellowship obligations (e.g., extra coursework, meetings, seminars, clinical experience, reports, outreach activities, and journal club attendance), I made available the funding for hardware (i.e., optical switch, zoom lens, DAQ board, etc.), software (e.g., SolidWorks and TracePro), and supplies with $25,775 funding, $30,000 stipend, and $3,200 travel funding.

nc_scDCT/DFT. I supplemented previous scDCT/nc_scDCT system designs with the necessary stackable tubes for combining the cross-polarizer and a set of filters to instantiate a multimodal nc_scDCT/DFT prototype (**Chapter 4**). I designed a flow and fluorescence experiment for verifying its proper operation. This included building a custom hinged holder from a clear acrylic sheet. An experimental protocol was carefully formed to exhibit the flow and fluorescence recovery within the constraints of source/detector number tradeoff and arrangement, ROI coverage, exposure time durations, frame averaging, and the number of steps to evaluate. Programming was added to coordinate source laser position scanning with varied exposure times and camera triggering. I performed all measurements, analysis, and summarization of the flow and fluorescence detection and characterizations. The CNTC fellowship also supported funding of components in this study including the galvo-mirror, filters, lenses, alternative test setups (involving filter wheels and lenses), and other related supplies.

Other. My other significant contributions include the assistance in writing, editing, and/or reviewing manuscripts, grant proposals, and presentations. I have been involved in many other *in vivo* studies including clinical measurements of human head and neck tumors prior to and during radiation therapy, breast tumor imaging, peripheral arterial revascularization surgery, electrical stimulation blood flow response, mouse leg cuff occlusion, and human subject orthostatic tolerance by cardiovascular response to antigravity treadmill and bed tilting.

5.2 Study Limitations and Future Perspectives

Flow acquisition improvements. Acquiring flow by means of speckle contrast from an image at a specific exposure time has its encumberments. Specifically, the exposure time is minimally flexible due to its relationship with flow, the aperture (f/#) is related to the smallest speckle size and Nyquist sampling, and the laser source must possess a long-coherence length. These factors combined limit the intensity. Utilizing the EM gain supplied by our highly sensitive EMCCD camera should enhance the available signal and reduce the influences of noise and promote repeatability. A camera with a greater frame rate will allow for more frame averaging. The type of noise to be minimized will dictate the experienced benefits of either such solutions.

Detection and characterization tradeoff. The testing of the multimodal imager prioritized neither heterogeneity detection or characterization. This mixed approach creates a situation where neither objective is optimized but rather a balance is obtained. The accuracy of object characterization can be improved by

taking more measurements near the heterogeneity such that most of the signals detected have interacted with it. However, in practice we may not know where such disturbances exist. As such, a spatially distributed set of SD pairs can be first utilized to localize the object with follow up imaging of increased sampling density in the target ROI's.

Device automation. The prototype nc_scDCT/DFT did not employ full automation. The extension thereof is expected to be straightforward with mostly time overhead. The filters can be exchanged dynamically with an appropriate motorized filter wheel for 2-inch diameter lenses. The laser sources can be alternated by the optical switch. The optical switch was not used during the current study so as to maximize flow signal. Combining the switch with the aforementioned flow signal compensations can make this feasible. Both the filter wheel and optical switch will incur some programming support for proper operation. Ultimately, this will provide the most robust system as originally conceptualized.

Flow reconstruction. The current flow reconstruction technique though useful couples the blood flow index reconstruction to the absorption coefficient in an undesirable fashion. It is anticipated that deriving an adjoint Jacobian formulation and corresponding update for flow specifically can improve flow imaging. This will not obviate the concerns regarding absorption changes. As is evident from the adjoint formulation, the absorption and reduced scattering coefficients continue to contribute to the sensitivity. Further investigation into L-curve analysis may also prove beneficial in optimizing selection of the reconstruction iteration to clarify the adequacy of assuming this method for the combined total absorption.

APPENDIX: GLOSSARY

Notations/ Terms	Description
α	Ratio of dynamic to total scatterers
αD_B	Blood flow index (BFI)
β	Factor related to speckle and collection optics
ϵ_{ex}	Fluorophore extinction coefficient
η	Fluorescence quantum yield
$\eta\mu_{a,fl}$	Fluorescent yield
λ	Wavelength
μ_a	Absorption coefficient
$\mu_{a,ex}$	Absorption coefficient (excitation)
$\mu_{a,fl}$	Absorption coefficient (emission)
μ_a^{total}	Total absorption coefficient
μ_s'	Reduced scattering coefficient
ν	Speed of light in tissue
ρ	Source-detector separation
τ	Correlation delay time
Φ	Photon fluence
Φ_{ex}	Photon fluence (excitation)
$\langle \Delta r^2(\tau) \rangle$	Mean-square scatterer displacement
BFI	Blood flow index (αD_B)

D	Photon diffusion coefficient
D_{ex}	Photon diffusion coefficient (excitation)
D_{fl}	Photon diffusion coefficient (emission)
D_B	Scatterer diffusion coefficient
G_1	Unnormalized temporal electric field autocorrelation function
g_1	Normalized temporal electric field autocorrelation function
G_2	Unnormalized temporal intensity autocorrelation function
g_2	Normalized temporal intensity autocorrelation function
I	Intensity
k_0	Wavenumber
K	Speckle contrast
n	Index of refraction
$[N]$	Fluorophore concentration
$\boldsymbol{r}$	Position vector
rBF	Relative blood flow
R_{eff}	Effective reflection coefficient
T	Exposure time
CW	Continuous wave
DCS/T	Diffuse correlation spectroscopy/tomography
DFS/T	Diffuse fluorescence spectroscopy/tomography
DOS/T	Diffuse optical spectroscopy/tomography
fps	Frames per second

ICG	Indocyanine green
ncDCS/T	Noncontact diffuse correlation spectroscopy/tomography
nc_scDCT	Noncontact speckle contrast diffuse correlation tomography
NIR	Near infrared
scDCS/T	Speckle contrast diffuse correlation spectroscopy/tomography
SD	Source-Detector separation

REFERENCES

[1] D. Hanahan and R. A. Weinberg, "Hallmarks of cancer: the next generation," *Cell,* vol. 144, no. 5, pp. 646-74, Mar 4 2011.

[2] P. Vaupel, F. Kallinowski, and P. Okunieff, "Blood flow, oxygen and nutrient supply, and metabolic microenvironment of human tumors: a review," (in eng), *Cancer Res,* vol. 49, no. 23, pp. 6449-65, Dec 1 1989.

[3] C. B. Wilson *et al.*, "Quantitative measurement of monoclonal antibody distribution and blood flow using positron emission tomography and 124iodine in patients with breast cancer," (in eng), *Int J Cancer,* vol. 47, no. 3, pp. 344-7, Feb 1 1991.

[4] H. Madjar, W. Sauerbrei, H. J. Prompeler, R. Wolfarth, and H. Gufler, "Color Doppler and duplex flow analysis for classification of breast lesions," (in eng), *Gynecol Oncol,* vol. 64, no. 3, pp. 392-403, Mar 1997.

[5] M. A. Hahn, A. K. Singh, P. Sharma, S. C. Brown, and B. M. Moudgil, "Nanoparticles as contrast agents for in-vivo bioimaging: current status and future perspectives," *Anal Bioanal Chem,* vol. 399, no. 1, pp. 3-27, Jan 2011.

[6] V. Saxena, M. Sadoqi, and J. Shao, "Indocyanine green-loaded biodegradable nanoparticles: preparation, physicochemical characterization and in vitro release," *Int J Pharm,* vol. 278, no. 2, pp. 293-301, Jul 8 2004.

[7] R. Tong, H. H. Chiang, and D. S. Kohane, "Photoswitchable nanoparticles for in vivo cancer chemotherapy," *Proc Natl Acad Sci U S A,* vol. 110, no. 47, pp. 19048-53, Nov 19 2013.

[8] R. K. Jain, "Delivery of molecular and cellular medicine to solid tumors," *Adv Drug Deliv Rev,* vol. 46, no. 1-3, pp. 149-68, Mar 1 2001.

[9] S. Eliasof *et al.*, "Correlating preclinical animal studies and human clinical trials of a multifunctional, polymeric nanoparticle," *Proc Natl Acad Sci U S A,* vol. 110, no. 37, pp. 15127-32, Sep 10 2013.

[10] T. Lei, A. Fernandez-Fernandez, R. Manchanda, Y. C. Huang, and A. J. McGoron, "Near-infrared dye loaded polymeric nanoparticles for cancer imaging and therapy and cellular response after laser-induced heating," *Beilstein J Nanotechnol,* vol. 5, pp. 313-22, 2014.

[11] H. Maeda, J. Wu, T. Sawa, Y. Matsumura, and K. Hori, "Tumor vascular permeability and the EPR effect in macromolecular therapeutics: a review," *J Control Release,* vol. 65, no. 1-2, pp. 271-84, Mar 1 2000.

[12] M. Ferrari, "Cancer nanotechnology: opportunities and challenges," *Nat Rev Cancer,* vol. 5, no. 3, pp. 161-71, Mar 2005.

[13] M. Cutler, "Transillumination of the Breast," *Ann Surg,* vol. 93, no. 1, pp. 223-34, Jan 1931.

[14] F. F. Jobsis, "Noninvasive infrared monitoring of cerebral and myocardial sufficiency and circulatory parameters.," *Science,* vol. 198, pp. 1264-1267, 1977.

[15] L. V. Wang, H. I. Wu, and W. Wang, *Biomedical Optics: Principles And Imaging*. Wiley-Interscience, 2007.

[16] V. Ntziachristos, A. G. Yodh, M. Schnall, and B. Chance, "Concurrent MRI and diffuse optical tomography of breast after indocyanine green enhancement," *Proceedings of the National Academy of Sciences of the United States of America,* vol. 97, no. 6, pp. 2767-2772, MAR 14 2000.

[17] A. Corlu *et al.*, "Three-dimensional in vivo fluorescence diffuse optical tomography of breast cancer in humans," (in eng), *Opt Express,* vol. 15, no. 11, pp. 6696-716, May 28 2007.

[18] B. Alacam, B. Yazici, X. Intes, and B. Chance, "Analysis of ICG Pharmacokinetics in Cancerous Tumors using NIR Optical Methods," *Conf Proc IEEE Eng Med Biol Soc,* vol. 1, pp. 62-5, 2005.

[19] X. D. Li, B. Chance, and A. G. Yodh, "Fluorescent heterogeneities in turbid media: limits for detection, characterization, and comparison with absorption," *Applied Optics,* vol. 37, no. 28, pp. 6833-6844, OCT 1 1998.

[20] L. He, Y. Lin, C. Huang, D. Irwin, M. M. Szabunio, and G. Yu, "Noncontact diffuse correlation tomography of human breast tumor," *J Biomed Opt,* vol. 20, no. 8, p. 86003, Aug 2015.

[21] L. Dong *et al.*, "Diffuse optical measurements of head and neck tumor hemodynamics for early prediction of chemoradiation therapy outcomes," *J Biomed Opt,* vol. 21, no. 8, p. 85004, Aug 1 2016.

[22] T. Durduran, R. Choe, W. B. Baker, and A. G. Yodh, "Diffuse optics for tissue monitoring and tomography," (in English), *Reports on Progress in Physics,* vol. 73, no. 7, p. 076701, Jul 2010.

[23] A. Yodh and B. Chance, "Spectroscopy and Imaging with Diffusing Light," *Physics Today,* vol. 48, no. 3, pp. 34-40, MAR 1995.

[24] M. D. Reisman, Z. E. Markow, A. Q. Bauer, and J. P. Culver, "Structured illumination diffuse optical tomography for noninvasive functional neuroimaging in mice," *Neurophotonics,* vol. 4, no. 2, p. 021102, Apr 2017.

[25] A. T. Eggebrecht *et al.*, "Mapping distributed brain function and networks with diffuse optical tomography," *Nat Photonics,* vol. 8, no. 6, pp. 448-454, Jun 2014.

[26] T. Durduran *et al.*, "Transcranial optical monitoring of cerebrovascular hemodynamics in acute stroke patients," (in eng), *Opt Express,* vol. 17, no. 5, pp. 3884-902, Mar 2 2009.

[27] X. J. Gu, Q. Z. Zhang, M. Bartlett, L. Schutz, L. L. Fajardo, and H. B. Jiang, "Differentiation of cysts from solid tumors in the breast with diffuse optical tomography," *Academic Radiology,* vol. 11, no. 1, pp. 53-60, JAN 2004.

[28] V. Ntziachristos, "Going deeper than microscopy: the optical imaging frontier in biology," (in English), *Nature Methods,* vol. 7, no. 8, pp. 603-614, Aug 2010.

[29] V. Ntziachristos, J. Ripoll, L. V. Wang, and R. Weissleder, "Looking and listening to light: the evolution of whole-body photonic imaging," *Nat Biotechnol,* vol. 23, no. 3, pp. 313-20, Mar 2005.

[30] X. Intes, Ripoll, J., Chen, Y., Nioka, S., Yodh, A.G., Chance, B., "In vivo continuous-wave optical breast imaging enhanced with Indocyanine Green," *Medical Physics,* vol. 30, pp. 1039-1047, 2003.

[31] D. J. Hawrysz and E. M. Sevick-Muraca, "Developments toward diagnostic breast cancer imaging using near-infrared optical measurements and fluorescent contrast agents," *Neoplasia,* vol. 2, no. 5, pp. 388-417., 2000.

[32] S. Nioka *et al.*, "Optical imaging of breast tumor by means of continuous waves," *Oxygen Transport to Tissue Xviii,* vol. 411, pp. 227-232, 1997.

[33] X. D. Li, Beauvoit, B., White, R., Nioka, S., Chance, B., and Yodh, A.G., "Tumor localization using fluorescence of indocyanine green (ICG) in rat model," *SPIE Proc.,* vol. 2389, p. 789, 1995.

[34] V. Ntziachristos and R. Weissleder, "Experimental three-dimensional fluorescence reconstruction of diffuse media by use of a normalized Born approximation," *Opt Lett,* vol. 26, no. 12, pp. 893-5, Jun 15 2001.

[35] K. Motomura, H. Inaji, Y. Komoike, T. Kasugai, S. Noguchi, and H. Koyama, "Sentinel node biopsy guided by indocyanine green dye in breast cancer patients," *Jpn J Clin Oncol,* vol. 29, no. 12, pp. 604-7, Dec 1999.

[36] B. Ebert *et al.*, "Near-infrared fluorescent dyes for enhanced contrast in optical mammography: phantom experiments," *J Biomed Opt,* vol. 6, no. 2, pp. 134-40., 2001.

[37] V. R. Kondepati, H. M. Heise, and J. Backhaus, "Recent applications of near-infrared spectroscopy in cancer diagnosis and therapy," (in eng), *Anal Bioanal Chem,* vol. 390, no. 1, pp. 125-39, Jan 2008.

[38] X. D. Li, M. A. O'Leary, D. A. Boas, B. Chance, and A. G. Yodh, "Fluorescent diffuse photon density waves in homogeneous and heterogeneous turbid media: analytic solutions and applications," *Appl Opt,* vol. 35, no. 19, pp. 3746-58, Jul 1 1996.

[39] G. Yu, "Near-infrared diffuse correlation spectroscopy in cancer diagnosis and therapy monitoring," *J Biomed Opt,* vol. 17, no. 1, p. 010901, Jan 2012.

[40] R. Cheng, Y. Shang, D. Hayes, Jr., S. P. Saha, and G. Yu, "Noninvasive optical evaluation of spontaneous low frequency oscillations in cerebral hemodynamics," *Neuroimage,* vol. 62, no. 3, pp. 1445-54, Sep 2012.

[41] Y. Shang *et al.*, "Noninvasive evaluation of electrical stimulation impacts on muscle hemodynamics via integrating diffuse optical spectroscopies with muscle stimulator," *J Biomed Opt,* vol. 18, no. 10, p. 105002, Oct 1 2013.

[42] G. Yu *et al.*, "Time-dependent blood flow and oxygenation in human skeletal muscles measured with noninvasive near-infrared diffuse optical spectroscopies," *J Biomed Opt,* vol. 10, no. 2, p. 024027, Mar-Apr 2005.

[43] K. Gurley, Y. Shang, and G. Yu, "Noninvasive optical quantification of absolute blood flow, blood oxygenation, and oxygen consumption rate in exercising skeletal muscle," *J Biomed Opt,* vol. 17, no. 7, p. 075010, Jul 2012.

[44] Y. Shang, Y. Zhao, R. Cheng, L. Dong, D. Irwin, and G. Yu, "Portable optical tissue flow oximeter based on diffuse correlation spectroscopy," (in eng), *Opt Lett,* vol. 34, no. 22, pp. 3556-8, Nov 15 2009.

[45] Y. Shang *et al.*, "Noninvasive optical characterization of muscle blood flow, oxygenation, and metabolism in women with fibromyalgia," *Arthritis Res Ther,* vol. 14, no. 6, p. R236, Nov 1 2012.

[46] Y. Shang, R. Cheng, L. Dong, S. J. Ryan, S. P. Saha, and G. Yu, "Cerebral monitoring during carotid endarterectomy using near-infrared diffuse optical spectroscopies and electroencephalogram," *Phys Med Biol,* vol. 56 pp. 3015-3032, 2011.

[47] G. Yu, Y. Shang, Y. Zhao, R. Cheng, L. Dong, and S. P. Saha, "Intraoperative evaluation of revascularization effect on ischemic muscle hemodynamics using near-infrared diffuse optical spectroscopies," (in English), *J Biomed Opt,* vol. 16, no. 2, p. 027004, Feb 2011.

[48] Y. Shang, T. B. Symons, T. Durduran, A. G. Yodh, and G. Yu, "Effects of muscle fiber motion on diffuse correlation spectroscopy blood flow measurements during exercise," *Biomed Opt Express,* vol. 1, no. 2, pp. 500-511, 2010.

[49] G. Yu, T. Durduran, C. Zhou, R. Cheng, and A. Yodh, "Near-infrared diffuse correlation spectroscopy (DCS) for assessment of tissue blood flow," in *Handbook of Biomedical Optics*, D. Boas, C. Pitris, and N. Ramanujam, Eds.: Taylor & Francis Books Inc, 2011, pp. 195-216.

[50] R. Cheng, "Noninvasive near-infrared diffuse optical monitoring of cerebral hemodynamics and autoregulation," Department of Biomedical Engineering, University of Kentucky, 2013.

[51] D. A. Boas, L. E. Campbell, and A. G. Yodh, "Scattering and imaging with diffusing temporal field correlations," *Phys Rev Lett,* vol. 75, no. 9, pp. 1855-1858, AUG 28 1995.

[52] R. Cheng *et al.*, "Near-infrared diffuse optical monitoring of cerebral blood flow and oxygenation for the prediction of vasovagal syncope," *J Biomed Opt,* vol. 19, no. 1, p. 17001, Jan 2014.

[53] L. Dong *et al.*, "Noninvasive diffuse optical monitoring of head and neck tumor blood flow and oxygenation during radiation delivery," *Biomed Opt Express,* vol. 3, no. 2, pp. 259-72, Feb 1 2012.

[54] U. Sunar *et al.*, "Noninvasive diffuse optical measurement of blood flow and blood oxygenation for monitoring radiation therapy in patients with head and neck tumors: a pilot study," (in eng), *J Biomed Opt,* vol. 11, no. 6, p. 064021, Nov-Dec 2006.

[55] C. Menon *et al.*, "An integrated clinically relevant approach to measuring tumor oxygen status using VEGF-transfected human melanoma xenografts as a model," *Cancer Research,* vol. 63, pp. 7232-7240, 2003.

[56] T. M. Busch *et al.*, "Fluence rate-dependent intratumor heterogeneity in physiologic and cytotoxic responses to Photofrin photodynamic therapy," (in English), *Photochem Photobiol Sci,* vol. 8, no. 12, pp. 1683-1693, 2009.

[57] B. Henry *et al.*, "Hybrid diffuse optical techniques for continuous hemodynamic measurement in gastrocnemius during plantar flexion exercise," *J Biomed Opt,* vol. 20, no. 12, p. 125006, 2015.

[58] C. Zhou *et al.*, "Diffuse optical monitoring of blood flow and oxygenation in human breast cancer during early stages of neoadjuvant chemotherapy," (in eng), *J Biomed Opt,* vol. 12, no. 5, p. 051903, Sep-Oct 2007.

[59] T. Durduran *et al.*, "Diffuse optical measurement of blood flow in breast tumors," (in eng), *Opt Lett,* vol. 30, no. 21, pp. 2915-7, Nov 1 2005.

[60] G. Yu *et al.*, "Noninvasive monitoring of murine tumor blood flow during and after photodynamic therapy provides early assessment of therapeutic efficacy," (in eng), *Clin Cancer Res,* vol. 11, no. 9, pp. 3543-52, May 1 2005.

[61] G. Ramirez *et al.*, "Chemotherapeutic drug-specific alteration of microvascular blood flow in murine breast cancer as measured by diffuse correlation spectroscopy," *Biomed Opt Express,* vol. 7, no. 9, pp. 3610-3630, Sep 1 2016.

[62] J. D. Johansson *et al.*, "Scanning, non-contact, hybrid broadband diffuse optical spectroscopy and diffuse correlation spectroscopy system," *Biomed Opt Express,* vol. 7, no. 2, pp. 481-98, Feb 1 2016.

[63] D. A. Boas and A. G. Yodh, "Spatially varying dynamical properties of turbid media probed with diffusing temporal light correlation," *J Opt Soc Am A Opt Image Sci Vis,* vol. 14, no. 1, pp. 192-215, JAN 1997.

[64] M. Schweiger, S. R. Arridge, M. Hiraoka, and D. T. Delpy, "The finite element method for the propagation of light in scattering media: boundary and source conditions," *Med Phys,* vol. 22, no. 11 Pt 1, pp. 1779-92, Nov 1995.

[65] G. Yu, "Diffuse Correlation Spectroscopy (DCS): A Diagnostic Tool for Assessing Tissue Blood Flow in Vascular-Related Diseases and Therapies," (in English), *Current Medical Imaging Reviews,* vol. 8, no. 3, pp. 194-210, Aug 2012.

[66] T. Durduran, "Non-invasive measurements of tissue hemodynamics with hybrid diffuse optical methods," Ph.D. thesis, University of Pennsylvania, Dissertation, 2004.

[67] Y. Shang, L. Chen, M. Toborek, and G. Yu, "Diffuse optical monitoring of repeated cerebral ischemia in mice," *Opt Express,* vol. 19, no. 21, pp. 20301-15, Oct 10 2011.

[68] E. M. Buckley *et al.*, "Cerebral hemodynamics in preterm infants during positional intervention measured with diffuse correlation spectroscopy and transcranial Doppler ultrasound," (in eng), *Opt Express,* vol. 17, no. 15, pp. 12571-81, Jul 20 2009.

[69] N. Roche-Labarbe *et al.*, "Noninvasive optical measures of CBV, StO(2), CBF index, and rCMRO(2) in human premature neonates' brains in the first six weeks of life," (in eng), *Hum Brain Mapp,* vol. 31, no. 3, pp. 341-52, Mar 2010.

[70] M. N. Kim *et al.*, "Noninvasive measurement of cerebral blood flow and blood oxygenation using near-infrared and diffuse correlation spectroscopies in critically brain-injured adults," (in eng), *Neurocrit Care,* vol. 12, no. 2, pp. 173-80, Apr 2010.

[71] G. Yu *et al.*, "Validation of diffuse correlation spectroscopy for muscle blood flow with concurrent arterial spin labeled perfusion MRI," *Opt Express,* vol. 15, no. 3, pp. 1064-1075 2007.

[72] C. Zhou *et al.*, "Diffuse optical monitoring of hemodynamic changes in piglet brain with closed head injury," (in eng), *J Biomed Opt,* vol. 14, no. 3, p. 034015, May-Jun 2009.

[73] S. O. Rice, "Mathematical analysis of random noise," in *Noise and Stochastic Processes*, N. Wax, Ed. New York: Dover, 1954, p. 133.

[74] L. Dong, L. He, Y. Lin, Y. Shang, and G. Yu, "Simultaneously extracting multiple parameters via fitting one single autocorrelation function curve in diffuse correlation spectroscopy," *IEEE Trans Biomed Eng,* vol. 60, no. 2, pp. 361-8, Feb 2013.

[75] L. He, Y. Lin, Y. Shang, B. J. Shelton, and G. Yu, "Using optical fibers with different modes to improve the signal-to-noise ratio of diffuse correlation spectroscopy flow-oximeter measurements," (in English), *Journal of Biomedical Optics,* vol. 18, no. 3, Mar 2013.

[76] R. Toy *et al.*, "Multimodal in vivo imaging exposes the voyage of nanoparticles in tumor microcirculation," *ACS Nano,* vol. 7, no. 4, pp. 3118-29, Apr 23 2013.

[77] D. R. Busch *et al.*, "Blood flow reduction in breast tissue due to mammographic compression," *Acad Radiol,* vol. 21, no. 2, pp. 151-61, Feb 2014.

[78] E. K. Chan, B. Sorg, D. Protsenko, M. O'Neil, M. Motamedi, and A. J. Welch, "Effects of compression on soft tissue optical properties," *Ieee Journal of Quantum Electronics,* vol. 2, no. 4, pp. 943-950, 1996.

[79] S. A. Carp *et al.*, "Compression-induced changes in the physiological state of the breast as observed through frequency domain photon migration measurements," *J Biomed Opt,* vol. 11, no. 6, p. 064016, Nov-Dec 2006.

[80] J. Ripoll, R. B. Schulz, and V. Ntziachristos, "Free-space propagation of diffuse light: Theory and experiments," *Physical Review Letters,* vol. 91, no. 10, pp. -, SEP 5 2003.

[81] R. B. Schulz, J. Ripoll, and V. Ntziachristos, "Experimental fluorescence tomography of tissues with noncontact measurements," (in English), *Ieee Transactions on Medical Imaging,* vol. 23, no. 4, pp. 492-500, Apr 2004.

[82] N. Deliolanis, T. Lasser, D. Hyde, A. Soubret, J. Ripoll, and V. Ntziachristos, "Free-space fluorescence molecular tomography utilizing 360 degrees geometry projections," *Opt Lett,* vol. 32, no. 4, pp. 382-4, Feb 15 2007.

[83] N. C. Deliolanis, J. Dunham, T. Wurdinger, J. L. Figueiredo, B. A. Tannous, and V. Ntziachristos, "In-vivo imaging of murine tumors using complete-angle projection fluorescence molecular tomography," *J Biomed Opt,* vol. 14, no. 3, p. 030509, May-Jun 2009.

[84] C. Zhou, G. Yu, D. Furuya, J. H. Greenberg, A. G. Yodh, and T. Durduran, "Diffuse optical correlation tomography of cerebral blood flow during cortical spreading depression in rat brain," *Opt Express,* vol. 14, pp. 1125-1144, 2006.

[85] Y. Lin, C. Huang, D. Irwin, L. He, Y. Shang, and G. Yu, "Three-dimensional flow contrast imaging of deep tissue using noncontact diffuse correlation tomography," *Appl Phys Lett,* vol. 104, no. 12, p. 121103, Mar 24 2014.

[86] J. P. Culver, T. Durduran, T. Furuya, C. Cheung, J. H. Greenberg, and A. G. Yodh, "Diffuse optical tomography of cerebral blood flow, oxygenation, and metabolism in rat during focal ischemia," *J Cereb Blood Flow Metab,* vol. 23, no. 8, pp. 911-924, AUG 2003.

[87] A. F. Fercher and J. D. Briers, "Flow Visualization by Means of Single-Exposure Speckle Photography," (in English), *Optics Communications,* vol. 37, no. 5, pp. 326-330, 1981.

[88] D. A. Boas and A. K. Dunn, "Laser speckle contrast imaging in biomedical optics," *J Biomed Opt,* vol. 15, no. 1, p. 011109, Jan-Feb 2010.

[89] J. D. Briers, "Laser Doppler, speckle and related techniques for blood perfusion mapping and imaging," *Physiol Meas,* vol. 22, no. 4, pp. R35-66, Nov 2001.

[90] H. Cheng, Q. Luo, S. Zeng, S. Chen, J. Cen, and H. Gong, "Modified laser speckle imaging method with improved spatial resolution," *J Biomed Opt,* vol. 8, no. 3, pp. 559-64, Jul 2003.

[91] R. Bi, J. Dong, and K. Lee, "Deep tissue flowmetry based on diffuse speckle contrast analysis," *Opt Lett,* vol. 38, no. 9, pp. 1401-3, May 1 2013.

[92] R. Bi, J. Dong, and K. Lee, "Multi-channel deep tissue flowmetry based on temporal diffuse speckle contrast analysis," *Opt Express,* vol. 21, no. 19, pp. 22854-22861, Sep 23 2013.

[93] M. Seong *et al.*, "Simultaneous blood flow and blood oxygenation measurements using a combination of diffuse speckle contrast analysis and near-infrared spectroscopy," *J Biomed Opt,* vol. 21, no. 2, p. 27001, Feb 2016.

[94] C. P. Valdes, H. M. Varma, A. K. Kristoffersen, T. Dragojevic, J. P. Culver, and T. Durduran, "Speckle contrast optical spectroscopy, a non-invasive, diffuse optical method for measuring microvascular blood flow in tissue," *Biomed Opt Express,* vol. 5, no. 8, pp. 2769-84, Aug 1 2014.

[95] H. M. Varma, C. P. Valdes, A. K. Kristoffersen, J. P. Culver, and T. Durduran, "Speckle contrast optical tomography: A new method for deep tissue three-dimensional tomography of blood flow," *Biomed Opt Express,* vol. 5, no. 4, pp. 1275-89, Apr 1 2014.

[96] C. Huang *et al.*, "Noncontact diffuse optical assessment of blood flow changes in head and neck free tissue transfer flaps," *J Biomed Opt,* vol. 20, no. 7, p. 075008, Jul 2015.

[97] Y. Lin, L. He, Y. Shang, and G. Yu, "Noncontact diffuse correlation spectroscopy for noninvasive deep tissue blood flow measurement," *J Biomed Opt,* vol. 17, no. 1, p. 010502, Jan 2012.

[98] T. Li *et al.*, "Simultaneous measurement of deep tissue blood flow and oxygenation using noncontact diffuse correlation spectroscopy flow-oximeter," *Sci Rep,* vol. 3, p. 1358, 2013.

[99] C. Huang, Y. Lin, L. He, D. Irwin, M. M. Szabunio, and G. Yu, "Alignment of sources and detectors on breast surface for noncontact diffuse correlation

tomography of breast tumors," *Appl Opt,* vol. 54, no. 29, pp. 8808-16, Oct 10 2015.

[100] C. Huang *et al.*, "Noncontact 3-D Speckle Contrast Diffuse Correlation Tomography of Tissue Blood Flow Distribution," *IEEE Trans Med Imaging,* vol. 36, no. 10, pp. 2068-2076, Oct 2017.

[101] Y. Lin, C. Huang, D. Irwin, L. He, Y. Shang, and G. Yu, "Noncontact deep tissue hemodynamic imaging using diffuse correlation tomography," ed. Applied Physics Letters. Manuscript submitted for publication, 2013.

[102] D. A. Boas, "Diffuse photon probes of structural and dynamical properties of turbid media: Theory and biomedical applications," Ph.D., University of Pennsylvania, Dissertation, 1996.

[103] C. Zhou, "In-vivo optical imaging and spectroscopy of cerebral hemodynamics," Ph.D. thesis, University of Pennsylvania, Dissertation, 2007.

[104] S. R. Arridge, "Optical Tomography in medical imaging," *Inverse Problems,* vol. 15, pp. R41-R93, 1999.

[105] H. Dehghani *et al.*, "Near infrared optical tomography using NIRFAST: Algorithm for numerical model and image reconstruction," *Commun Numer Methods Eng,* vol. 25, no. 6, pp. 711-732, Aug 15 2008.

[106] S. R. Arridge and M. Schweiger, "Photon-measurement density functions. Part2: Finite-element-method calculations," *Applied Optics,* vol. 34, no. 34, pp. 8026-8037, 1995.

[107] S. R. Arridge, M. Schweiger, M. Hiraoka, and D. T. Delpy, "A finite element approach for modeling photon transport in tissue," *Med.Phys.,* vol. 20, pp. 299-309, 1993.

[108] M. Schweiger, Arridge, S.R., and Delpy, D.T., "Application of the finite-element method for the forward and inverse models in optical tomography," *Journal of Mathematical Imaging and Vision,* vol. 3, pp. 263-283, 1993.

[109] M. Schweiger, "Application of the Finite Element Method in Infrared Image Reconstruction of Scattering Media," PhD, Department of Medical Physics and Bioengineering, University College London, 1994.

[110] M. Jermyn *et al.*, "Fast segmentation and high-quality three-dimensional volume mesh creation from medical images for diffuse optical tomography," *J Biomed Opt,* vol. 18, no. 8, p. 86007, Aug 2013.

[111] S. R. Arridge, "Photon-measurement density functions. Part 1: Analytical forms," *Applied Optics,* vol. 34, no. 31, pp. 7395-7409, 1995.

[112] L. He, "Noncontact Diffuse Correlation Tomography of Breast Tumor," PhD, Biomedical Engineering, University of Kentucky, Lexington, KY, 2015.

[113] D. J. Slamon, G. M. Clark, S. G. Wong, W. J. Levin, A. Ullrich, and W. L. Mcguire, "Human-Breast Cancer - Correlation of Relapse and Survival with Amplification of the Her-2 Neu Oncogene," (in English), *Science,* vol. 235, no. 4785, pp. 177-182, Jan 9 1987.

[114] A. McCann, P. A. Johnston, P. A. Dervan, W. J. Gullick, and D. N. Carney, "c-erB-2 oncoprotein expression in malignant and nonmalignant breast tissue," *Ir J Med Sci,* vol. 158, no. 6, pp. 137-40, Jun 1989.

[115] M. C. Paterson *et al.*, "Correlation between C-Erbb-2 Amplification and Risk of Recurrent Disease in Node-Negative Breast-Cancer," (in English), *Cancer Research,* vol. 51, no. 2, pp. 556-567, Jan 15 1991.

[116] C. Ma, H. Lin, S. S. Leonard, X. Shi, J. Ye, and J. Luo, "Overexpression of ErbB2 enhances ethanol-stimulated intracellular signaling and invasion of human mammary epithelial and breast cancer cells in vitro," *Oncogene,* vol. 22, no. 34, pp. 5281-90, Aug 14 2003.

[117] S. Wang *et al.*, "Ethanol promotes mammary tumor growth and angiogenesis: the involvement of chemoattractant factor MCP-1," *Breast Cancer Res Treat,* vol. 133, no. 3, pp. 1037-48, Jun 2012.

[118] D. Irwin *et al.*, "Influences of tissue absorption and scattering on diffuse correlation spectroscopy blood flow measurements," *Biomed Opt Express,* vol. 2, no. 7, pp. 1969-1985, 2011.

[119] H. W. Wang *et al.*, "Treatment-induced changes in tumor oxygenation predict photodynamic therapy outcome," (in eng), *Cancer Res,* vol. 64, no. 20, pp. 7553-61, Oct 15 2004.

[120] T. Durduran *et al.*, "Bulk optical properties of healthy female breast tissue," *Physics in Medicine and Biology,* vol. 47, no. 16, pp. 2847-2861, AUG 21 2002.

[121] S. L. Jacques, "Optical properties of biological tissues: a review," *Phys Med Biol,* vol. 58, no. 11, pp. R37-61, Jun 7 2013.

[122] A. D. Krainov, A. M. Mokeeva, E. A. Sergeeva, P. D. Agrba, and M. Y. Kirillin, "Optical properties of mouse biotissues and their optical phantoms," *Optics and Spectroscopy,* vol. 115, no. 2, pp. 193-200, 2013.

[123] Y. Shang, T. Li, L. Chen, Y. Lin, M. Toborek, and G. Yu, "Extraction of diffuse correlation spectroscopy flow index by integration of th-order linear model with Monte Carlo simulation," *Appl Phys Lett,* vol. 104, no. 19, p. 193703, May 12 2014.

[124] Y. Shang and G. Yu, "A Nth-order linear algorithm for extracting diffuse correlation spectroscopy blood flow indices in heterogeneous tissues," *Appl Phys Lett,* vol. 105, no. 13, p. 133702, Sep 29 2014.

[125] C. Huang *et al.*, "Speckle contrast diffuse correlation tomography of complex turbid medium flow," *Med Phys,* vol. 42, no. 7, pp. 4000-6, Jul 2015.

[126] C. Huang *et al.*, "Low-cost compact diffuse speckle contrast flowmeter using small laser diode and bare charge-coupled-device," *J Biomed Opt,* vol. 21, no. 8, p. 80501, Aug 1 2016.

[127] S. J. Kirkpatrick, D. D. Duncan, and E. M. Wells-Gray, "Detrimental effects of speckle-pixel size matching in laser speckle contrast imaging," *Opt Lett,* vol. 33, no. 24, pp. 2886-8, Dec 15 2008.

[128] R. Bandyopadhyay, A. S. Gittings, S. S. Suh, P. K. Dixon, and D. J. Durian, "Speckle-visibility spectroscopy: A tool to study time-varying dynamics," (in English), *Review of Scientific Instruments,* vol. 76, no. 9, Sep 2005.

[129] W. Ruyten, "Smear correction for frame transfer charge-coupled-device cameras," *Opt Lett,* vol. 24, no. 13, pp. 878-80, Jul 1 1999.

[130] S. Yuan, "Sensitivity, noise and quantitative model of laser speckle contrast imaging," PhD PhD Thesis, PhD Thesis, Tufts University, Medford, MA, 2008.

[131] S. Yuan, A. Devor, D. A. Boas, and A. K. Dunn, "Determination of optimal exposure time for imaging of blood flow changes with laser speckle contrast imaging," *Appl Opt,* vol. 44, no. 10, pp. 1823-30, Apr 1 2005.

[132] D. D. Duncan, S. J. Kirkpatrick, and R. K. Wang, "Statistics of local speckle contrast," *J Opt Soc Am A Opt Image Sci Vis,* vol. 25, no. 1, pp. 9-15, Jan 2008.

[133] M. Watanabe and S. K. Nayar, "Telecentric optics for focus analysis," (in English), *Ieee Transactions on Pattern Analysis and Machine Intelligence,* vol. 19, no. 12, pp. 1360-1365, Dec 1997.

[134] L. Zhang, H. Zhao, W. B. Dong, N. Cao, and P. F. Zhang, "Design of an optical system consisting of a special telecentric lens for side-scattering measurement on individual cells," *Optical Engineering,* vol. 49, no. 5, 2010.

[135] B. Yuan, N. Chen, and Q. Zhu, "Emission and absorption properties of indocyanine green in Intralipid solution," *J Biomed Opt,* vol. 9, no. 3, pp. 497-503, May-Jun 2004.

[136] S. C. Davis, H. Dehghani, J. Wang, S. Jiang, B. W. Pogue, and K. D. Paulsen, "Image-guided diffuse optical fluorescence tomography

implemented with Laplacian-type regularization," *Opt Express,* vol. 15, no. 7, pp. 4066-82, Apr 2 2007.

[137] M. Doulgerakis, A. Eggebrecht, J. Culver, and H. Dehghani, "Towards real-time functional human brain imaging with diffuse optical tomography," in *Proc. of SPIE-OSA*, CA, 2017, vol. 10412, p. 1041209.

[138] X. Wu, A. T. Eggebrecht, S. L. Ferradal, J. P. Culver, and H. Dehghani, "Fast and efficient image reconstruction for high density diffuse optical imaging of the human brain," *Biomed Opt Express,* vol. 6, no. 11, pp. 4567-84, Nov 1 2015.

VITA

Daniel Irwin, Ph.D. Candidate

EDUCATION

University of Louisville, Louisville, Kentucky, USA

B.S., Computer Science and Computer Engineering, June 2008

University of Kentucky, Lexington, Kentucky, USA

M.S., Biomedical Engineering, December 2011

University of Kentucky, Lexington, Kentucky, USA

Ph.D. Candidate, Biomedical Engineering, August 2012 – present

PROFESSIONAL POSITIONS

Research Assistant (Biophotonics), Department of Biomedical Engineering, University of Kentucky, Lexington, KY, 2009 – present

Research Assistant (Cardiovascular), Department of Biomedical Engineering, University of Kentucky, Lexington, KY, 2010 – 2011

PROFESSIONAL MEMBERSHIPS

Optical Society of America (OSA), 2012 – 2017

Biomedical Engineering Society (BMES), 2010 – 2017

HONORS AND ACTIVITIES

Cancer Nano. Training Center (CNTC) Predoctoral Traineeship, 2013 – 2015

($25,775 Supply Funding; $30,000 Annual Stipend; $3,200 Travel Funding)

CNTC & Markey Cancer Center Joint Seminar, 2014

JOSA-A Manuscript Peer Reviewer, 2014

Visiting Student Mentor, 2014

Assist Rehabilitation Sciences Group Integrate LabVIEW Program, 2014

BME 530 LabVIEW/Project Introductory Lecture and Lab Assistant, 2013 – 2016

University of Kentucky BME Fall Newsletter Student Spotlight, 2013

Fundamentals of Engineering Exam Completion, 2013

Grant Proposal Feedback (Multiple Departments), 2012 – present

Engineers Day (E-Day) Volunteer, 2009 – 2011, 2015

Student Travel Support Award, University of Kentucky, 2011

Lab Liaison, 2010 – 2017

PUBLICATIONS

Peer-reviewed Papers

1. C. Huang, **D. Irwin**, M. Zhao, Y. Shang, N. B. Agochukwu, L. Wong, G. Yu, "Noncontact 3-dimensional speckle contrast diffuse correlation tomography of tissue blood flow distribution," *IEEE Transactions on Medical Imaging* 36 (10), (2017)
2. L. Dong, M. Kudrimoti, **D. Irwin**, L. Chen, S. Kumar, Y. Shang, C. Huang, E. L. Johnson, S. D. Stevens, B. J. Shelton, G. Yu, "Diffuse optical

measurements of head and neck tumor hemodynamics for early prediction of chemoradiation therapy outcomes," *JBO* 21(8), 085004 (2016)

3. C. Huang*, **D. Irwin***, Y. Lin, Y. Shang, L. He, W. Kong, J. Luo, G. Yu, "Speckle contrast diffuse correlation tomography of complex turbid medium flow," *Medical Physics Letter* 42(7), 4000 (2015). *Contributed equally
4. C. Huang, Y. Lin, L. He, **D. Irwin**, M. Szabunio, G. Yu, "Alignment of sources and detectors on breast surface for noncontact diffuse correlation tomography of breast tumors," *Appl Opt* 54(29), 8808-8816 (2015)
5. L. He, Y. Lin, C. Huang, **D. Irwin**, M. Szabunio, G. Yu, "Noncontact diffuse correlation tomography of human breast tumor," *JBO* 20(8), 086003 (2015)
6. Y. Lin, C. Huang, **D. Irwin**, L. He, Y. Shang, G. Yu, "Three-dimensional flow contrast imaging of deep tissue using noncontact diffuse correlation tomography," *Appl Phys Lett* 104(12), 121103 (2014)
7. **D. Irwin**, L. Dong, Y. Shang, R. Cheng, M. Kudrimoti, S. D. Stevens, G. Yu, "Influences of tissue absorption and scattering on diffuse correlation spectroscopy blood flow measurements," *Biomedical Optics Express* 2, 1969-1985 (2011)
8. Y. Shang, Y. Zhao, R. Cheng, L. Dong, **D. Irwin**, G. Yu, "Portable optical tissue flow oximeter based on diffuse correlation spectroscopy," *Optics Letters* 34(22), 3556-3558 (2009)

Conference Abstracts/Proceedings

1. **D. Irwin**, C. Huang, M. Zhao, S. Mazdeyasna, A. Bahrani, G. Yu, "Noncontact optical imaging of flow and fluorescence contrasts," *University of Kentucky Center for Clinical and Translational Science 13th Annual Spring Conference*, Lexington, KY, USA (2018)
2. M. Zhao, C. Huang, **D. Irwin**, S. Mazdeyasna, N. Agochukwu, R. Li, L. Wong, G. Yu, "Noncontact 3-dimensional speckle contrast diffuse correlation tomography of tissue blood flow distribution," *Biomedical Engineering Society Annual Meeting*, Phoenix, AZ, USA (2017)
3. **D. Irwin***, C. Huang*, Y. Lin, Y. Shang, L. He, W. Kong, J. Luo, G. Yu, "Speckle contrast diffuse correlation tomography (scDCT): A reflectance-based FEM technique for flow contrast imaging of complex turbid media," *Biomedical Engineering Society Annual Meeting*, Tampa, FL, USA (2015), * Equal contributors
4. L. Dong, **D. Irwin**, Y. Shang, L. Chen, B. Shelton, S. Stevens, M. Kudrimoti, G. Yu, "Diffuse optical measurements of head and neck tumor hemodynamics for early prediction of radiation therapy outcomes," *Biomedical Engineering Society Annual Meeting*, Tampa, FL, USA (2015)
5. L. He, Y. Lin, C. Huang, **D. Irwin**, M. Szabunio, G. Yu, "Noncontact diffuse correlation tomography of human breast tumor," *Biomedical Engineering Society Annual Meeting*, Tampa, FL, USA (2015)
6. **D. Irwin***, C. Huang*, Y. Lin, Y. Shang, L. He, W. Kong, J. Luo, G. Yu, "Speckle contrast diffuse correlation tomography for flow contrast imaging

of complex turbid media," *Markey Cancer Center Research Day*, Lexington, KY, USA (2015), * Equal contributors

7. L. Dong, M. Kudrimoti, **D. Irwin**, L. Chen, Y. Shang, X. Li, S. D. Stevens, B. J. Shelton, G. Yu, "Diffuse optical measurements of head and neck tumor hemodynamics for early prediction of radiation therapy," *Markey Cancer Center Research Day*, Lexington, KY, USA (2015)
8. L. He, Y. Lin, C. Huang, **D. Irwin**, M. Szabunio, G. Yu, "Noncontact diffuse optical 3-D imaging of hemodynamic contrasts in breast tumor: Computer simulation," *Markey Cancer Center Research Day*, Lexington, KY, USA (2015)
9. **D. Irwin***, C. Huang*, Y. Lin, Y. Shang, L. He, W. Kong, J. Luo, G. Yu, "Speckle contrast diffuse correlation tomography for flow contrast imaging of complex turbid media," *University of Kentucky Center for Clinical and Translational Science 10th Annual Spring Conference*, Lexington, KY, USA (2015), * Equal contributors
10. L. He, Y. Lin, C. Huang, **D. Irwin**, M. Szabunio, G. Yu, "Noncontact diffuse optical 3-D imaging of hemodynamic contrasts in breast tumor: Computer simulation," *University of Kentucky Center for Clinical and Translational Science 10th Annual Spring Conference*, Lexington, KY, USA (2015)
11. **D. Irwin**, Y. Lin, C. Huang, L. He, Y. Shang, M. Xu, H. Wang, J. Luo, G. Yu, "3-D Blood Flow Contrast Imaging Case Study on Small Animal Mammary Tumors Using Noncontact Diffuse Correlation Tomography (ncDCT),"

University of Kentucky Center for Clinical and Translational Science 9th Annual Spring Conference, Lexington, KY, USA (2014)

12. **D. Irwin**, Y. Lin, C. Huang, L. He, Y. Shang, M. Xu, H. Wang, J. Luo, G. Yu, "Noncontact Near-Infrared 3-D Blood Flow Contrast Imaging on Small Animal Mammary Tumors: A Case Study," *OSA BIOMED*, Miami, FL, USA (2014)
13. **D. Irwin**, Y. Lin, C. Huang, L. He, Y. Shang, M. Xu, H. Wang, J. Luo, G. Yu, "A Case Study on Mouse Mammary Tumor Blood Flow Contrast Imaging with 3-D Noncontact Diffuse Correlation Tomography," *Markey Cancer Center Research Day*, Lexington, KY, USA (2014)
14. Y. Lin, C. Huang, **D. Irwin**, L. He, Y. Shang, G. Yu, "Noncontact three-dimensional flow contrast imaging of deep tissue using diffuse correlation tomography," *OSA BIOMED*, Miami, FL, USA (2014)
15. Y. Lin, C. Huang, **D. Irwin**, L. He, Y. Shang, G. Yu, "Three-dimensional flow contrast imaging of deep tissue using noncontact diffuse correlation tomography (ncDCT)," *University of Kentucky Center for Clinical and Translational Science 9th Annual Spring Conference*, Lexington, KY, USA (2014)
16. L. He, Y. Lin, C. Huang, **D. Irwin**, M. Szabunio, G. Yu, "3-D blood flow imaging of breast tumor using noncontact diffuse correlation tomography (ncDCT): Computer simulations," *University of Kentucky Center for Clinical and Translational Science 9th Annual Spring Conference*, Lexington, KY, USA (2014)

17. L. Dong, M. Kudrimoti, **D. Irwin**, C. Huang, Y. Shang, J. Bruno, S. D. Stevens, B. J. Shelton, G. Yu, “Diffuse optical measurements of head and neck tumor hemodynamics for early prediction of radiation therapy,” *Markey Cancer Center Research Day*, Lexington, KY, USA (2014)
18. L. He, Y. Lin, C. Huang, **D. Irwin**, M. Szabunio, G. Yu, “Noncontact diffuse correlation tomography (ncDCT) for 3-D blood flow imaging of breast tumor,” *Markey Cancer Center Research Day*, Lexington, KY, USA (2014)
19. C. Huang, Y. Lin, L. He, **D. Irwin**, G. Yu, “A computer-aided-design approach to align sources and detectors on arbitrary tissue surface for noncontact diffuse correlation tomography,” *OSA BIOMED*, Miami, FL, USA (2014)
20. L. He, Y. Lin, C. Huang, **D. Irwin**, M. Szabunio, G. Yu, “3-D blood flow imaging of breast tumor using noncontact diffuse correlation tomography: computer simulations,” *OSA BIOMED*, Miami, FL, USA (2014)
21. Y. Lin, C. Huang, L. He, **D. Irwin**, Y. Shang, G. Yu, “Three-dimensional flow contrast imaging of deep tissue tumor using noncontact diffuse correlation tomography (ncDCT),” *Markey Cancer Center Research Day*, Lexington, KY, USA (2014)
22. **D. Irwin**, Y. Lin, L. He, C. Huang, Y. Shang, M. Zhao, G. Yu, “Noncontact 3-D imaging of small animal tumors with combined diffuse optical, correlation, and fluorescence tomography: preliminary results in phantoms,” in *Markey Cancer Center Research Day*, Lexington, KY, USA (2013)

23. L. He, Y. Lin, C. Huang, **D. Irwin**, M. Szabunio, G. Yu, “Noncontact diffuse optical 3-D imaging of hemodynamic contrasts in breast tumor: computer simulation,” in *Markey Cancer Center Research Day*, Lexington, KY, USA (2013)
24. C. Huang, Y. Lin, L. He, Y. Shang, **D. Irwin**, M. Szabunio, G. Yu, “Noncontact diffuse optical 3-D imaging of hemodynamic contrasts in breast tumor: geometrical reconstruction and alignment of optical sources and detectors,” in *Markey Cancer Center Research Day*, Lexington, KY, USA (2013)
25. **D. Irwin**, Y. Lin, L. He, C. Huang, Y. Shang, M. Zhao, G. Yu, “Noncontact 3-D imaging of small animal tumors with combined diffuse optical, correlation, and fluorescence tomography: preliminary results in phantoms,” in *University of Kentucky Center for Clinical and Translational Science 8th Annual CCTS Spring Conference*, Lexington, KY, USA (2013)
26. L. He, Y. Lin, C. Huang, **D. Irwin**, M. Szabunio, G. Yu, “Noncontact diffuse optical 3-D imaging of hemodynamic contrasts in breast tumor: computer simulation,” in *University of Kentucky Center for Clinical and Translational Science 8th Annual CCTS Spring Conference*, Lexington, KY, USA (2013)
27. C. Huang, Y. Lin, L. He, Y. Shang, **D. Irwin**, M. Szabunio, G. Yu, “Noncontact diffuse optical 3-D imaging of hemodynamic contrasts in breast tumor: geometrical reconstruction and alignment of optical sources and detectors,” in *University of Kentucky Center for Clinical and Translational Science 8th Annual CCTS Spring Conference*, Lexington, KY, USA (2013)

28. L. Dong, **D. Irwin**, Y. Shang, R. Cheng, M. Kudrimoti, S. D. Stevens, G. Yu, "Influences of tissue optical properties on diffuse correlation spectroscopy blood flow measurements," in *OSA Biomedical Optics (BIOMED)*, Miami, FL, USA (2012)
29. **D. Irwin**, L. Dong, Y. Shang, R. Cheng, M. Kudrimoti, S. D. Stevens, G. Yu, "Influences of tissue absorption and scattering on diffuse correlation spectroscopy blood flow measurements in head and neck tumors," in *Advances in Optics for Biotechnology, Medicine and Surgery XII, ECI Conferences*, Naples, FL, USA (2011)
30. **D. Irwin**, L. Dong, Y. Shang, R. Cheng, M. Kudrimoti, S. D. Stevens, G. Yu, "Influences of tissue absorption and scattering on diffuse correlation spectroscopy blood flow measurements in head and neck tumors," in *Markey Cancer Center Research Day*, Lexington, KY, USA (2011)
31. Y. Shang, R. Cheng, L. Dong, **D. Irwin**, K. M. Gurley, K. R. Swartz, S. S. Salles, G. Yu, "Evaluation of electronic stimulation impact on muscle hemodynamics using diffuse optical spectroscopies," in *23rd Annual Physical Medicine and Rehabilitation Research Day*, Lexington, KY, USA (2011)
32. Y. Shang, Y. Zhao, R. Cheng, L. Dong, **D. Irwin**, K. R. Swartz, S. S. Salles, G. Yu, "Diffuse optical spectroscopies for evaluation of muscle hemodynamic enhancements by electrical stimulation," in *OSA Biomedical Optics (BIOMED)*, Miami, FL, USA (2010)

33. G. Yu, Y. Shang, Y. Zhao, R. Cheng, L. Dong, **D. Irwin**, S. P. Saha, "Portable optical tissue flow oximeter for evaluation of revascularization effect on ischemic muscle hemodynamics," in *OSA Biomedical Optics (BIOMED)*, Miami, FL, USA (2010)
34. Y. Shang, Y. Zhao, R. Cheng, L. Dong, **D. Irwin**, K. R. Swartz, S. S. Salles, G. Yu, "Diffuse optical spectroscopies for evaluation of muscle hemodynamic enhancements by electrical stimulation," in *Muscle Biology Fall Retreat*, Lexington, KY, USA (2010)
35. G. Yu, Y. Zhao, R. Cheng, L. Dong, **D. Irwin**, "A portable optical tissue flow oximeter based on diffuse correlation spectroscopy," in *BiOS SPIE Photonics West*, San Francisco, CA, USA (2010)
36. Y. Shang, Y. Zhao, R. Cheng, **D. Irwin**, L. Dong, K. R. Swartz, S. S. Salles, G. Yu, "Noninvasive assessment of muscle hemodynamic enhancement by electrical stimulation using diffuse optical spectroscopies," in *Fall Annual Meeting of the Biomedical Engineering Society*, Pittsburgh, PA, USA (2009)
37. G. Yu, Y. Shang, Y. Zhao, R. Cheng, **D. Irwin**, L. Dong, K. R. Swartz, and S. S. Salles, "Diffuse optical evaluation of muscle hemodynamic responses to electrical stimulation," in *2nd Photonics and OptoElectronics Meetings*, Wuhan, China (2009)
38. Y. Shang, Y. Zhao, R. Cheng, **D. Irwin**, L. Dong, K. R. Swartz, S. S. Salles, G. Yu, "Noninvasive assessment of muscle hemodynamic enhancement by electrical stimulation using diffuse optical spectroscopies," in *Adult Skeletal*

Muscle Symposium: Clinical Problems, Molecular Targets, Lexington, KY, USA (2009)

39. Y. Shang, Y. Zhao, R. Cheng, **D. Irwin**, L. Dong, K. R. Swartz, S. S. Salles, G. Yu, “Noninvasive assessment of muscle hemodynamic enhancement by electrical stimulation using diffuse optical spectroscopies,” in *Linda and Jack Gill Heart Institute Cardiovascular Research Day*, Lexington, KY, USA (2009)